University of Ferrara
Physics and Earth Science Department

Ph.D. in PHYSICS
Disciplinary sector: Fis/01

DEVELOPMENT OF A PHOTOVOLTAIC VENTILATED FACADE -SMART SKIN- FOR THE CONTROL OF BUILDINGS THERMAL BUDGET

Advisor

Prof. Donato Vincenzi

Candidate

Giulio Mangherini

XXXIV CYCLE 2018-2022
COORD. PROF. ELEONORA LUPPI

Referees of the thesis

Prof. Rossella Corrao
Department of Architecture, University of Palermo, Italy

Prof. Maurizio Brocato
École nationale supérieure d'architecture Paris-Malaquais, France

Ph.D. Candidate

Giulio Mangherini

Advisor

Prof Donato Vincenzi

Abstract (English)

Buildings can weigh up to 40% of the total primary energy requirements of industrialized countries. A wider deployment of renewable energy sources is therefore crucial to fulfill the increasing trend towards decarbonization, and several studies demonstrated that the integration of photovoltaic technology in building façades had a great potential in decreasing the building energy loads. In fact, the implementation of the so-called Building Integrated Photovoltaic devices is significantly increasing. However, there is still little implementation of Luminescent Solar Concentrators (LSC) panels in this type of structures, even though they could be a very promising technology to be installed in building façades.

Here the realization of a natural Ventilated Façade (VF) integrating a LSC device as external pane is presented. A VF is the combination of two skins separated by an air cavity, and its working principle lies in the exploitation of solar radiation to create a thermal gradient between the outer and inner pane. The LSC optical properties were modeled with Matlab to describe the optical properties of this device (absorption, transmission, and reflection spectrum), and confirmed that LSC panels could be manufactured also with dimensions compatible with the typical ones of the building sector. The LSC optical properties were inserted in a finite element model developed with the software COMSOL Multiphysics, whose results were validated thanks to a comparison with experimental data. The obtained thermal and optical properties were then used in a new model created to perform the retrofit of a typical building envelope, which proved that this structure can be employed to decrease the building thermal budget in both summer and winter season. Finally, the VF thermal transmittance was compared to the maximum values prescribed by the Italian directive, confirming a promising result for a "proof of concept" research work.

Keywords: BIPV, Ventilated façade, LSC, CFD, energy saving

Abstract (Italiano)

La necessità di sopperire al fabbisogno energetico degli edifici attraverso fonti rinnovabili gioca un ruolo fondamentale nell'attuale processo di decarbonizzazione. Nei paesi industrializzati essi possono infatti rappresentare fino al 40% della produzione totale di energia primaria, percentuale a cui l'implementazione di dispositivi fotovoltaici architettonicamente integrati può apportare una riduzione significativa. Nonostante il loro impiego stia aumentando considerevolmente, l'implementazione di pannelli con tecnologia LSC è ancora poco diffusa in questo tipo di strutture, seppur essi siano particolarmente indicati per l'integrazione architettonica.

In questo lavoro è presentata la realizzazione di una Facciata Ventilata (VF) con ventilazione naturale, che integra un dispositivo LSC come componente esterna. Una VF è una struttura formata da due componenti, chiamate anche pelli, separate da un'intercapedine d'aria, che si basa sullo sfruttamento della radiazione solare per regolare il confort termico dell'edificio. La modellazione delle proprietà ottiche delle varie componenti della VF è perciò fondamentale per valutare le performance del sistema, in particolare quelle dell'LSC, che sono state modellate utilizzando Matlab. Le simulazioni hanno confermato che è possibile realizzare pannelli aventi dimensioni compatibili a quelle tipiche del settore edile, che sfruttino questa tecnologia, rendendone quindi possibile l'implementazione in questo tipo di strutture. Le proprietà ottiche dell'LSC (spettro di assorbimento, trasmissione e riflessione) sono state poi inserite in un modello agli elementi finiti sviluppato con il software COMSOL Multiphysics, il quale ha permesso di studiare le proprietà termiche dell'intera VF tramite il confronto con dati sperimentali. Le proprietà fisiche dei materiali sono state poi inserite in un secondo modello termico al fine di eseguire il retrofit di un tipico involucro edilizio. I risultati hanno dimostrato che una VF ideata in questo modo è effettivamente in grado ridurre il budget termico dell'edificio sia nella stagione estiva che in quella invernale. Infine, il confronto tra la trasmittanza termica della VF e i valori massimi prescritti dalla direttiva italiana, ha evidenziato un risultato promettente per una tesi di ricerca di tipologia "proof of concept".

Keywords: BIPV, Ventilated façade, LSC, CFD, energy saving

Contents

List of Figures

List of Tables

Preface

The increasing global energy demand has raised concerns about supply shortages, depletion of energy resources, and environmental implications. In particular, in the last few decades, the need for limiting climate change and reducing energy related carbon dioxide emissions is leading to a transformation of the global energy sector from fossil-based to zero-carbon energy sources. New policies have introduced technical and regulatory measures to promote this transition [1] and a more rational use of energy [2]. PhotoVoltaic (PV) technologies are the most promising renewable energy sources to lead this transition, thanks to the improvements in module efficiencies, the reduction in manufacturing costs, and the achievement of levelized costs of electricity.

Indeed, the cost of electricity from PV technologies is nowadays generally lower than other energy sources and approaches a similar price when a storage system is included. Moreover, if we consider utility scale PV plants, it is even lower than conventional fossil fuel generators [3]. The international energy agency report testifies that the growth of the global PV industry is mainly associated to the so-called solar farm or utility scale PV [4]. Namely, large-scale stand-alone facilities directly connected to the main regional grid, and designed to generate large amount of electricity, either using thermal energy collectors or PV panels. The main advantage of these structures lies in their energy cost per kW, in fact due to economy of scale fulfillment and maintenance costs are usually lower if compared to smaller PV plants. This assumption is valid as long as the solar farms are located immediately adjacent to existing electrical grids, since transmission distance plays a key role in the overall grid efficiency and in the electricity cost [5]. A concern that remains underestimated about these kinds of plants is whether they could influence the natural environment because of "heat island" effect. In fact, the PV panels introduction reduces the landscape albedo, thus warming the surrounding areas [6].

An alternative that limits both the distribution and the environmental drawbacks is the Distributed Model, and it consists in the installation of small or medium PV plants directly in urban areas. The installation of PV plants within metropolitan buildings, where most changes to the wildlife habitat have already occurred, highly decreases their environmental impact, and drastically decreases the distribution losses, as the energy is produced where it

will be used. Moreover, if the PV panels are properly installed, they can be used not only to decrease buildings energy demand but also to improve their energy efficiency.

The energy requirements in buildings are primarily related to building heating, air conditioning and electricity needs, which together account for 36% of global energy balance, and for 39% of energy-related CO_2 [7]. These values are even higher for European residential buildings [8], therefore the exploitation of distributed model can play a key role for an environmental-friendly transition. To invert this trend European Parliament enacted the Energy Performance of Buildings Directive 2018/844/EU (EPBD), which defined a new category of buildings called nearly Zero Energy Building (nZEB). They are building with a very high energy performance, having their annual energy requirements provided in a very significant extent by renewable energy sources located on-site or nearby [9]. Furthermore, the EPBD requires all new buildings to be nZEB from 2021 and promotes the transformation of existing ones. The introduction of nZEBs as the new building target shifts the role of the building from energy consumer to energy prosumer, therefore, representing a very interesting measure to reduce both energy consumption and CO_2 emissions related to the building sector.

For this reason, over the last decade a new paradigm of buildings has been defined as: nearly Zero Energy Building [10], Net Zero Energy Building [11], Zero Energy Building, or Zero Emission Building [12]. The difference between the various definitions is given by the period of time in which the building energy balance is considered, by the amount of CO_2 that the building produces, or by the location and nature of energy sources that power it.

According to De Boeck et al. [13], the parameters affecting the energy consumption of a building are several:

1. the building shape and orientation,
2. the insulation efficiency of the envelope, the fenestration-to-wall ratio (windows and doors) with the components of the window glazing and sill type,
3. the lighting system,
4. the presence of natural or mechanical ventilation systems affecting the Heating-Ventilating-Air Conditioning (HVAC) load,
5. the integration of renewable energy technologies.

Thanks to a careful analysis of these parameters two considerations can be expressed. Firstly, all the construction elements that define the separation between the interior and exterior of a building (namely building envelope) have a great impact on the overall building energy consumption. Secondly, the options to increase building envelope thermal efficiency are several. In particular, considering the amount of energy that strikes Earth surface every day, Passive Solar Systems (PSSs) could represent a very promising solution, especially in temperate or tropical climate [14–16].

The main issue of this kind of systems is represented by their architectonic impact, since to maximize their efficiency, they are usually characterized by dark colors. Unfortunately, dark surfaces are not always considered aesthetically appealing [17], especially in urban environments. Therefore, in the past, PSSs were often installed separately from the building or confined to the roof top in order to minimize their aesthetic impact [18,19]. This problem was solved by a new generation of PhotoVoltaic (PV) devices called Building Integrated PhotoVoltaic (BIPV). These are PV modules specifically designed to play a dual role, energy converters and architectural elements. Indeed, they are constituent elements of the architectural composition and replace conventional building elements.

The implementation of BIPV devices into PSSs has the advantage to increase their impact on the building energetic budget. In fact, the combined system may either act as a PSS, decreasing the thermal budget [20], and as a PV system, producing energy. The interest of the scientific community in this approach is testified by the coupling of BIPV technology with traditional PSS, such as: solar chimneys [21,22], solar roofs [23,24], Double Skin Façades (DSFs) [25–27] or Ventilated Façades (VFs) [28–30].

The importance of this research field is confirmed also by the trend of the global BIPV market, which is expected to expand with a compound annual grow rate of 20%, thus growing from 16.6 billion of USD (2020) to 59.5 billion of USD (2028) [31]. However, BIPV systems still represent a small share of the PV market, mainly because of the past tendence to prefer utility scale plants, or conventional roof top installations, with respect to BIPV devices.

Among various passive solar systems, DSF and VF technologies have been identified as one of the best options to reduce building thermal budget [32]. Indeed, if properly designed, their architectural flexibility allows to modify the interaction between outdoor and indoor spaces according to the building energy need [20].

This thesis describes the development of a VF coupled with an innovative and highly transparent PV panel, called Luminescent Solar Concentrator (LSC) panel. Even if, there is still little exploitation of LSC panels in this type of applications, they can be a very promising technology to be installed in vertical façades. In fact, they can be manufactured starting from intrinsic low-cost materials and they feature a much higher tolerance to partial shading with respect to standard PV modules. Moreover, their optical properties allow to drastically reduce the amount of solar cell per square meter of collecting surface and to increase the architectonic appeal of the whole system. This work was developed within a project entitled *Development of photovoltaic ventilated facade -smart skin- for the control of buildings thermal budget*, which was part of the POR FESR 2014-2020 program funded by Regione Emilia Romagna and European Union and was realized within the Photovoltaic laboratory of the University of Ferrara. A brief overview of this thesis Chapters is shown below.

The first Chapter concerns an overview on the arguments presented this thesis as well as the theoretical notions useful to easily understand the physical principles on which the employed systems are based. Following, a review on the methodology used to model thermo-fluid dynamic system is presented. In fact, in each paragraph of the second Chapter the strengths and the drawbacks of the most common models are analyzed, with the purpose to present the motivation behind the choice of a computational fluid dynamics software for the modeling of the presented systems. In the third Chapter the procedures related to the creation of the Ventilated Façade thermal model and the ones related to the LSC optical model are presented, as well as their validation thanks to the comparison with experimental measurements. Following, the fourth Chapter concerns the extension of the model previously validated, which was done by performing the retrofit of a typical building envelope for several days of both summer and winter season. Finally, conclusions are provided, and some possible future outcomes of this work are described.

CHAPTER 1

Double skin and solar façades: theory and applications

This chapter concerns an overview on the arguments of this thesis, together with the theoretical notions useful to easily understand their physical principles. In particular, as the reader can guess, the Paragraph *1.1 Ventilated Façade* addresses the aspects concerning the ventilated system, and the Paragraph *1.2 Building integrated photovoltaic* is instead focused the photovoltaic devices and their integration in buildings. Furthermore, a section dedicated to LSC panel technology is present, as it is the PV employed within this research project.

1.1 Ventilated Façade

Ventilated Façade systems are a subset of Double Skin Façade (DSF). The concept of DSF was introduced in early 1900s [33], and since then this concept has been associated to systems with the most different designs. They can be classified according to the materials, the type of ventilation, and the façade dimensions. A DSF is realized by the exploitation of two slabs separated by an air cavity, and each of these slabs is commonly called skin [16]. DSF structures are based on the exploitation of solar radiation to create a thermal gradient between the outer and inner skin, thus warming the air inside the cavity creating buoyancy phenomena. The way in which the heated air is used completely changes the system nature, in fact the cavity can be exploited as ventilation channel, when the air is used to regulate the temperature of indoor spaces, or as a buffer zone, when the still air acts as an additional insulation layer.

The first characteristic distinction between different types of DSFs is given by the optical properties of the outer skin, and the ideal façade transparency is given by an optimal balance of lighting, indoor thermal conditions, and energy consumption. In common DSFs the outer skin is usually made of glass [34] and the radiation that impinges on it is either reflected, absorbed, or transmitted. Pérez-Grande et al. [35] investigated the influence of the glass optical properties on the performance of a Double Glazed Façade (DGF), namely a DSF in which also the inner pane is glazed. They coupled glasses with different reflectance, absorbance, and transmittance values for a total of 10 combinations. If two glasses with high transmittance were coupled the heat transferred inside the building was five times more with respect to the case in which the external skin was realized with a high absorbance glass. However, the transmittance of the whole façade ranged from 0.04 to 0.17, and it could be noticed that regardless the transmittance of the single glass the whole system does not have a high transmission efficiency. This meant that despite the configuration in which the external pane had a high absorbance, a large amount of the impinging solar radiation was trapped inside the cavity and would heat up the air inside it. However, the pre-heated air inside the cavity could be employed in building Heating, Ventilation and Air Conditioning (HVAC) systems, and the cost of the building heating load could be significantly decreased. In the same work Pérez-Grande et al. also examined how the value of the mass flow rate and the average temperature of air passing through the cavity were affected by the glass optical properties. The mean temperature increase was

calculated considering as initial-ambient condition the temperature of the air at the entrance of the channel, and as final one the temperature of the air at the exit, founding a variation from 1.4 to 2 degrees. The dependency of the increase in temperature from the glass property reflected also on the air mass flow rate, since in natural ventilated façades it was driven by pressure difference due to thermal buoyancy. Even in this case, it could be seen that changing the glass property an increase in mass flow of more than 50% can be achieved.

In their work dated back to 2009 Chan et al. [36] compared the energy performance of a DSF in which glasses with different optical properties were tested and combined with various pane configurations. Four configurations were investigated in which single or double-glazed panes were installed as both external and/or internal skin. The results showed that the exploitation of a double-glazed pane increased the building thermal insulation, and the better performance was achieved by the VF implementing a single clear glass as an inner pane and a double reflective glazing as the outer pane, with a saving in annual cooling energy around 26% compared to a traditional building. In air-conditioned buildings the double glazing minimizes the building thermal loads both in cold and warmer climates. These results were confirmed also by Mingotti et al. [37], who in particular underlined that in cold climates with a low solar flux, the exploitation of a double-glazed skin reduced the need of mechanical heating, while in warmer climates with higher solar irradiation it decreased the need for building mechanical cooling.

It is therefore possible to state that for naturally ventilated DSF it is important to achieve higher air flow in the cavity by increasing the air temperature. The exploitation of a high transmittance glass as outer layer enhances this effect as a significant portion of solar radiation is exploited to increase the air temperature. If it is coupled with a double-glazed inner pane with a high thermal insulation, the radiative and conductive components of heat transfer across the whole façade are significantly reduced. If the inner skin is instead opaque, it absorbs the radiation that passes through the glazing and the emission of infrared radiation due to its temperature further increases the air temperature.

The choice of the suitable combination of glazed or opaque skins is so essential to guarantee the desired balance between the stack effect in the cavity and the heat transfer to the indoor rooms, especially in the case of natural ventilated DSFs.

The air cavity is the fulcrum of the DSF system and can serve different purposes depending on its ventilation techniques, airflow concepts and geometry. If the cavity and the skins are properly designed the DSF has the potential to significantly reduce the building energy consumption, whereas if the cavity cannot guarantee a correct balancing between air extraction and heat transmission the result is an uncomfortable indoor temperature and an additional energy consumption. The structural characteristic that most affects the flow of the air inside the cavity is its depth, which can range from few centimeters for the narrowest cavity to several meters for the widest accessible ones. The cavity depth may vary according to the different design concepts, such as the presence of shading devices or vegetation and the necessity to guarantee the access to the cavity interior [38,39]. The width of 40 cm has been defined as the threshold for the distinction between Narrow Façade and Wide Façade, as it represents the minimum depth that ensures the adequate access to the cavity for maintenance and cleaning purposes [16].

Rahmani et al. [37] and Torres et al. [34] evaluated how the DSF cavity depth affects the main parameters of these systems, namely the amount of solar heat transferred through the cavity, the temperature of the internal skin, the channel ventilation rates. The results showed that narrower cavities presented an accentuated stack effect and a stronger air movement, whereas this effect was reduced in cavities with a depth bigger than 1 m. Thus, in air-conditioned buildings narrower cavities are preferred, since the accentuated stack effect leads to a more effective extraction of the air through the cavity, which results in less energy demand for cooling the building. Larger cavities are instead preferred when the DSFs are primarily employed to increase the heat transfer towards the interior rooms. For cases in which the air extraction and heat transmission to the user room must be balanced Radhi et al. [40] recommended a cavity depth between 0.7 m and 1.2 m. However, in naturally ventilated buildings the influence of the cavity airflow on the interior of the buildings still needs investigation as the equilibrium between the ventilation rate to remove heat from the indoor spaces and the heat transfer from the cavity to the room still deserve to be examined. Oesterle et al. [41] categorized the DSFs mostly by considering the geometry of the cavity, organizing them into different categories depending on the façade height and width. The distinctions related to the cavity height are more articulated since they involve the splitting of the façade into unitary modules. The façade splitting is obtained thanks to horizontal and/or vertical partitioning, and the difference between the definitions lie on the way in which the unitary modules are connected. According to the configuration pioneered

by Oesterle et al. a VF can be categorized as Box Windows Façade (BWF), Corridor Façade (CF), Shaft Box Façade (SBF), or Multi-story Façade (MF). In BWF configuration the façade is divided in smaller and independent unitary modules by a horizontal and vertical partitioning, whereas in CFs just the horizontal partitioning is created. The SBF and MF are more complex structures in which unitary module connections are intentionally designed to increase the stack effect. Indeed, in the former sets of unitary module elements are connected via vertical shafts, which allows to create a ventilation channel as high as the whole building. In the latter neither horizontal nor vertical partitioning exists, and the cavity ventilation is obtained thanks to openings near the floor and the roof of the building. As the reader could have guessed this categorization is particularly interesting as the air channel is the actual driving force of a DSF and its ventilation properties are highly dependent on the cavity openings and on their structural combination. A drawing summarizing all the DSF categorization is presented in Figure 1.1.
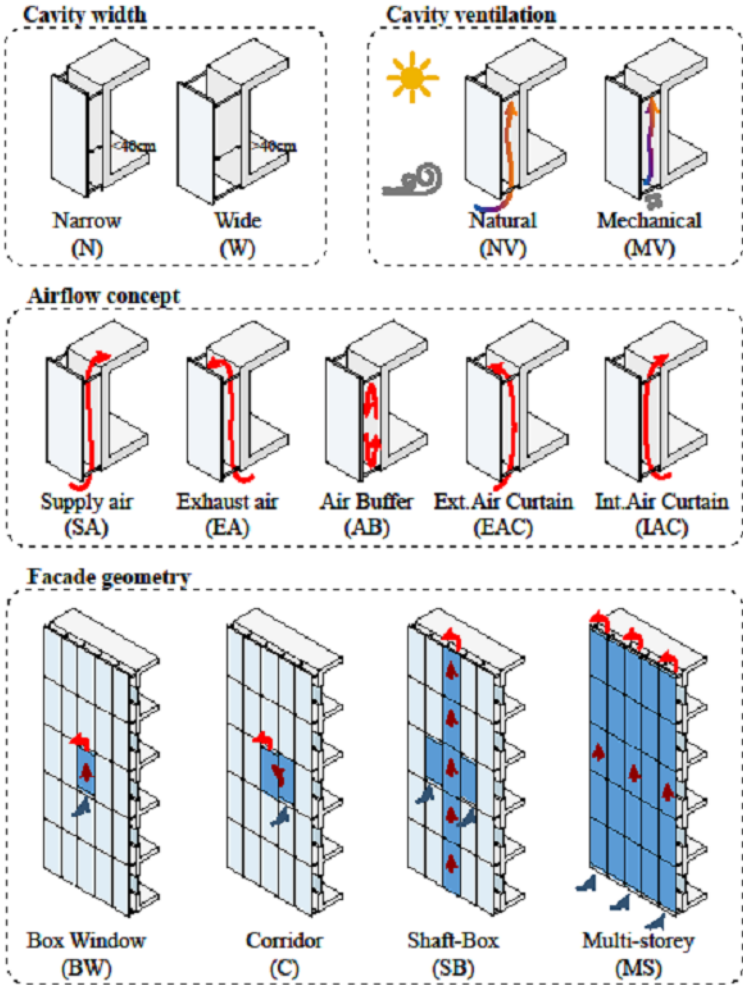
Figure 1.1 Graphical representation of the possible configurations of a Double Skin Façade.

Any VF is defined as Narrow Façade since the gap between the internal and the external skin is less than 30 cm. This type of building envelope maximizes its passive properties thanks to the exploitation of low transmittance glasses or opaque panes as external skin [42]. In Figure 1.2 an illustration which clarifies the effects of external skin transparency on the indoor spaces is presented.
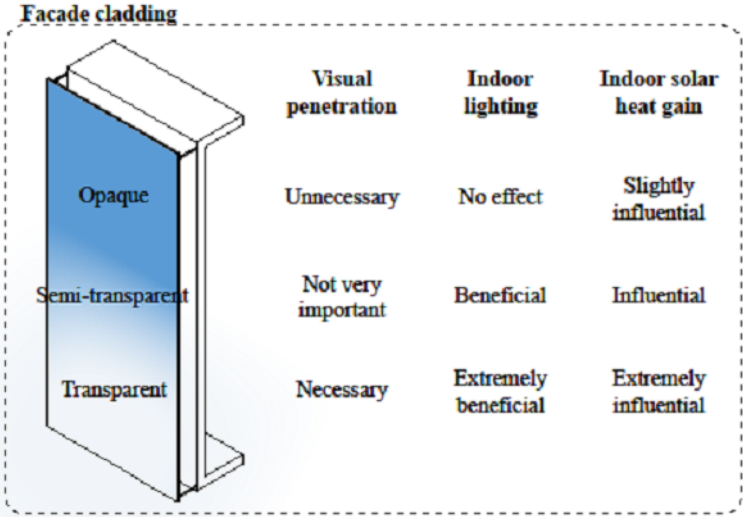
Figure 1.2 Graphical representation of the external skin transparency effect on the building indoor spaces.

The interest for VFs that implement an opaque external skin, is testified by the increase of scientific works that exploit this technology [29,43]. This kind of façades are denominated Opaque Ventilated Façades (OVFs) and they were originally developed for locations with low direct solar irradiation like Northern European countries, to protect building outer walls against atmospheric agents and prevent thermal excursion [44]. However, the possibility to implement BIPV technology in VF systems has extended their application also to Southern European locations. Indeed, as explained by Gonçalves and al. [45] this kind of systems can be seen as combined BIPV/Thermal (BIPV/T) systems, that both decrease building thermal loads and produce energy. In the case of an OVF the solar radiation warms just the external skin and the heat is transferred inside the building thanks to convection and conduction phenomena, whereas in normal VFs the solar radiation directly warms up also the inner skin and the air inside the cavity. Moreover, semitransparent external glazing allows also to exploit the greenhouse effect to heat the air inside the cavity, as the outer skin is transparent to the visible portion of the solar spectrum, but it is opaque to the thermal radiation emitted from the internal skin.

An alternative solution to change the system performance depending on the sun position or other external conditions is given by the implementation of active or passive elements, which modify the amount of solar irradiation reaching the façade internal skin. In Wide DSF this function is often delegated to shading devices, however, their introduction heavily modifies the structure of the ventilated system. Several studies, including the one of Gratia and De Herde [46] have estimated that the presence of shading devices in DSF decreases the heating loads in a range between 11.3% and 13%, depending on the façade orientation. The greatest reduction is observed for the northern DSF, since the southern wall fully benefits from the heating due to the solar radiation, while the northern one increases its insulation thanks to an additional buffer zone. On the other hand, if no natural strategy is implemented to try to decrease cooling consumption, the implementation of a DSF increases the building cooling loads of a non-negligible amount. Indeed, if no form of ventilation is applied, the presence of a VF enhances the effect of direct solar radiation on the building walls, and the heat transmission towards the building interior spaces. As in the case of the heating reduction the increase of the cooling loads depends on the façade orientation, and it reaches a maximum equal to 19.7%, for a southern DSF. Moreover, for buildings with DSF the percentage that cooling loads have on the total energy demand increases because of the creation of an additional buffer zone, so the implementation of passive or active cooling strategies becomes crucial for these types of buildings. In their study, Gratia and De Herde present the implementation of solar blinds as one of the most efficient cooling strategies, since they regulate the solar irradiance reaching the DSF inner skin, thus keeping the room cooler, and improving the thermal comfort in warmer conditions, not to mention that they can be easily combined with ventilation effects. The position of the shading device within the cavity was studied also by and Jiru et al. [47]. The blinds were simulated in three different positions: close to the DSF inner skin, close to the outer one, and in the middle of the cavity. The results showed that the temperature of the inner layer becomes higher when the solar blinds were positioned close to it. Thus, this configuration led to higher heat transfer from the cavity to indoor and consequently higher cooling loads in the user room. The influence of different blind inclination angles on the DSF thermal performance and the different heat transfer mechanisms were investigated by Ji et al. [48]. It was observed that the installation of the venetian blinds not only offered a shading function, but it also enhances the natural ventilation in the cavity. In fact, near the solar blinds the air flow conditions move from laminar to turbulent, thus increasing the upwards buoyancy momentum, and the efficiency with which the air is driven out of the

cavity. The buoyancy effect enhanced the natural ventilation in the cavity up to 35%, when angle of the blinds was 80° with the blinds in quasi vertical position. On the contrary smaller angles decrease the ventilation effect as the blinds in horizontal position obstruct the air circulation. Chou et al. [49] analyzed the impact of the window-to-wall ratio and Shading Coefficient (SC) of the glazing on energy management in buildings. They defined the SC as an indicator related to how the interior is shaded when the glazing is exposed to direct sunlight and the values of the heat transfer through the façade range from 18 W/m^2 to 59 W/m^2, when the SC varied from 0.3 to 0.7. Both works of Gratia and De Herde and Haase et al. [50] compared the effect of shading devices of different colors, in particular dark and light blinds. The results showed that the cavity equipped with darker blinds presented an air temperature 11.1 °C higher than the one with lighter blinds. The optical and mechanical properties of the implemented shading devices are then crucial to ensure the decreasing of both heating and cooling loads. In fact, the most functional shading devices are represented by adaptive technologies which can change their properties according to external conditions, like the intensity of the solar radiation, the outdoor temperature, or the temperature inside the air cavity.

In the description of ventilated systems presented so far, the role of the air inside the cavity was not examined in depth. The cavity may act as a buffer zone, when the air acts as an additional insulation layer, or as a ventilation channel, when the air inside the cavity is used for heat extraction (see Figure 1.1). This last aspect plays a key role when a standard façade is coupled with PV technologies. Lai and Hokoi work [51] classified the façade according to the role of the air inside the cavity, and they categorized DSFs into dissipative and storage façades. In both cases the air is used as heat transfer media to decrease the modules temperature and increase their life cycle and efficiency [52,53], but in the former the heated air is disperses in the external environment, whereas in the latter the it is reused within the building HVAC system. Peng et al. [54] investigated the impact of the air cavity width in a south-facing façade in Hong Kong, whose outer skin was substituted with a solar panel. They increased the channel thickness from 0.05 m to 0.25 m monitoring the system performance, the minimum of the annual heat transfer through the PV module was obtained for a width of 0.06 m.

1.1.1 Natural Ventilated Façade working principle

The ventilation in a natural VF is due to two main phenomena related to the pressure difference: the one caused directly by the wind action and the one caused by the thermal buoyancy. The former occurs when wind hits the main faces of a building. They can be identified as windward and leeward faces: the windward side is characterized by a positive pressure which pushes the air against the building or into the VF channel, whereas the leeward ones are subjected to negative pressure which results in a suction of the air away from the building. The intensity of the wind speed increases with the building height, thanks to the absence of friction with the ground level.

The buoyancy effect, also known as stack or chimney effect, is due to air thermal expansion, in fact air density decreases when its temperature raises. Therefore, hot air is lighter than cold air provided that the same volume is considered. The driving force of this phenomenon is the solar radiation impinging on the outer skin of the VF. As a result of this heat flux, the air in the channel becomes warmer than the external one, but it is in contact with the last one thanks to openings at the top and the bottom of the channel, so that a process of pressure equalization occurs. For this reason, the external air causes an over pressure at the bottom opening and forces itself into the channel. Meanwhile, the air inside the channel rises upward, thus causing an excess pressure at the top opening, where the heated air is ejected. The size of the whole effect depends on the temperature difference between the internal and external air and on the height of the channel [55]. According to Pomponi et al. [16] the pressure difference due to thermal buoyancy can be calculated according to:

$$(1.1) \quad \Delta p = \Delta \rho \cdot g \cdot \Delta h \cdot \Delta T$$

where $\Delta \rho$ is the air density change due to the temperature change, g is the gravity acceleration, Δh is the channel height and ΔT is the temperature difference between the internal and external air.

1.2 Building integrated photovoltaic

PV systems used on buildings can be classified into two main groups: Building Attached PhotoVoltaics (BAPV) and Building Integrated PhotoVoltaics (BIPV). The acronym BAPV identifies the PV devices having no direct effects on the building structure that are simply attached to the existing envelope [56]. As BIPV are instead defined the PV systems that are integrated in the building envelope and replace conventional building materials, acting also as building structural parts. According to Biyik et al [42], the parameters that need to be considered for the integration of PVs into the building envelope range from design to regulations, passing through their performance and maintenance. They summarized the key factors for BIPV system further development in low production cost, environmental impact, and high efficiency. Moreover, considering that BIPV technologies are usually installed to retrofit existing buildings, the design of easy installation systems acquires a particular importance. BIPVs devices can, in turn, be inserted in different categories depending on the employed PV technologies, or on their application. According to the first categorization they can be defined as silicon and non-silicon based devices, and according to the second as solar foils, tiles, modules or glazing; depending on the application they were designed for [57]. According to literature one of the BIPV solutions more capable of satisfying the demands of the stakeholders in is the Multifunctional PV façade. Indeed, it is a constructive solution that guarantees active and passive benefits to both buildings that need to be retrofitted, and new constructions. The high versatility of this system ensures the following advantages [42]:

1. The in-situ electricity generation decreases the losses due to energy transportation,
2. The combination between the thermal envelope benefits and the type of installed PV modules seem to ensure an energy savings within 15–35%.
3. The presence of semitransparent PV panels allows to modify daylight entrance according to the building needs.
4. Acoustic, and aesthetical benefits, as well as an increased resistance against harmful atmospheric conditions due to the presence of DSF.

However, Debije and Verbunt [58] testify that the adaptation of traditional silicon-based PV panels for urban integration presented some critical aspects. Indeed, although the recent increase of the BIPV markets has considerably widened the module offer filling the lack of available products with different colors and shapes, PV cells still remain the most

expensive component of the modules and the increase of their aesthetic appeal also carries some disadvantages. For these reasons, numerous are the studies concerning the development of aesthetical appealing or semitransparent PV panels based on Si solar cells, as for example modules in which the front glass pane has been replaced or combined with sheets of different materials [59,60]. In these modules the solar cells were covered with a white pane or veneer made of natural materials, and this retrofitting ensures a higher aesthetic appeal and a lower module temperature. An alternative solution is given by modules which consist of a layered structure composed by thin film PV [61]. Unfortunately, all these techniques reduce the module optical efficiency, and a further criticality is given by the installation site, especially in the countries with a high population density [62], as PV panels have their best performance under direct sunlight, while, because of the scattering and reflections due to other objects, in the urban environment diffuse solar radiation is dominant. The buildings and surrounding objects, such as trees, streetlights, or chimneys, can be responsible for the module shading, which is a condition that significantly reduces the performance of an extended PV system. Shading conditions not only highly affects the performance of PV strings, but they can also permanently damage the shadowed module if bypass devices are not correctly installed [63]. As for the normal skins, the opacity of the panels may vary, and their transparency is a key element for the solar energy harvesting and control. A façade made of standard flat modules is completely opaque but its transparency can be increased tanks to several approaches like interleaving standard panels with glass [64], increasing the spacing between the solar cells [65], or exploiting Thin-Film (TF) technologies [66]. The other technologies ensure the potential for low-cost fabrication and versatile applications, since the possibility to exploit metallic, plastic, or glass substrates allows to develop flexible or light-weight panels. A further improvement was presented by Kang et al. [67] that proposed the texturization of an asymmetric photovoltaic TF to increase the light-trapping and thus the panel efficiency. This solution is particularly interesting for BIPV applications, since the power produced by the panels is dependent on the incident radiation angle, which strongly deviates from the normal direction during the year. A category of PV devices that has most of the advantages presented by modules based on TF technology is represented by Luminescent Solar Concentrators (LSC) panels. They are very promising candidates for BIPV integration, since they can exploit both direct and diffuse radiation, thus presenting a high tolerance to shading [42,68]. Furthermore, thanks to their intrinsic transparency, LSC panels can be exploited also in transparent façades.

27

1.2.1 LSC panels

Luminescent Solar Concentrator (LSC) panels are concentrating photovoltaic systems that can be easily designed to be integrated in buildings, especially in transparent or semi-transparent façades. They are based on the coupling of a functionalized glass or plastic slab with PV cells, and their working principle is based on the combination of two physical phenomena: total internal reflection and fluorescence. The fluorescence phenomenon is due to the slab functionalization, and in particular to optical active centers, called fluorophores that are able to absorb a portion of the impinging light and then re-emit it at longer wavelengths. If the luminophores are uniformly dispersed inside and the slab, the fluorescence light is isotropically emitted and a portion of it undergoes total internal reflection and is guided to the slab edges. The remaining light is lost through the so-called escape-cone, namely the cone that subtend the solid angle for which the re-emitted light is refracted by the interface. Both the escape-cone losses and the amount of light entrapped in the LSC are due to the interface between the LSC slab and external air. They are regulated by laws of geometrical optics, thus they can be expressed as a function of the slab refractive index [69].
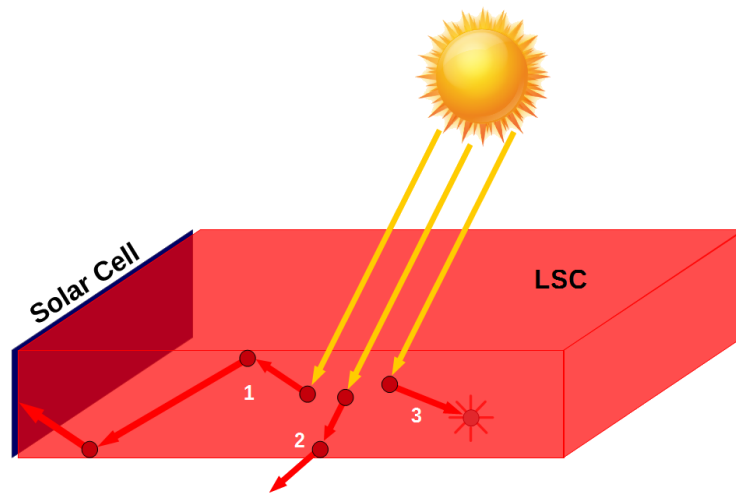
Figure 1.3 Model that describes the phenomena occurring inside an LSC. (1) the light is absorbed by a fluorophore, and it reaches the slab edge thanks to total internal reflection. (2) the light is absorbed by a fluorophore, but it is subjected to escape cone losses. 3 the fluorescence radiation is absorbed by another dye molecule (self-absorption).

The nature of the fluorophores can be different. Indeed, as functionalizing material, organic, metal-organic, and quantum dots can be exploited. The organic dyes represent the cheapest solution, but they suffer from a considerable degradation under UV radiation and a

significant superposition between the absorption and emission spectrum. This superposition means that the luminophores can also absorb fluorescence light, thus increasing the number of re-emission events and the probability of escape-cone losses. In Figure 1.3 a model that clarifies the phenomena occurring inside an LSC is depicted. This problem can be partially resolved exploiting quantum dots as luminophores; because of electron quantum confinement, resulting in a quantized energy spectrum [70] quantum dots exhibit a negligible superposition between absorption and fluorescence spectrum. A similar result can be also obtained thanks to the introduction of metallic or rare-earth ions in the dye molecular complex [71]. The implementation of metal nanoparticles can be useful also to exploit surface plasmon resonance in the visible region, which increases the quantum yield of fluorophores in this portion of the electromagnetic spectrum [72]. These solutions ensure high stability, nearly zero self-absorption, and high quantum yield luminophores. However, they are often exploitable just for small dimension LSC panels, as their high cost strongly affects the price-to-watt ratio of the whole panel.

The last component that affects the LSC cost and performance is the PV cell placement and nature, since they collect the fluorescent light that is trapped inside the slab thanks to total internal reflection. There are several examples in literature in which spectrally matched PV cells or trench reflector, and photonic mirror are exploited to increase the panel efficiency [73,74]. In the case of more performant fluorophores, the cost of high-performance PV cells limits the industrial scalability of LSC panels, and nowadays their price-to-watt ratio is not competitive with commercial BIPV technologies. Rafiee et al. work [75] testifies that despite there is a clear understanding of the combination that led to the highest efficiency LSC panels, the more scalable ones are those based on organic dyes and Si solar cells. In fact, fluorophores realize a down-shifting of wavelengths that cross the slab, which ensures to expose Si solar cells to a wavelength range in which their External Quantum Efficiency (EQE) is higher than the average EQE under the solar spectrum, thus leading to a performance increase.

1.2.2 Luminescent Solar Concentrator panel working principle

The portion of the fluorescence light that is trapped inside the slab is a function of its refractive index. According to Snell's law, all photons approaching an interface between the slab surface and the air at an angle higher than the critical one will be totally reflected. The critical angle for the air/LSC interface can be defined as:

$$(1.1) \quad \vartheta_C = sin^{-1}\left(\frac{1}{n}\right)$$

where the air refractive index has been approximated to 1, and n is the slab refractive index. Considering that the materials used as matrix for the slab typically have a refractive index between 1.4 and 1.6 approximately 25% of the re-emitted photons will be lost because of escape-cone losses, whereas 75% will be subjected to total internal reflection. These photons will be waveguided to the LSC sides and then converted to electricity by the PV cells. The efficiency of the whole panel can be divided in two major components, the optical, η_{opt}, and electrical, η_{PV}, efficiency. The optical efficiency is a function of the slab properties and can be expressed as:

$$(1.2) \quad \eta_{opt} = T \cdot P_{tir} \cdot \eta_{slab} \cdot \eta_{abs} \cdot \eta_{PQY} \cdot \eta_{SA}$$

where T is the slab transmittance, P_{tir} is the total internal reflection efficiency, and as mentioned above it depends on the slab refractive index. η_{slab} is the slab transport efficiency and depends on the flatness and smoothness of the surfaces. η_{abs} is the absorption efficiency of the fluorescent dye, and it can be estimated from the fluorophore absorption spectrum. η_{PQY} is the photoluminescent quantum yield of the dye, which for the one employed in this thesis was equal to 95%. Finally, η_{SA} is related to the photons loss due to re-absorption phenomena during the light transport inside the slab.

The electrical efficiency is instead function of the solar cell conversion efficiency. Solar cells are based on semiconductor materials, and the useful parameters to evaluate their efficiency are the Spectral Response (SR), and the EQE. The SR is a curve describing the ratio of the current generated by the solar cell to the power incident on the cell itself, as a function of the wavelength, while the EQE compares the number of charge carriers collected form the solar cell with the number of photons incident on the device. The ideal SR increases linearly with the wavelengths until a cut off value after which it becomes zero.

The SR decreases for photons of short wavelengths, since at these wavelengths each photon has a large energy and hence the ratio of photon energy to power produced by the cell tends to zero. In fact, highly energetic photons cede their excess energy under the form of kinetic energy, which is dissipated as heat, through a process called thermalization that leads to an increase in the system temperature, without contributing to current production. The low energy cut off wavelength, which is usually called *threshold wavelength*, is defined as $\lambda_T = hc/E_G$, where h is the Planck's constant, c is the speed of light in vacuum and E_G is the energy band gap of the semiconductor used in the solar cell. The phenomenon is due to the inability of a semiconductor to absorb photons with energies lower than their band gap. This limit is therefore present also in the EQE curve that for an ideal cell is a step function, which takes it maximum value for $\lambda < \lambda_T$ and it is zero for $\lambda > \lambda_T$. The maximum value depends once again on the semiconductor employed in the PV cell. The EQE of real solar cells has a further cut off wavelength on the shorter wavelength range that is due to the cell thickness, in fact, even if the semiconductor can absorb photons with that specific energy, the cell could be too thick to efficiently convert it into electrons. The maximum quantum efficiency of silicon solar cells lies in the range from 500 nm to 800 nm, and their efficiency may vary from 16%, for polycrystalline silicon cells to 24% for monocrystalline silicon cell. The efficiency range is so wide because it depends on several factors, such as, purity of the crystal, doping concentration and shape of the contact with the external circuit.

CHAPTER 2

Numerical modelling of Ventilated Facades: state of the art

In this chapter a review on the methodology used to model DSF and VF systems is presented, and in each paragraph the strengths and the drawbacks of the several methods are analyzed. In fact, the purpose of this chapter is an in-depth depiction of existing models, with the intention to present the reasons that led to the choice of a computational fluid dynamics software for the modeling of the VF presented in this thesis.

2.1 Ventilated Façade Modeling

During the last decade, various ways to model the behavior of ventilated systems have been proposed. The ancient approaches were based on numerous assumptions and constrains, but they were able to provide the necessary information with very few computational resources. Modern computational machines allow the exploitation of more complex numerical models, which can describe the modeled systems with such a high degree of detail that nowadays numerical modeling became essential for the design and development of these systems. However, this approach needs to be coupled with data acquisition campaigns, both to better understand the behavior of these systems and to offer data that validate the created models [76–78]. Analytical models, lumped models, non-dimensional analysis, network and control volume models, zonal approach, and Computational Fluid Dynamics (CFD) are the methods used to numerically evaluate the performance of VF systems, which will be presented on this chapter.

2.2.1 Analytical and lumped models

If compared with other methods, analytical and lumped models can provide the essential information for the design of a VF employing very few computational resources. In analytical models the investigated physical quantities are calculated via mathematical equations, however they can be solved only under a considerable number of assumptions constrains. The lumped models are used to describe the behavior of spatially distributed physical systems by using a topology consisting of discrete lumps and assuming that the temperature difference inside each lump is negligible. The main drawback is that lumped models require the imposition of a constant temperature at the façade skins and cavity. These premises are confirmed by the first generation of numerical models that try to describe DSFs behaviors with simple one-dimensional analytical methods and empirical correlations. Moreover, Park e al. work [79,80] highlighted how the calibration process plays an important role in the performance of lumped models based on descriptions of physical processes. According to this, instead of using empirical correlations from the literature, the model presented in this work was calibrated using parameters acquired in a dedicated data acquisition campaign, and the calibration process highly improved the model accuracy in comparison to the experimental data. Rheault and Bilgen work [81] represents

an example of how tightening can be the boundary conditions necessary to solve a model developed with lumped element method. The model investigated the heat transfer across an automated venetian blind window system and the analysis was carried out under the following assumptions:

1. the heat transfer was unidimensional and only temperature gradient along the x direction was considered,
2. except for the one ruled by the room temperature, the heat exchanges were modeled as stationary during the considered time interval,
3. material properties are evaluated thanks to their average values, or they are modeled as constant,
4. each element of the subsystem is considered isothermal,
5. the lateral heat losses can be neglected,
6. within the infrared radiation band, the whole system is considered as a gray body,
7. the radiative heat exchange of the room walls was modeled as if they had been at indoor air temperature.

2.2.2 Non dimensional analysis method

Non-dimensional analysis is a powerful analytical technique to study physical and thermodynamic processes. Since its application reduces the degrees of freedom of the problem to the minimum, it is presented as a basic tool to evaluate some specific parameters. The key tool of non-dimensional analysis is the Buckingham π-theorem, which represents a general solution method for complex problems. This theorem allows to create the so-called *similarity parameters*, non-dimensional numbers that correlate the problem dependent variables, thus reducing the independent variables necessary to describe them. A further advantage is that if a problem can be described by using dimensionless variables, these same parameters can describe that problem at all scales, thus generating the most economical scaling laws. For the perspective concerning this thesis, the relevant physical parameter corresponds to the heat transfer to the channel throughout the wall. The results presented in Balocco's work testified how non-dimensional analysis cold be employed to estimate the thermal performance of a naturally [82] and mechanically [83] ventilated façade. The resulting correlations were validated by means of CFD simulations and experimental data, and both proved to be valid under several different conditions. The study

revealed that for the naturally ventilated façade the complete heat transfer process can be described by 18-dimensional variables, and that the whole set of variables depended only on 4 fundamental dimensions. For the model developed by Balocco the Buckingham π-theorem allowed to exploit the 4 fundamental demotions to create 14 non-dimensional numbers. These variables allowed to correlate the total heat flux to an equation defined as follow:

$$(2.1) \quad M1 = a \cdot M2^b \cdot M3^c \cdot M4^d \cdot M5^e \cdot M6^f \cdot M7^g \cdot M8^h \cdot M9^i \cdot M10^l \cdot M11^m \cdot M12^n \cdot M13^p \cdot M14^q$$

where $M1 \ldots M14$, are the 14 non-dimensional numbers estimated with the Buckingham's theorem, whereas the constants, from a to q have been determined and validated by using the least square correlation method. For the mechanically ventilated façade just 12 non-dimensional numbers were sufficient to describe the system thermal performance and to correlate the model whit experimental data. The computational resources demanded by this method are comparable with the ones needed by analytical and lumped model, but as before they come at the cost of very strong assumptions. In fact, for example the air density is the only thermo-physical property that the model developed by Balocco considers dependent from temperature or pressure conditions.

2.2.3 Airflow network model

As stated by Hensen [84], airflow network modeling is exploited to resolve bulk flows parameters. The high similarity between the thermal and electrical systems allows to employ widely utilized basic rules for balancing networks, such as Ohm's Law and Kirchhoff's Laws, also for thermal networks. To apply numerical methods in the solution of the partial differential equations describing a thermal network, the system must be partitioned into a number of finite volumes called nodes. The essential characteristics of each node are its temperature and capacitance (thermal mass), which are simulated as if they were concentrated at the center of the considered finite volume. A network flow analysis is usually implemented in complex physical system especially if they presents many inlets, outlets, internal flow branching, pressure differences, or discharge coefficients for easy cross ventilation [85]. The whole system is connected by internodal connections representing all the elements that generate distributed flow paths, as doors, pipes, pumps, or

ducts. The temperature of each volume, T, represents its average value, and in a system composed by a homogeneous material its temperature is estimated by interpolation between nearby nodal sites. The temperature T is used also to define the node capacitance, C, as it is computed from the thermophysical parameters of the sub-volume material at that specific temperature. The capacitance of a node is a useful parameter to define its nature since it is related to the node thermal mass. The sub-volumes with finite capacitance are usually exploited to represent diffusion nodes, since the energy variation of these nodes is determined by their capacitance value C, and the net heat that flows into the node, $\dot{Q}$. They can be defined by the following equation:

$$(2.2) \quad \sum \dot{Q} - \frac{C \cdot \Delta T}{t} = 0$$

where t is the time over which the heat is flowing, and the capacitance of a node is defined as $C = \rho \cdot V \cdot c_p$. In the last equation V is the nodal volume, and ρ and c_p are the material density and specific heat respectively. In Equation (2.2) both ρ and c_p are considered temperature dependent properties since they may highly vary with the temperature.

Another category of nodes consists of arithmetic nodes, which resemble nodes with $C = 0$. Although zero capacitance could represent a physical unreal quantity, their successful utilization with numerical solutions frequently aids in the interpretation of surface temperatures, and node coupling temperatures. They can also be useful for representing thermal system components with low capacitance compared to the rest of the system, thus decreasing the simulation computational time without a significant change in the simulation overall accuracy. Therefore, when compared to the overall number of nodes in the network, arithmetic nodes should be few. Small components such as bolts, films, or fillets, or low mass insulations are perfect examples of this kind of nodes. They can be defined by the following equation:

$$(2.2) \quad \sum \dot{Q} = 0$$

as can be seen by Equation (2.2), because of their low capacitance, the temperature of arithmetic nodes changes instantaneously with its surroundings.

The last type of nodes, called border nodes, are used to represent thermal components with infinite capacitance. They are usually employed within a thermal network to model constant

temperature sources, such as reference temperature, recovery temperature, and surfaces at constant temperature. A border node is defined by the following equation:

$$(2.3) \quad T = constant$$

Equation (2.3) states that boundary nodes can be used to model entities of constant temperature that can between points, lines or surfaces depending on whether the model is one, two, or three dimensional. A typical application is the modeling of exterior surfaces, where the temperature remains very close to the radiation equilibrium with the surface heating rate. Obviously the modulization of all the boundaries that are at the same temperature can be implemented with a single boundary node.

Regardless of the type of node, the location of the node center and their shape are determined by considering the several simulation constrains, among which the most relevant are: the position in which the temperature must be evaluated, the structural design, the expected temperature distribution, and the desired accuracy.

The difference between the dimension of finite size nodes compared to real infinitesimal volumes is the main source of approximations in the simulation results, but they are influenced also by the material thermal properties, the boundary constraints, the node center locations, and the time increment of transient computation. If the approximation introduced by the node size is consistent with the intended results, the diffusion node shape is selected to be a basic geometric figure with easily computed areas and volumes, even if they represent irregularly shaped physical elements. In these circumstances the mass centroids of the nodes are presumed to represent the node centers, however there are cases in which the nodal division is decided first, and the node center positions are specified as a result. The last possibility is the one in which the position of the node centers is dictated by output needs with nodal borders assigned as a constraint.

An example of this approach is given by the work of Ioannidis et al. [86] that presented the numerical model of a double skin façade integrating photovoltaic panels and automated roller shades. The approach used in this work was based on a detailed transient finite difference thermal network, and in order to isolate the optical and thermal properties of each component, the whole system was represented with several distinct entities. Each element of the whole system was, in turn, divided in N equal control volumes along the vertical direction, with the perimetral thermal zones further subdivided into Z different sub-

elements, so that the air gradient along the channel could be captured. The temperatures of the façade elements were therefore calculated through the energy balance method at each time step t, for each $z-$ th perimeter zone and for each $n-$ th control volume. Haase et al. [50] developed a model to estimate how orientation, window to wall factor and glazing types could influence the performance of a DSF. The model was validated with experimental data related to hot and humid climates. Gratia and De Herde [87] deeply studied the thermal performance of a naturally ventilated façade using a software for thermal analysis of buildings in which the airflow network model is coupled with an energy simulation algorithm. The energy performance of VF systems was also simulated by using the building energy modeling tool EnergyPlus. Indeed, the VF channel can be easily simulated by dividing it into sub-zones, and by describing each zone with an airflow network model [36,88].

Despite the remarkable results presented in literature, this approach presents several limits: in fact, in order to solve the heat balance at each node it usually needs to be integrated with thermal network, and it cannot provide detailed information on the flow field nature, for which CFD simulations are required [89]. Furthermore, if airflow network modeling is used to analyze the thermal performance of the VF when integrated into a building, the building thermal model must be integrated within the thermal and airflow models of the VF. The whole model must account for the pressure difference between the channel inlet and outlet, due to the wind or to the buoyancy effect. This is confirmed by the work of Stec and van Passen [90], who also demonstrated that the HVAC system should be integrated in the façade.

2.2.4 Control Volume approach

With this kind of approach, the VF skins are coupled only thanks to the air cavity, and each of them is subdivided in so-called control volumes. A control volume is an artificial representation that resembles the real volume of interest, and it could have a velocity equal to zero if it is used to model fixed objects or stationary fluids, or it could move with a constant velocity equal to that of the surrounding fluid. If the studied system is a solid or a fluid in steady state condition, the control volume mass remains constant, whereas if the modeled system is a flowing fluid, the constant quantity is the mass flow rate, i.e., the mass that enters the control volume is equal to the mass that leaves it. Therefore, for a VF, the

mass flow rate of each control volume must be equal to the mass inlet flow rate [89]. The other interesting physical quantity for thermodynamics simulations is the control volume energy: if no heat is transferred to the control volume its energy remains constant, whereas if the control volume is subjected to an energy flow its total energy may vary, but this variation must be equal to the difference between the incoming and the outgoing energy. As in the case of airflow network modeling, this methodology allows to consider the thermal gradient driven by buoyancy phenomena that are present inside the cavity. An algorithm based on this approach was developed by Faggembau et al. [91], they validated their algorithm thanks to experimental measurements, and analytical solutions where possible. Moreover, the implementation of control volume method in the Transient System Simulation Tool (TRNSYS) combined with experimental data and a sensitivity numerical study, let Saelens et al. [92–94] to underline that this kind of approach is particularly suitable to estimate the energy efficiency of the whole façade, as the air flow rate and the recovery of air returning from the VF are well modeled by control strategies.

2.2.5 Zonal approach

This representation was developed in 2008 by Jiru and Haghighat [95] specifically to estimate the thermal performance of a DSF. It is a hybrid approach that the authors validated thanks to experimental results, which collocates in the middle between lumped model and CFD. In the zonal approach the VF is divided into control volumes with dimensions larger than the cells used by CFD models, the resulting equations are therefore smaller and easier to solve if compared to the ones presented in CFD models. Moreover, the thermodynamic representation contains more information if compared to the one obtained with lumped or the control volume approach, but it requires reduced computational resources with respect to CFD models. Jiru and Haghighat formulated both mass and energy conservation equations for each cell as follow:

$$(2.4) \quad \sum_{=1}^{n} m_j - S_M = 0$$

$$(2.5) \quad \sum_{j=1}^{n} Q_j - S_q = 0$$

where m_j is the mass flow rate, S_M is the mass source, Q_j is the heat flow and S_q is the heat source.

2.2.6 Computational Fluid Dynamic methods

CFD methods consist of a branch of numerical methods employed to solve Partial Differential Equations (PDEs) that characterize the thermodynamic problem. These methods numerically solve the PDEs by replacing them with algebraic equations, and the most traditional ones will be presented in this work. The former is the Finite Difference Method (FDM) that, as it is suggested by the name, solves the algebraic equations by approximating spatial, or time derivatives with finite differences. In fact, depending on the nature of the simulation, the spatial domain and/or the time interval are discretized into a finite number of elements, with the equations solved in correspondence of each of these specific elements [96]. This method generates an error, which is called the discretization error, given by the difference between the numerical solution and the exact one and directly correlated with the error passing from a differential to a difference operator. The smaller it is the difference between two consecutive elements, the higher is the solution quality, but unfortunately it also increases the simulation duration. Large time steps are useful for increasing simulation speed in practice, but at the cost of a reduction in data quality. A second kind of CFD method is the Finite Element Method (FEM) that solves the algebraic equations related to the problem by a particular space discretization, i.e., the mesh construction of the object. The mesh is the numerical domain in which the solution is computed, and its element are called finite elements. In particular, the solution is computed at the nodal points, which are the connection points between the finite elements, and then interpolated inside each finite element [97]. If the chosen mesh is too coarse the simulation results may depend on the mesh element number, thus, to ensure that the obtained results are independent of the chosen mesh, a process called mesh refinement must be performed. This consists in a progressive increase of the number of the mesh elements, until the simulated results are independent from the mesh element number. Unfortunately, the mesh tightening increases both the quality of the results and the time required for the simulation, so the coarser mesh for which the independency is guaranteed is usually chosen as the best performing one. The latter CFD is the Finite Volume Method (FVM), similarly to the previous method, the FVM discretizes the physical domain into non-overlapping elements or finite volumes. This method is strictly conservative, since the flux entering a given volume must coincide with the sum of the fluxes leaving the adjacent volumes [98]. The algebraic equations associated to the problem are then solved to compute the values of the dependent variable for each control volume. However, in contrast with the previous

methods that evaluate the solution at specific points and then interpolates the obtained results, this method approximates the solution by evaluating the exact expressions of the average value of the solution over some volume [99]. As in the case of FDM, the error on the simulated results can be associated to the discretization error and can be decreased with the same procedure [100].

The high versatility of CFD methods combined with the increase of computing power rapidly spread their exploitation as modeling technique, so that nowadays are extended far beyond their classic use for the extraction and confirmation of empirical correlations, or the determination of the convective heat transfer coefficients. One of the first examples is given by Borgers and Akbari's work, in which a FDM is used to describe the natural air flow between two vertical plates. The model allows to extract empirical correlations that can describe the flow rate inside the cavity both for laminar and turbulent fluid flow [101]. Yedder et al [102] numerically analyzed how a constant radiative heat flux on the system affects the channel natural convection and Mootz and Bezian studied how the heat transferred by convection depend on the channel depth [103]. However, in the last decade, the awareness that the efficiency of DSF may depend on numerous parameters moved the use of CDF models beyond from the calculation of convective heat transfer coefficient to the study, evaluation and comparison of the thermodynamic behavior of different types of DSF [104–107]. Moreover, the increasing popularity of shading devices or vegetation inside the cavity make CFD simulations the only tools able to describe the nature of flow field [108,109].

CHAPTER 3

Model development and validation

In this chapter the procedures used to create the thermal model of the whole VF and the ones related to the LSC optical model are presented. In particular, in Paragraph *3.1 LSC characterization* the experimental apparatus and the modeling techniques adopted to estimate LSC absorption coefficient are described. This estimation allows to understand the distance traveled by the light inside the slab, understanding if large area LSC panels can be exploited to produce energy. The following paragraphs concern the development of the VF thermal model and its validation thanks to the comparison with experimental measurements.

3.1 LSC characterization

3.1.1 LSC optical performance

As mentioned in the Paragraph *1.2.1 LSC panels* the most suitable LSC panels for BIPV applications are based on organic dyes and Si solar cells [75], however as is evident also from Figure 3.1 this kind of dyes usually presents a considerable superposition between the absorption and emission spectrum. A high self-absorption can drastically decrease the amount of radiation that reaches the PV cells mounted on the LSC, especially for large area devices; thus a further study to understand if LSC based on organic dyes could be exploited in the building sector was therefore necessary. To evaluate how the self-absorption phenomena affects the fluorescent light propagation inside a large area LSC an analysis on the output spectrum of a luminescent slab was performed. The analysis was carried out by analyzing the collected data with Matlab to obtain the absorption coefficient for each wavelength. The measurements were performed with a laser and an optic fiber in a dark room. The tested LSCs consisted of 50 x 50 x 0.5 cm^3 plastic slabs, made of PMMA (PolyMethylMethAcrylate) and doped with Lumogen® Red 305, which is a perylene-based organic dye developed by BASF Corporation [110]; Figure 3.1 shows the Lumogen® Red 305 absorption and emission (fluorescence) spectra.
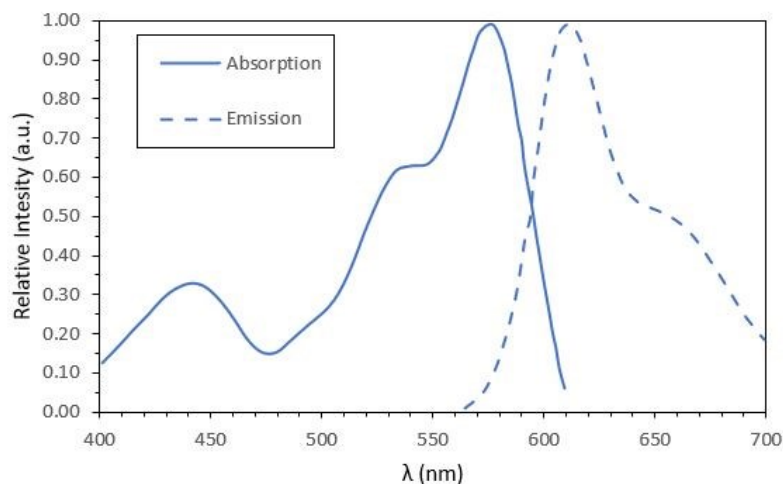
Figure 3.1 Lumogen® Red 305 absorption and emission spectra.

The region between 560 nm and 610 nm corresponds to the wavelength range in which the self absorption phenomena can occur. The tests were performed on samples doped with a dye concentration of 300 ppm and 160 ppm. The choice of the slab dimensions was guided by two main aspects: the results presented by Bernardoni et al. [68] and the minimum

dimension of semitransparent glass or plastic slabs employed in the building sector. They demonstrated that the spectral components affected by auto absorption are completely removed from the fluorescence spectrum already for slabs with dimension of 25 x 25 cm^2, however their small dimension severely limits their use in the building sector. A slab of 50 cm side has a characteristic dimension that is more compatible with that of typical building components, as for example windows or greenhouses cover modules. The experimental measurements were performed in a dark room by illuminating the LSC slab from above only with a Collimated Laser Module CPS450, manufactured by Thorlabs. This was chosen as light source since it ensured an almost monochromatic light beam, with an emission peak wavelength of 455 nm, and an elliptical aperture of 3.2 mm x 1.0 mm. The laser was used to illuminate the largest face of the LSC, whereas the optic fiber was coupled with an edge of the slab, so that if the laser beam is kept in front of the optic fiber edge it collects only the light generated by the fluorescent dye in the volume of LSC and not the light generated by laser itself.

Figure 3.2 Scheme (top) and picture (bottom) of the measurement system.

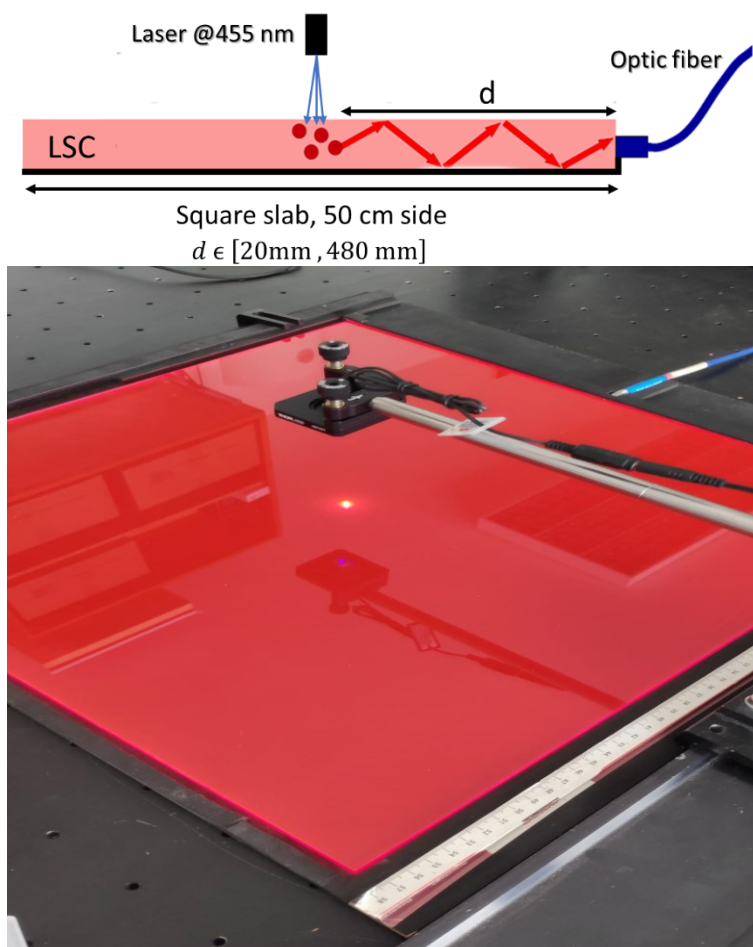The experimental apparatus was built on purpose and consisted in a bench housing the LSC slab and a moving arm useful to support and move the laser. The light source was progressively distanced from the slab edge with the optic fiber, ranging from a distance of 20 mm to 480 mm. The chosen step-size was 5 mm for distances between 20 mm and 270 mm, which was increased to 10 mm for the remaining measurements. In Figure 3.2 a picture of and a scheme of the measurement system are displayed. The slab output spectrum was collected by using a quartz optic fiber with a diameter of 400 nm and an angular acceptance of 25°. An extremity of the fiber was housed in the bench and optically coupled with the edge of the slab, the other one was coupled to a spectrometer via a SMA905 connector. An Ocean Optics USB4000-XR1-ES spectrometer with an UV-VIS-NIR sampling range from 195 nm to 1055 nm, allowed to collect information about the spectral distribution and global intensity of the emerging light. The choice of smaller size steps for the shorter distances was due to two main reasons: the first was the limited angular aperture of the optic fiber, and the second was the higher decrease in intensity when the laser was closer to the detector. This allowed the exclusion of those distances for which not all the light source, considered as the emission of both the laser and the fluorescence halo, was included in the fiber angular aperture. Thanks to this precaution it was possible to considerably simplify the data analysis, which was developed by applying the Lambert-Beer law although neither the emitter nor the receiver could be considered as point-like objects. The LSCs used in this work are systems with a uniform thickness hence a 2D approximation could be applied, and the influence of the thickness can be implemented in the data analysis as a correction factor. The Lambert-Beer law relates the attenuation of light to the properties of the material through which the light is travelling and if both the emitter and the receiver can be approximated as point like objects, the law can be expressed as:

$$(3.1) \quad I = I_0 \cdot e^{-\alpha \cdot z}$$

where I is the intensity of the light exiting the material, I_0 is the light intensity entering the material, α is the absorption coefficient and z is the path length that the light travels through the material. Equation (3.1) is valid for materials whose α is constant within the path traveled inside the material. However, in case the absorption coefficient was function of the traveled path a further integral on z must be performed.

If we want to apply this law to a two-dimensional system in which neither the emitter nor the receiver can be considered as point-like objects Equation (3.1) must be expressed as:

$$(3.2) \quad I = I_0 \int_{-w/2}^{w/2} \int_{-h/2}^{h/2} \int_{-h'/2}^{h'/2} \frac{(d+x)e^{-\alpha\sqrt{(d+x)^2+(y-y')^2}}}{2\pi h((d+x)^2+(y-y')^2)} dx\,dy\,dy'$$

where I, I_0 and α are defined as in Equation (3.1), w and h are the width and the height of the laser beam, h′ is the diameter of the optic fiber, d is the distance between the LSC edge and the center of the laser beam. x and y correspond to the coordinates of a point inside the ellipse projected by the laser and they can range from $-w/2$ to $w/2$ and from $-h/2$ to $h/2$ respectively. y' is a point within the fiber diameter and it can range between $-$ h′$/2$ and h′$/2$.

The LSC thickness influences the average path length traveled by light inside the slab, and this length depends on the emission angle calculated from the normal to the LSC surface. If we consider a distance d between the light source and the detector, the shortest path is a straight line from the emission point to the optic fiber, namely d, and it corresponds to an emission angle ϑ equal to $\pi/2$. The longest path is, instead, travelled by the light emitted with an angle ϑ just above the critical one ϑ_C, as the emitted light is subjected to the maximum number of reflections before reaching the detector. The average path is therefore represented by the ratio between d and the sine of the average emission angle. Since the angular distribution is uniform, the probability of emission between two angles, $P_{\Delta\vartheta}$, can be express thanks to the cosine rule, namely: $P_{\Delta\vartheta} = cos(\vartheta_{avg}) = = (cos(\vartheta_{min}) - cos(\vartheta_{max}))/2;$ where in particular, ϑ_{min} corresponds to ϑ_C and ϑ_{max} to $\pi/2$, since the shorter path is parallel to the slab surface. Moreover, considering PMMA optical properties, $n = 1.489$ at 633 nm, and the possibility to express ϑ_C by using Equation (1.2), the correction factor that accounts for the contribution of the LSC thickness to the average optical path length becomes:

$$(3.3) \quad Th = \frac{1}{sin(\vartheta_{avg})} = \frac{1}{sin[arcos(P_{\Delta\vartheta})]} = \frac{1}{\sqrt{1-P_{\Delta\vartheta}^2}} = \frac{1}{\sqrt{3+\frac{1}{n^2}}} \approx 1.077$$

Figure 3.3 (a) and (b) shows the intensity spectrum registered at different distances against wavelength for a dye concentration of 300 ppm and 160 ppm respectively.
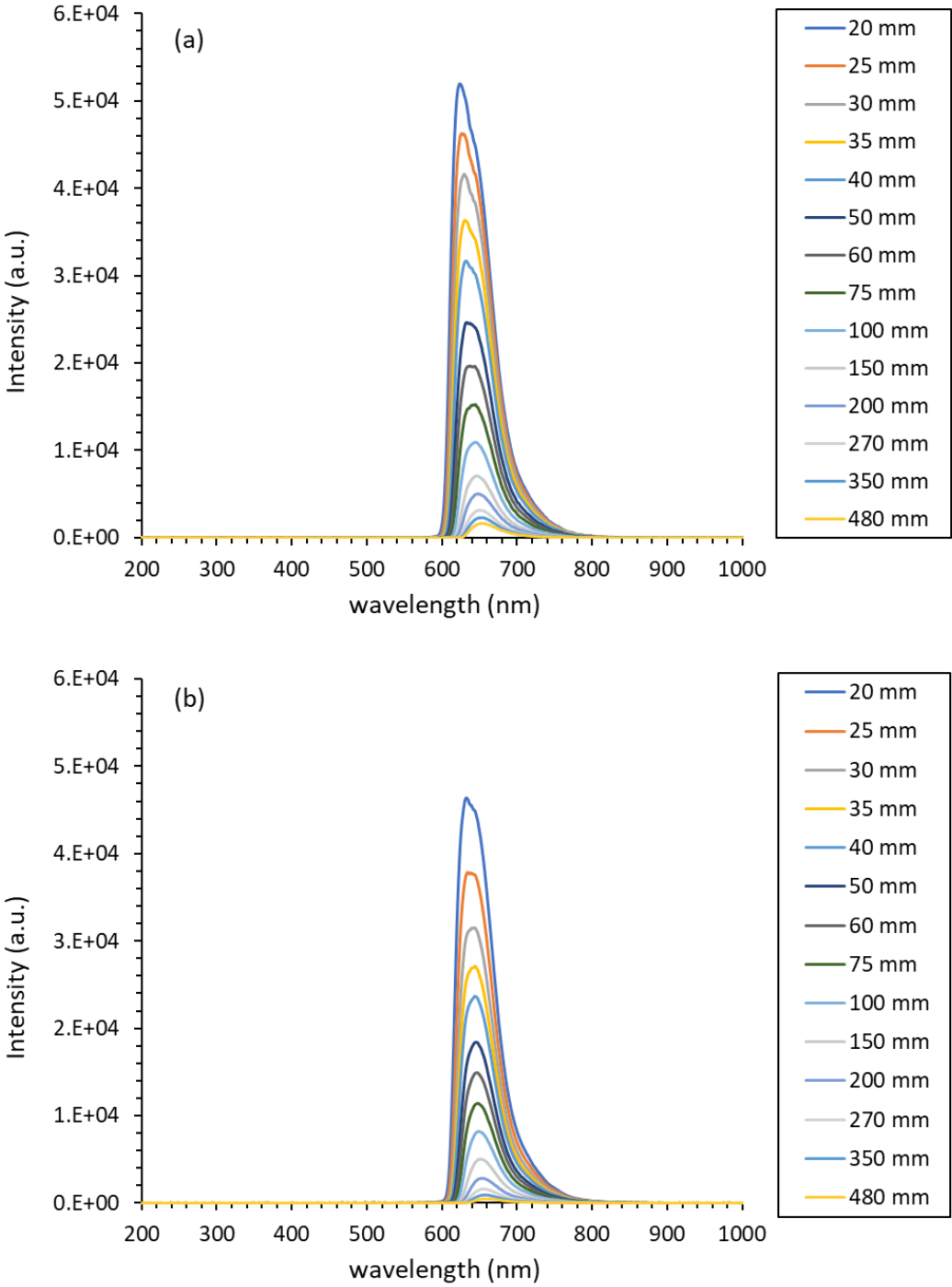
Figure 3.3 Measured intensity against the distance between the spot-light and the optic fiber for a dye concentration of (a) 300 ppm and (b) 160 ppm.

From the results presented by these plots it seems that the LSC with a dye concentration of 300 ppm is more efficient, since its fluorescence spectrum has a higher intensity for the same distance between emitter and receiver. The following analysis aims to investigate this aspect. The data analysis consisted of the following steps:

1. firstly, a selection on the wavelength of the collected light was made,
2. each wavelength was then expressed against the distance between the laser and the optic fiber d,
3. the obtained results were then fitted by using Equation (3.1).
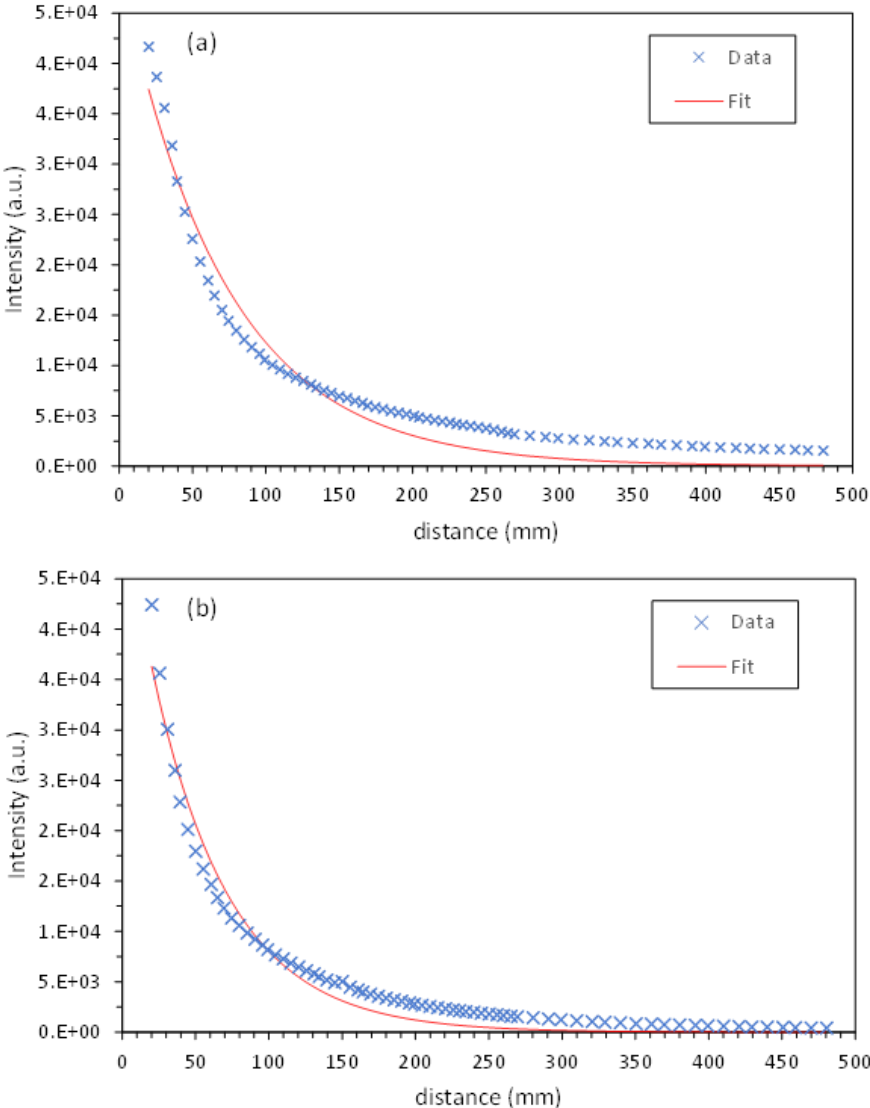
Figure 3.4 Measured intensity at 650 nm as function of the distance between the laser and the optic fiber for a dye concentration of (a) 300 ppm and (b) 160 ppm.

In Figure 3.4(a) and (b) the intensity measured at 650 nm for both dye concentrations as function of the distance between the laser and the optic fiber, as well as the obtained fit, are shown. The choice of this wavelength as example one was driven by the necessity of selecting an emission wavelength outside the dye absorption spectrum.
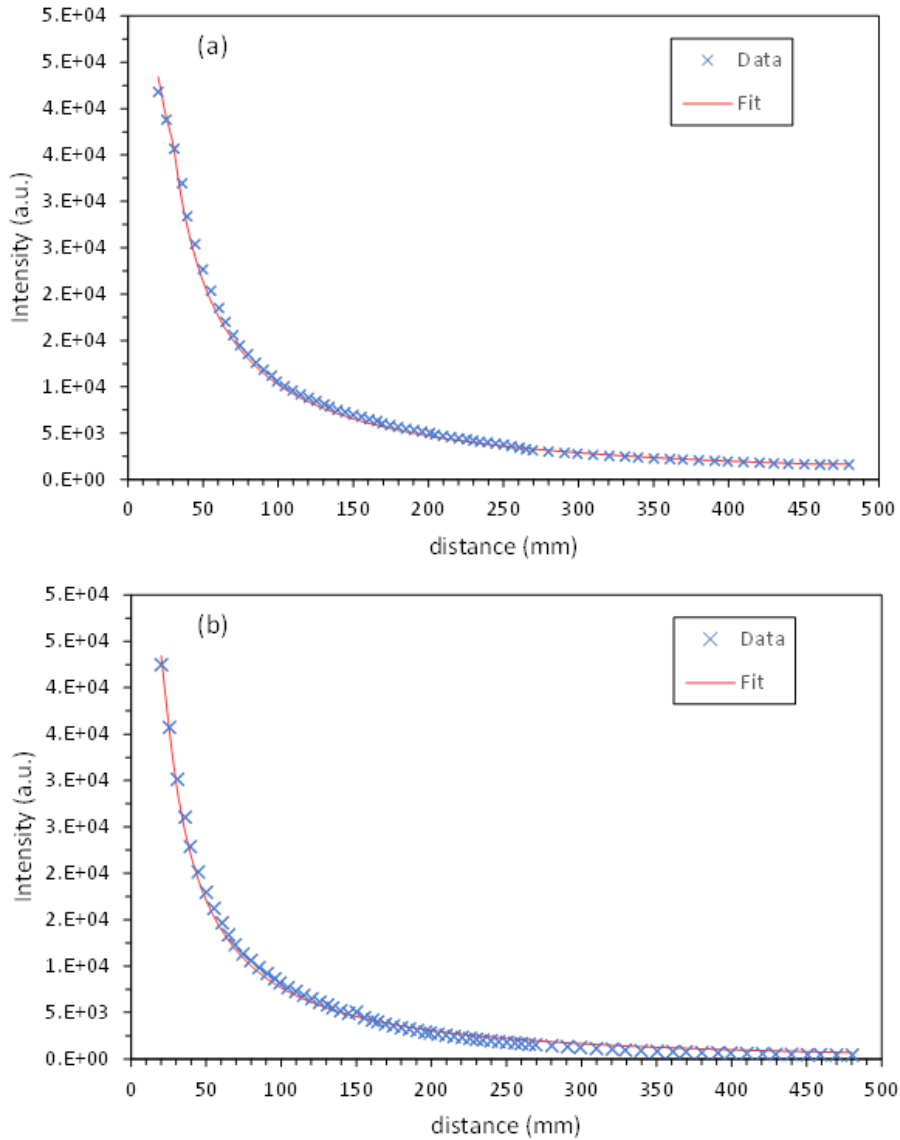
Figure 3.5 Measured intensity at 650 nm as function of the distance between the laser and the optic fiber for a dye concentration of (a) 300 ppm and (b) 160 ppm.

This step was made to obtain an absorption coefficient $\alpha_i(\lambda)$ and an initial intensity $I_{0i}(\lambda)$ for each wavelength that were employed as initial values for the Matlab function *"lsqcurvefit"*. It is a nonlinear least-squares solver, which is used to find the coefficients x that solve the problem $\min_{x} ||F(x, x_{data}) - y_{data}||_2^2 = \min_{x} \Sigma_i (F(x, x_{data(i)}) - y_{data(i)})^2$, where for the purpose of this analysis $F(x, x_{data})$ corresponds to the product between Equation (3.2) and Equation (3.3), in which $\alpha_i(\lambda)$ and $I_{0i}(\lambda)$ served as initial values for α

and I_0, respectively. x_{data} corresponds to the various distances d, and y_{data} to the intensities measured at those distances. The difference between the initial coefficients and the ones obtained thanks to the Matlab solver can be appreciated in Figure 3.5 where are shown the same plots of Figure 3.4, but with $\alpha(\lambda)$ and $I_0(\lambda)$ computed by using the *lsqcurvefit* function.

Considering the good agreement between the measurements and the simulations, the obtained $\alpha(\lambda)$ were employed to estimate the diffusion length of these LSC panels. For the purpose of this work this length was defined as "half power length", namely the distance that light should travel to halve its intensity. Figure 3.6 displays the absorption coefficients as a function of the wavelength for both dye concentrations and the relative half power lengths. The wavelengths below 600 nm were neglected since data corresponding to the fluorescent spectrum were analyzed, and these wavelengths are completely absorbed before reaching the optic fiber.
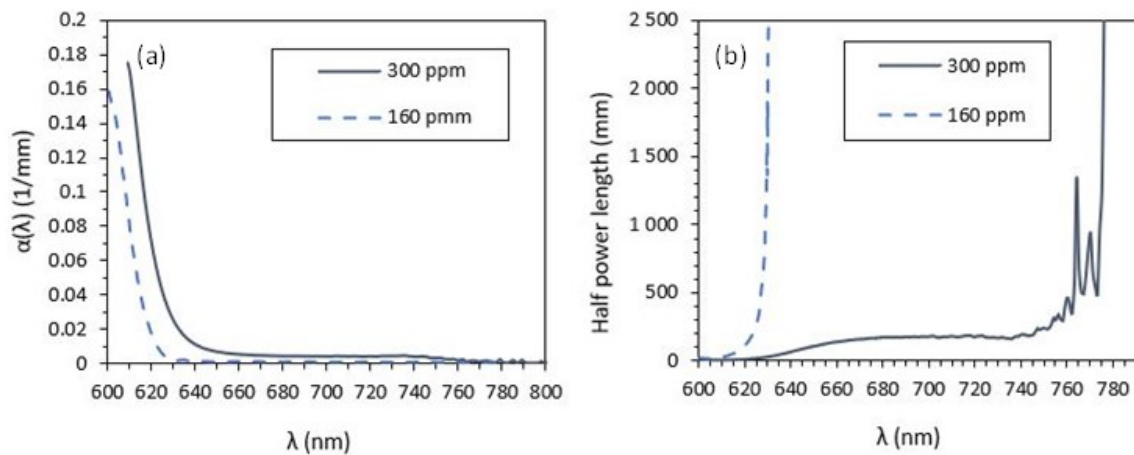
Figure 3.6 Absorption coefficient, (a), and half power length, (b), as a function of wavelength, doped with 300 ppm (continuous blue) and 160 ppm of dye (dashed light-bule).

By observing the results presented in Figure 3.6(b) it is clear that the LSC doped with the lower concentration (160 ppm) turned to be more suitable for this type of application. Indeed, the presented plot underlines that the slab with a 300 ppm dye concentration led to a higher absorption coefficient and to a lower diffusion length (if the same wavelengths are compared). This can be explained by the partial overlap between the spectra presented in Figure 3.1, in fact a decrease of the dye concentration corresponded a reduction of the self-absorption phenomena, and thus an increase of the diffusion length.

3.1.2 LSC electrical performance

In light of the abovementioned results, the LSC implemented in the VF was realized by doping a 1 m x 0.5 m x 0.005 m PMMA slab with 160 ppm of Lumogen® F Red 305. The proper LSC panel was then assembled by mounting along each of its longer edges four PV receivers, for a total of eight pieces. To ensure a good optical matching between the slab and the receivers they were coupled by using an optical UV glue with a refraction index of 1.506 [111]. The receivers mounted on the same edge were connected in parallel because of a limitation of the data acquisition system (Keithley 2400 SourceMeter), and the two PV branches were in turn connected in parallel. In Figure 3.7 a picture of one PV receiver is presented, realized by soldering to a printed circuit board with a SMT technique ten back contact SunPower™ Maxeon C50 solar cells [112]. The circuit board was 0.246 m long and 0.012 m large, and to adapt the PV cells to these dimensions they were cut into rectangles with an area of 0.024 x 0.008 m^2, thanks to a mechanical precision dicing machine.
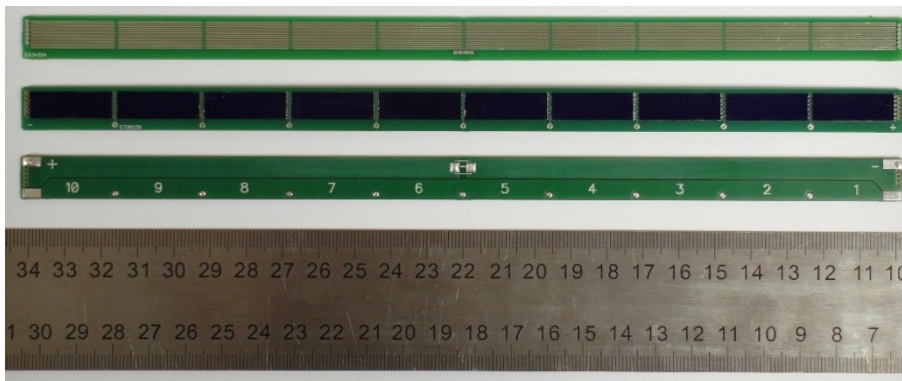
Figure 3.7 Picture of one PV receiver coupled with the LSC slab.

Following the results presented by Bernardoni et al [68] the shorter edges were covered with a high efficiency dielectric mirror film [113], as its application increased the panel performances with respect to a configuration with receivers along all sides. The authors have proved that this increase is much more evident when the device is partially shaded, and that this solution not only increased the panel efficiency but also decreased their costs, thus it is highly functional to limit the main drawback of LSC panels: their high price-per-watt ratio. Figure 3.8 exhibits a picture of the LSC panel in which the coupling between the PV receivers and the reflective layer is shown.
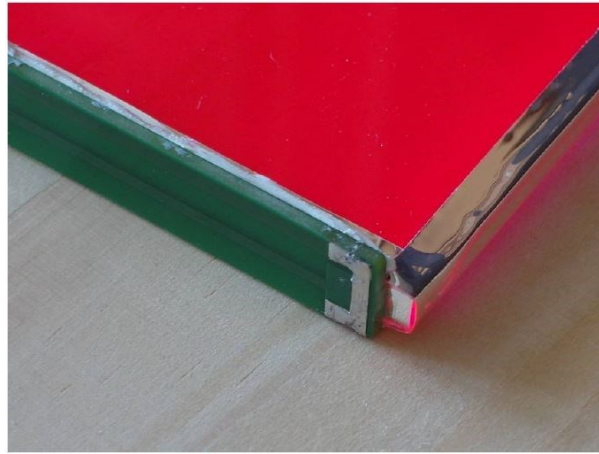
Figure 3.8 LSC panel detail showing the edge of the LSC slab fitted with the PV receivers on the longer sides and the reflective film on the shorter ones.

As can be seen from Figure 3.8 the reflective film was added also next to the PV receivers, this precaution was taken to reduce the possible efficiency decrease due to light reflection at the interface between slab and cells. In Figure 3.9 the results about the LSC panel electrical performance are reported. Figure 3.9 (a) displays the characteristic I-V and P-V curves of the module, registered at noon on May 04, 2021, under a Global Normal Irradiance (GNI) of 480 W/m^2. Figure 3.9 (b) shows the power produced by the LSC between the 04th and 9th May 2021. The measured power conversion efficiency was 0.5% that considering the slab dimensions and the employed PV cell is a value perfectly aligned with the ones found in literature [75].
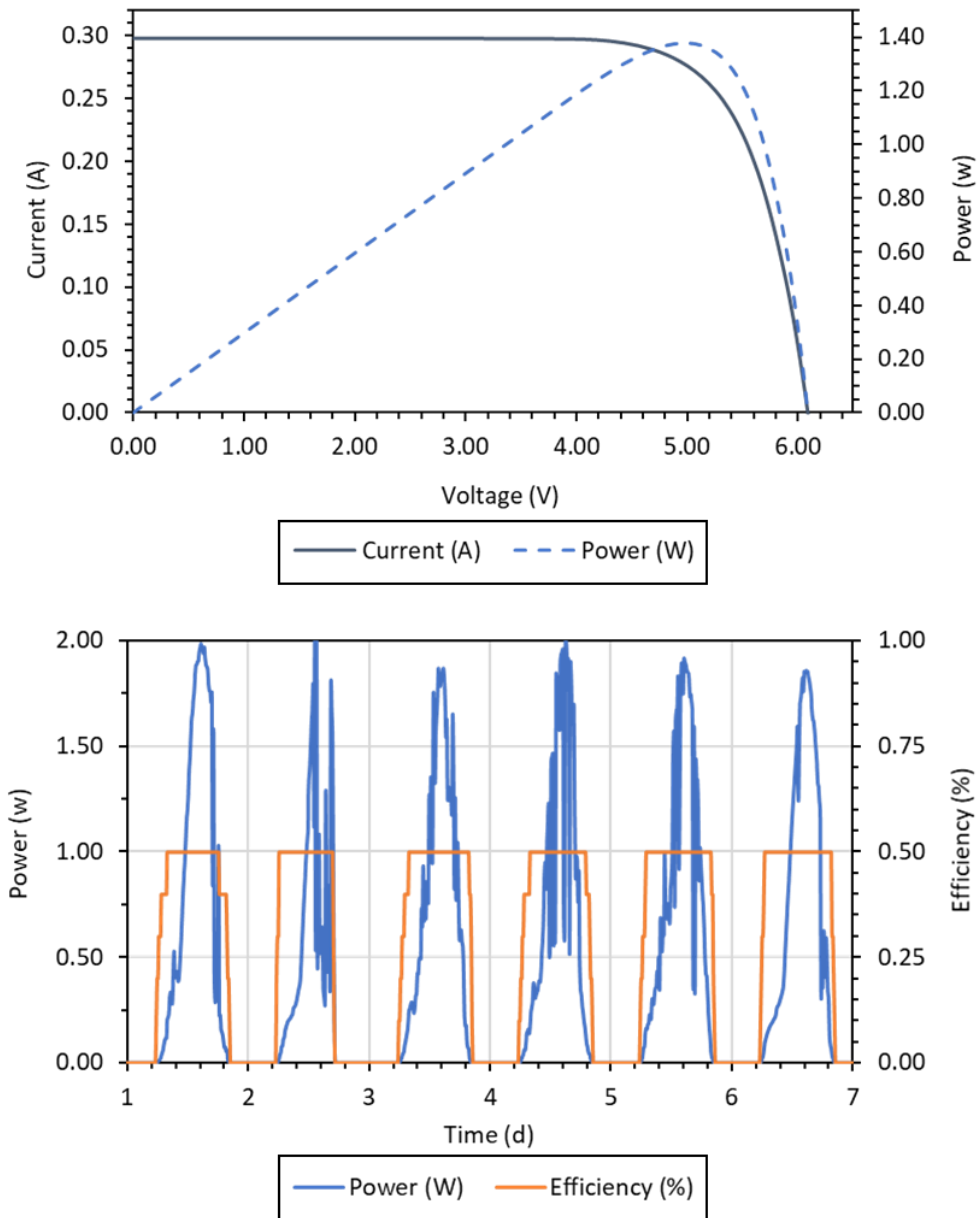
Figure 3.9 (a) Characteristic I-V and P-V curves of the LSC panel measured on the 04th May 2021 at noon, under a GNI of 480W/m². (b) Efficiency and power produced by the module between the 04th and 9th May 2021.

3.2 Mockup realization

The façade described in this work was developed with the intention to create a Narrow Façade that could be installed onto existing buildings to increase their thermal efficiency minimizing the retrofit footprint. The possibility to create a very narrow cavity was given by the high transparency of the LSC panels that ensures an increase in the solar radiation reaching the façade internal skin, if compared with traditional solar panels. This evidence combined with the work of Balocco [28] and Dragićević and Lambic [114] led to the realization of a VF having a ventilation chamber of 9 cm, with an LSC panel as external skin, and an aluminum plate as internal one. The choice of a reflective plate as internal skin was made to avoid overheating in summer and due to aluminum ease of manufacturing, in fact the LSC high transparency increased the importance of the back panel optical and aesthetical properties. The implementation of easily manufacturing materials as aluminum could open the possibility to create a back panel that increases the façade aesthetic appealing and optimizes the solar radiation harvesting, according to the climate zone and urban environment in which the system might be inserted. In order to calibrate and validate the developed models with experimental data, once the VF main parameters were defined, a mockup was built up in the Ferrara University campus. It was realized by stacking five different layers, four of which (the LSC and aluminum panel, the air cavity, and the insulating layer) represented the proper VF, whereas the last one (bricks) were added to increase the system thermal inertia and to resemble a wall behind the VF. To ensure that the heat flux was perpendicular to the layers and unidirectional the insulating layer and the bricks were inserted into a wooden framework, which was covered with insulating material. The wooden framework was made with two edges that were used as mounting points for the LSC and as boundaries of the air channel. The insulating material was also exploited to change the cavity configuration, switching from a close to an open channel VF, whose schematic representation is shown in Figure 3.10.

Position of the NTC temperature sensors:
- layer 1: on the back of the brick layer
- layer 2: between the insulation and the brick layer
- layer 3: between the two insulation panels
- layer 4: on top of the aluminum plate
- layer 5: on the back of the LSC panel

Layer 1

Layer 2

Layer 3

Layer 4

Layer 5

left
center
right

1 m

0.5 m

LSC panel, 0.005 m
Air channel, 0.09 m
Aluminum plate, 0.003 m
XPS insulation, 0.03+0.025 m
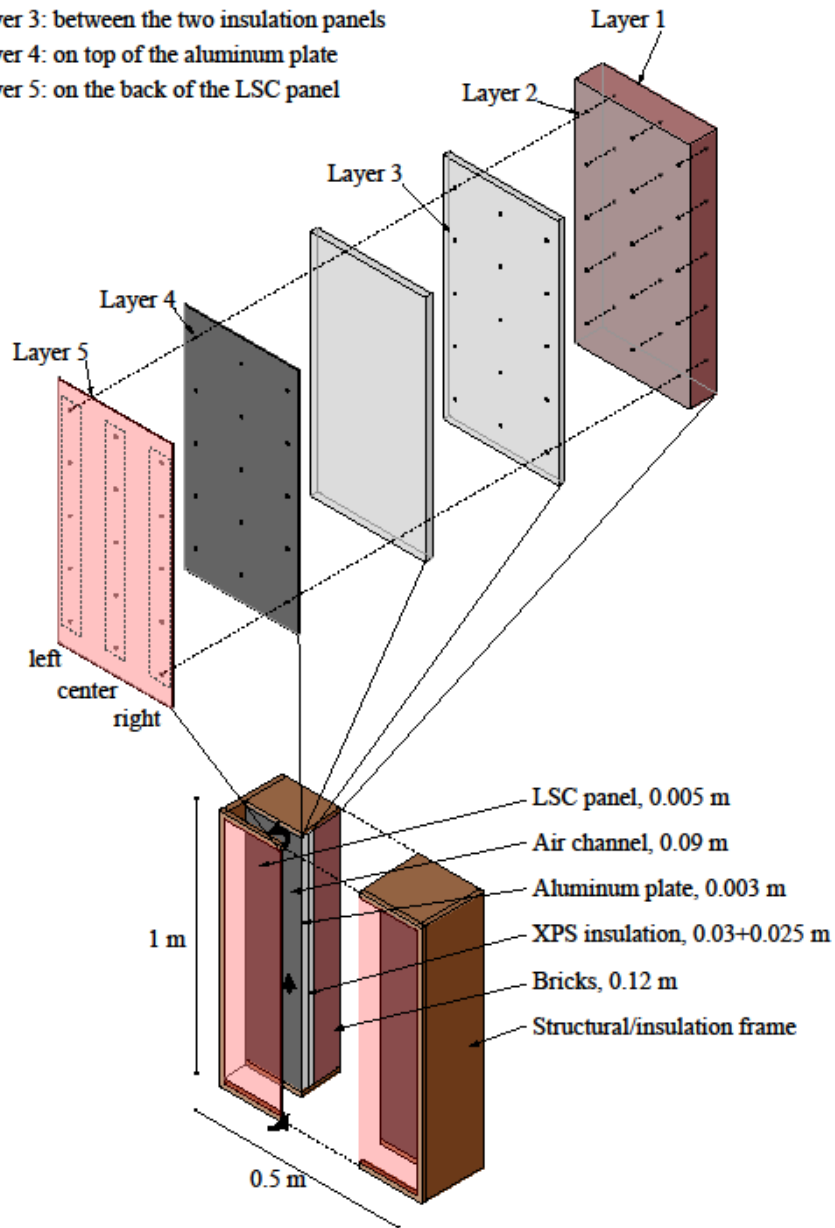Bricks, 0.12 m
Structural/insulation frame

Figure 3.10 Axonometric view of the mockup installed in Ferrara university campus, where in the top part the position of the installed temperature sensors (black dots) and their subdivision in Layers (1-5) and Sections (left-central-right) is highlighted.

The temperature of the system was monitored by installing several temperature sensors between the different layers. As thermal sensors Negative Temperature Coefficient (NTC) thermistors were chosen, since they ensured an excellent long-term stability and a high sensitivity over the temperature range in which the measurements were performed. They are sensors whose resistance decreases as temperature raises following a particular case of the Steinhart–Hart equation. Therefore, the relation between temperature and resistance can be expressed as:

$$(3.4) \quad R = R_0 \cdot e^{B\left(\frac{1}{T}-\frac{1}{T_0}\right)}$$

where B depends on the device characteristics, and R_0 is the resistance at temperature T_0 (298 K). The NTC sensors used in this data acquisition campaign were manufactured by Vishay BC component, and their B and R_0 values were equal to 3435 K and 10 KΩ [115], respectively.

Overall, seventy-five NTC sensors organized in a 5x5x3 matrix were installed. This arrangement allowed to organize the sensors according to two sub-divisions. The first one was represented by the splitting of the 5x5x3 matrix in three 5x5 matrices that crossed all five the material layers, generating three different identical sections of the mockup. The second division consisted in the splitting of the initial matrix in five 5x3 matrices involving just one material layer. In Figure 3.10 the mockup schematic with the position of the temperature sensors is depicted. The Layer 1 corresponded to temperature measured behind the bricks, the Layer 2 to the one between the insulation material and the wall, and Layer 3 to the temperature measured within the insulation layer. The Layer 4 and Layer 5 referred to sensors installed at the boundaries of the ventilation channel (the façade skins), in particular to the temperatures of the aluminum and the LSC panel, respectively. The sensors of the first row were placed at 0.085 m from the mockup base and each row was spaced by 0.20 m, Figure 3.11 shows the mockup with the disposition of three thermistor layers.
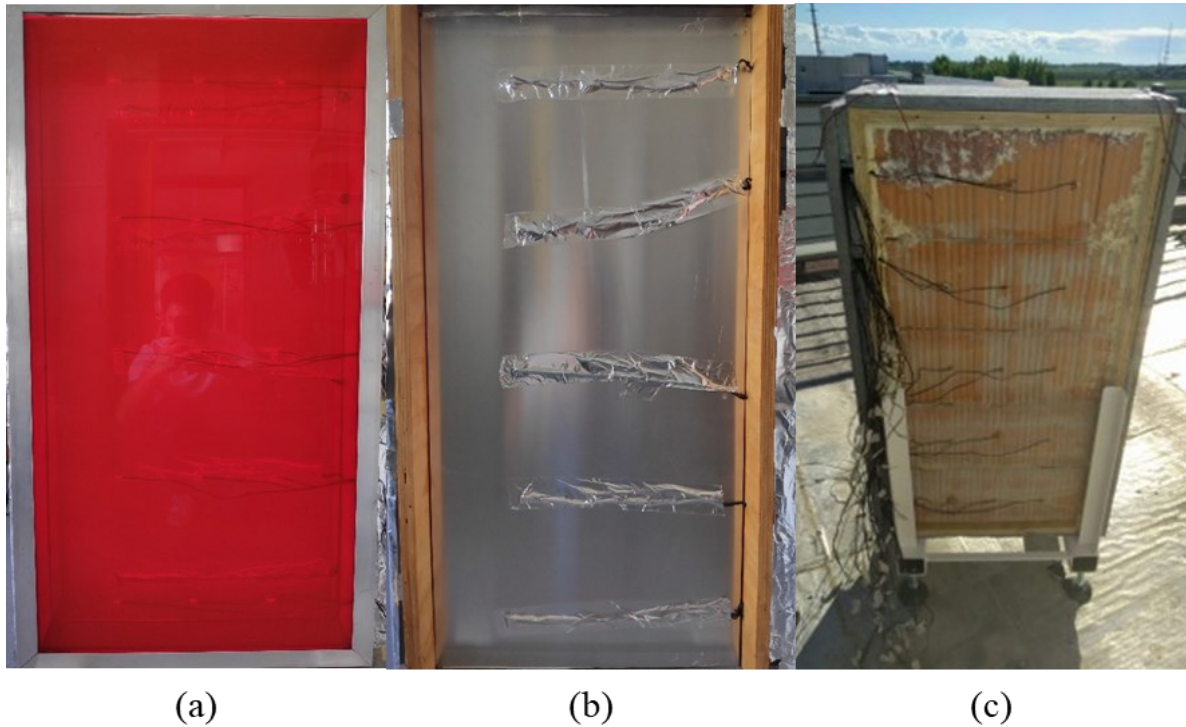
Figure 3.11.Pictures of Layer 5 (a), Layer 4 (b), and Layer 1 (c) of the mockup, whose back was further insulated during the data acquisition campaigns.

This sensors layout allowed the verification of the results presented by Pasut and De Clari [116]. They discussed the relevant elements in the simulation of a naturally VF using a CFD model, concluding that for these systems the velocity field is almost bidirectional, hence they can be simulated with 2D models and 3D ones are not needed. In Table 3.1 the temperatures measured between the 13th and the 18th of June 2021 by the sensors of the three sections for Layer 4 (aluminum) and Layer 5 (LSC) are presented. Table 3.2 reports the same measurements acquired in the period from the 07th to the 15th of September 2021. The two acquisition campaigns correspond to different cavity configurations, in fact in June the channel was closed whereas for the data collected in September it was naturally ventilated. The detected temperatures corroborate the results obtained by Pasut and De Clari so the simulation model was developed with a 2D geometry, choosing as data source for the calibration and validation procedure the central section. This choice was driven by the condition under which the experimental data were acquired, in fact they were collected by exposing the mockup to outdoor ambient conditions, and despite of the uniformity between the measured temperature, it was reasonable to suppose that the sensors placed along the central section were the ones less affected by abrupt changes of environmental conditions.

Table 3.1 Temperatures of LSC and Aluminum panel measured at different hours the 15th of June 2021 in the closed façade configuration.

daytime	T_{LSC} (°C)			T_{Back} (°C)		
	Left	Central	Right	Left	Central	Right
00:00	21.9	21.7	21.8	25.4	25.4	25.4
06:00	24.7	24.5	24.6	25.4	25.5	25.5
12:00	56.6	56.2	55.7	61.1	61.1	61.1
18:00	28.4	28.0	28.2	33.2	33.2	33.3

Table 3.2 Temperatures of LSC and Aluminum panel measured at different hours the 11th of September 2021 in the open façade configuration.

daytime	T_{LSC} (°C)			T_{Back} (°C)		
	Left	Central	Right	Left	Central	Right
00:00	17.3	17.0	17.1	20.3	20.3	20.3
06:00	17.0	16.8	16.9	18.1	18.2	18.2
12:00	48.7	48.9	47.1	43.7	43.5	43.1
18:00	23.4	23.1	23.3	26.1	26.1	26.1

In particular, the modeled data were primarily compared with the ones given by the central sensor of each layer. The choice of these sensors as primarily validation sources was due to the same reasons that led to the selection of the central section as validation section. The error related to the measured resistances δ_R was equal to the 1% [115], of the measured values and the errors related to temperatures were obtained by applying Equation (3.4) to δ_R.

3.2.1 Data acquisition system

The data were acquired by using the Multi_IO system, which is a modular system of electronic boards designed within the Photovoltaic Laboratory of the University of Ferrara. This system was developed to handle digital and analog input and output given by environmental sensors, and it was composed by a Main board with six power digital outputs (24V/4A) and as many basic (10bit ADC) inputs that could acquire both analog and digital signals within the range 0 V and 24 V. In order to collect the data of all the sensors the system was then expanded by coupling the Main board with four external add-on boards. The boards were all connected with a daisy-chain topology thanks to appropriate expansion connectors, which transported both power and communication through an I2C bus. A block diagram summarizing the components of the acquisition system is presented in Figure 3.12.
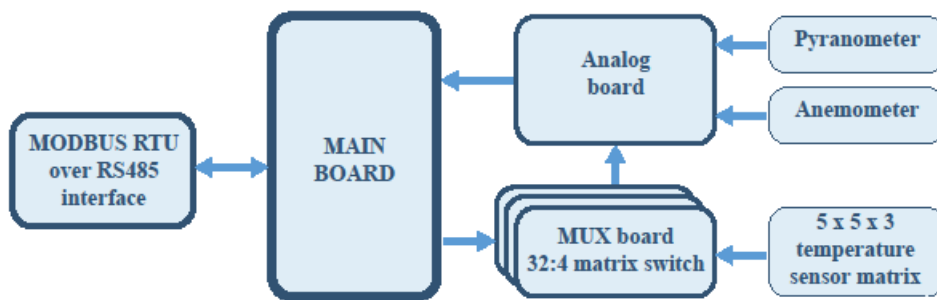

Figure 3.12 Block diagram depicting the components and the logical connection of the data acquisition system.

The Multi_IO system physical connection occurred through an unshielded twisted pair (UTP) cable with RJ45 connectors similar to the ones used for Ethernet networks. In our case, data were transmitted using the serial RS485 physical layer and communication was managed thanks to a standard MODBUS RTU protocol, which has widely been used in industrial sensor networks. The cable allowed for both daisy chain and star topologies (using a specific HUB) and powered the board with currents up to 2 A, without the necessity of an external power supply. The first addon board was an analog expansion board called Multi_IO_Analog, and its function was to digitalize the analog signals from the sensors network. The signal digitalization was carried out by high resolution and low noise 16-bit Sigma-Delta differential Analog to Digital Converters (ADCs), placed at the input of the Multi_IO_Analog board. The pyranometer (LP PYRA 03, manufactured by Delta OHM) and the anemometer (DW 6410, made by Davis Instruments) were connected directly to this board, whereas the acquisition of the signals generated by the NTC sensors

were multiplexed by three more expansions boards, called Multi_IO_MUX. Each of them was dedicated to one of the three 5x5 section matrixes that crossed all the façade layers, and the thermistors of each section were identified by a progressive index between 1 and 25. A Multi_IO_MUX board hosted quadruple 8-to-1 analog bidirectional matrix switches, arranged in a 32-to-1 configuration (connecting together the switch commons), this allowed to independently connect each NTCs to an input of the analog board.
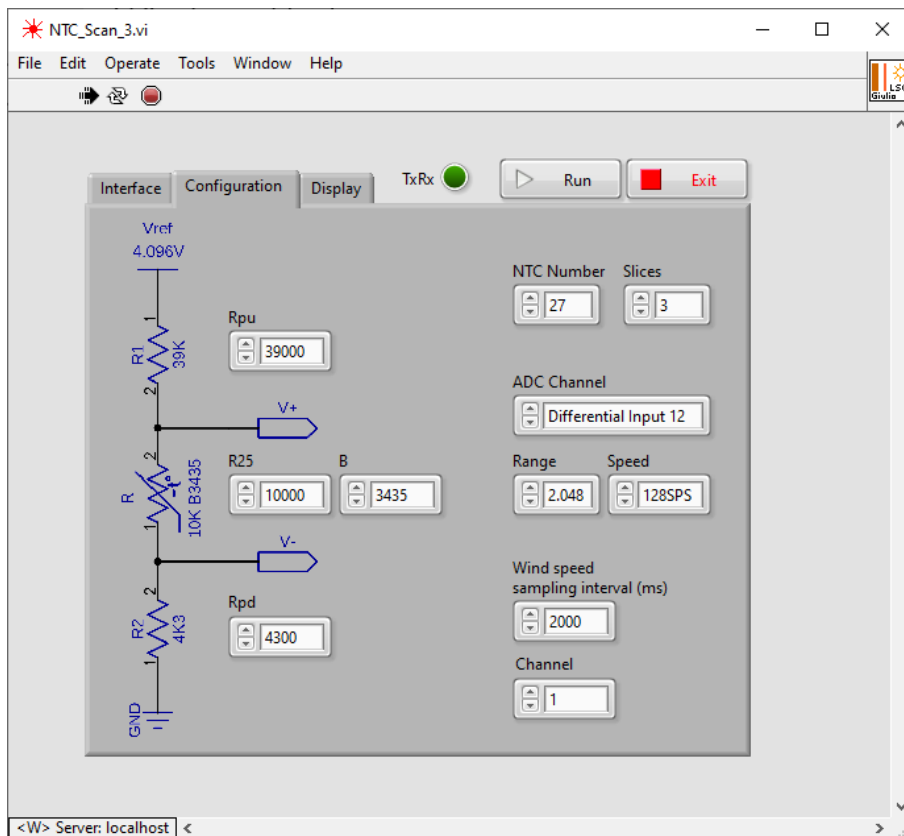
Figure 3.13 Screenshot of the Configuration Panel of the data acquisition software developed with LabView.

This configuration led to the voltage divider depicted in Figure 3.13, where the variable resistor labeled by R corresponded to NTC thermistor, and R1 and R2 to the pull-up and pull-down resistors respectively. The actual physical quantity measured by the data acquisition system was the voltage difference (V+−V-) across the NTC thermistor R. The increment/decrement parameter named *Slice* identified the number of Multi_IO_MUX boards connected to the system, whereas the one termed *NTC Number* set the maximum number of NTC sensors that were red by the software for each section. In this work it corresponded to twenty-six, the twenty-five embedded in the structure plus an external one for the ambient temperature. A voltage divider with three resistors was employed to ensure a proper bias of the analog signal, whereas the choice of the pull-up resistor, the pull-down one, and the voltage reference values was driven by the Multi_IO_Analog input range. In

fact, it ensured that the voltage difference between V+ and V- was within 0.18 V and 2.048 V, for a temperature range from -8 °C to 70 °C, with a constant ADC range. The constant ADC range had considerably simplified the acquisition software, ensuring that the error introduced by the acquisition electronics was much smaller than the NTC intrinsic one. Moreover, this configuration allowed the board to maintain a good sensitivity and signal to noise ratio. In Figure 3.14 the range of measurable temperature as a function of the of the potential difference across V+ and V- is depicted.

The data acquisition software was developed with a system-design platform called Laboratory Virtual Instrument Engineering Workbench (LabVIEW). It is a development environment for a visual programming language commonly used for data acquisition and instrument control. LabVIEW integrates the creation of user interfaces and programs-subroutines called Virtual Instruments (VIs), and the implementation of several VIs in combination with Equation (3.4) allowed the data acquisition, visualization, and storage, which was made in standard CSV format files. In Figure 3.15 is depicted the panel termed as *Display* of the data acquisition software, and it contained a table listing the temperature measured by the NTC sensors. In each row the value measured by the thermistors of the same section are reported, whereas the columns identified the different sections.
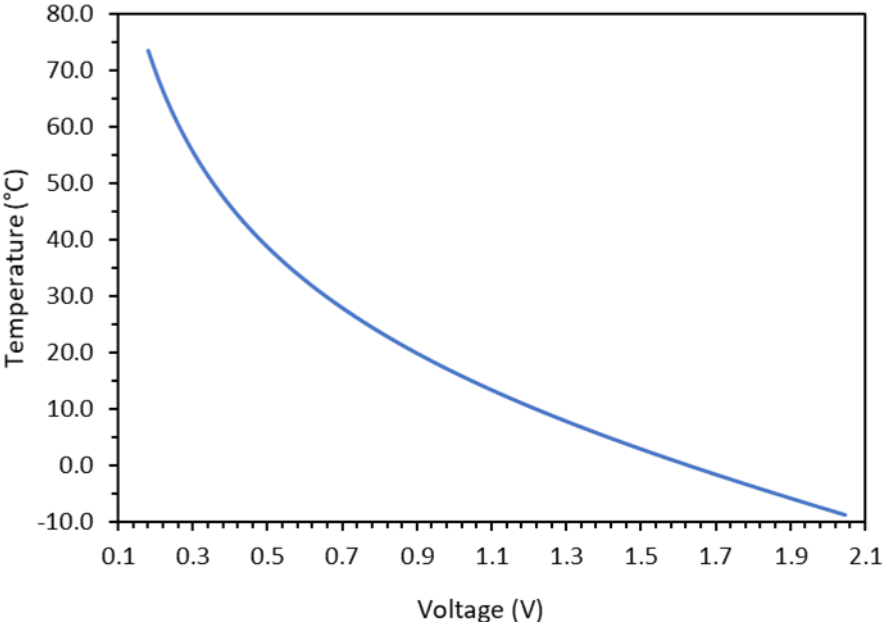
Figure 3.14 Measurable temperature range by the NTC sensors as a function the potential difference between their edges.

The system was developed to save several triplets formed by the values given by the thermistors of different sections labeled with the same index (1-25) as well as the wind speed, direction, and solar irradiance (GNI). On the right side of the *Display* panel, the voltage, resistance, and temperature values relative to the last measured triplet are displayed.
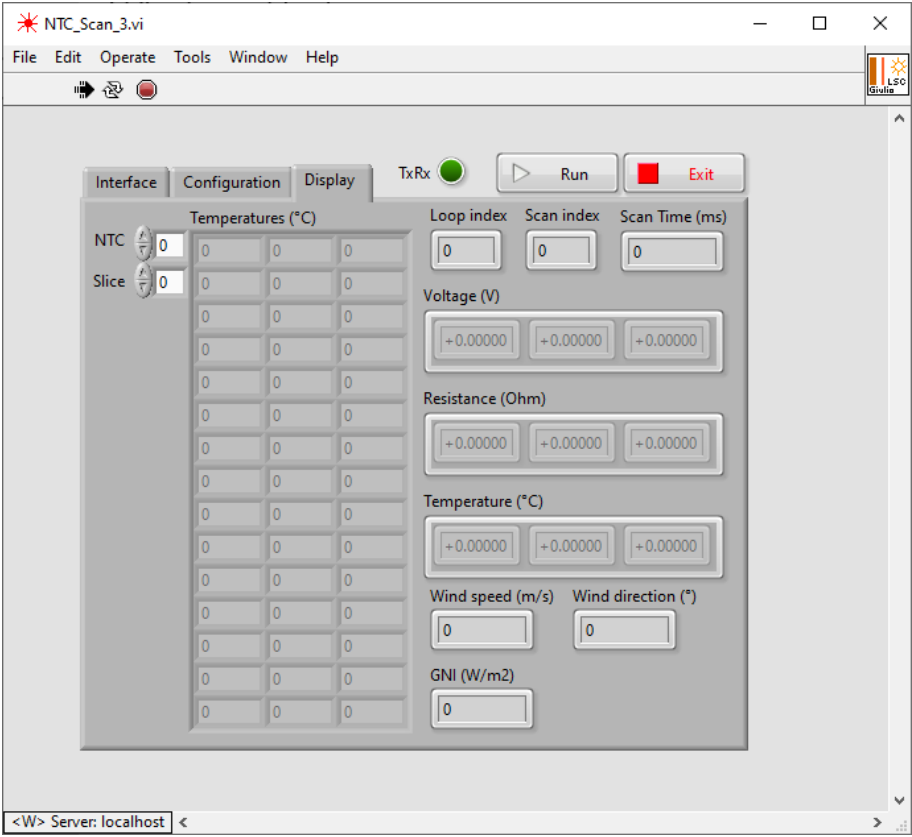
Figure 3.15 Screenshot of the Display Panel of the data acquisition software developed with LabView.

The presentation of the remaining parameters and panels was omitted as they have been inserted to ensure that the software could also be adapted to different data acquisition or expansion boards, and they were not essential for the interpretation of the work presented in this thesis.

3.3 CFD model

Following the considerations presented in *CHAPTER 2* the whole façade was modeled by using a computational fluid dynamic softer called COMSOL Multiphysics. In fact, the description of the air flow inside the cavity was intrinsically related to the efficiency of the VF. COMSOL is a multiphysics simulation software that solves partial differential equations thanks to FEM. and allowed to build a model through a tree structure called *Model Builder* composed by different nodes and branches. Figure 3.16 displays the main branches of the model builder, each branch was in turn subdivided in other branches with specific functions.

Figure 3.16 Scheme depicting the COMSOL main branches present in the software model builder.

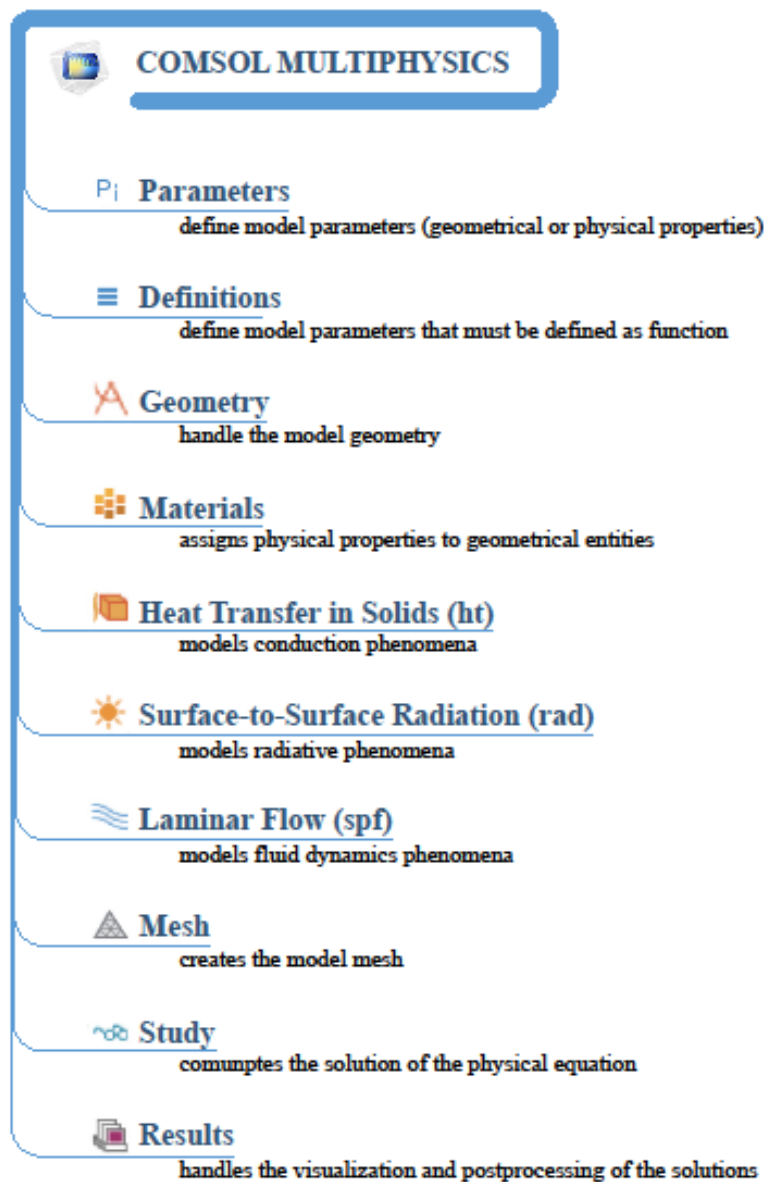The *Parameters* node was used to define global definitions like the parameters (constant quantities) and the inputs values of the model. The *Definitions* node allowed to monitor the desired physical quantities during the simulation procedure thanks to entities called *probes*. The same node was also used to import the measured data and compare them with the modeled ones, in fact, mathematical functions that returns measured data were defined and associated to fictitious probes, allowing to use data as irradiance, temperatures, and optical properties, as boundary conditions or to collate them with the model results.

The names of the next two nodes are quite self-explaining. The *Geometry* node was used to handle the model geometry and the *Material* one was necessary to confer to the geometrical entities their physical properties. The *Mesh* node was responsible for the creation of the model mesh, which was necessary for the computation of the results. Since creating a suitable mesh for a FEM simulation is crucial for getting accurate results, COMSOL allows to check the mesh quality in different ways, as the mesh plot or a presentation of the mesh statistics. For the models presented in this thesis the Mesh Plot was used as a qualitative analysis instrument, whereas the mesh statistics, and in particular the mesh element skewness, was used to quantitative evaluate the mesh quality. The skewness parameter corresponded to a value between 0 and 1 that evaluated the distortion of each mesh element with respect to the ideal element, at which COMSOL assigns a skewness equal to 1. The storage of the results was possible thanks to sub-node *Results*, which allowed also their postprocessing. The above-mentioned nodes are present in all COMSOL models, as they are not strictly related to physical phenomena and are functional to any simulation independently from the model nature. Instead, the three nodes *Heat transfer in solid and Fluids* (HT), *Laminar Flow* (SPF) and *Surface-to-surface Radiation* (RAD), also called *physics*, were implemented to model the heat transfer phenomena that occur inside a VF, so they were the core of the work presented in this thesis. The expressions in parentheses are the tags used by COMSOL to handle the different physics, and from now on they will be used as acronyms. The HT was used to model the heat exchange phenomena, and in particular the conduction ones, by solving the following equation:

$$(3.5) \quad \rho c_p \frac{\partial T}{\partial t} + \rho c_p \boldsymbol{u} \cdot \nabla T + \nabla \cdot (-k \nabla T) = q$$

where ρ is the material density, c_p its heat capacity at constant pressure, T is the absolute temperature, and $\boldsymbol{u}$ a velocity vector, which is considered different from zero only for the domains defined as Fluid. The term $-k \nabla T$ accounts for the conductive heat flux, and it is

defined as the product between the material thermal conductivity, k, and the temperature gradient, ∇T. Finally, q models the additional heat sources.

The SPF interface was used to handle the aspects related to fluid dynamics in the façade cavity, and since the air was simulated as a compressible fluid the relative equations were:

$$(3.6) \quad \rho \frac{\partial \boldsymbol{u}}{\partial t} + \rho(\boldsymbol{u} \cdot \nabla)\boldsymbol{u} = \nabla \cdot (-p\boldsymbol{I} + \boldsymbol{K}) + \boldsymbol{F} + \rho \boldsymbol{g}$$

$$(3.7) \quad \frac{\partial \rho}{\partial t} + \nabla \cdot (\rho \boldsymbol{u}) = 0$$

where ρ and $\boldsymbol{u}$ were the fluid density and velocity vector. The term $-p\boldsymbol{I} + \boldsymbol{K}$ represented the Cauchy stress tensor and accounted for pressure and viscous stress. $\rho \boldsymbol{g}$ was the term that simulated the gravity force, and $\boldsymbol{F}$ a vector that modeled additional volumetric forces.

The nature of the flow (laminar or turbulent) was checked by following the official COMSOL procedure presented by F. Schlegel, concerning the natural convection [117]. In this section is explained that for a natural convection problem the ratio between buoyancy and viscous forces acting on the air can be expressed thanks to the Grashof number, Gr. For a compressible fluid the Gr is defined as [118]:

$$(3.8) \quad Gr = \frac{g \Delta \rho L^3}{v^2 \rho}$$

where g is the gravity acceleration, and ρ the fluid density. L identifies the characteristic length, and since convection in a vertical cavity can be treated as an internal flow problem, the characteristic length was defined as the hydraulic diameter $D_h = 4A/P$, with A and P the cavity cross-sectional area and perimeter, respectively. A value below 10^8 indicates that the flow is laminar, whereas a value above 10^9 indicates that the flow is turbulent, with the range $10^8 < Gr < 10^9$ corresponding to a transition region. The assumptions made within this thesis led to a $Gr \approx 1.5 \cdot 10^6$, thus confirming the laminar flow hypothesis.

Lastly, the RAD node modeled the radiative phenomena between surfaces according to the following law:

$$(3.9) \quad q = F(G - J)$$

where q is the net radiative heat flux entering the surface, F the surface view factor, G the total radiation impinging on it, and J the surface radiosity, defined as the total radiation that exits from the surface. The terms contained in Equation (3.9) can be function of different

parameters like the methodology used to model the radiation, the type of surface, and the imposed boundary. Furthermore, it is important to underline that also the attribution of the material optical properties depends on the methodology used to model the radiation. However, COMSOL considers the domains implemented as *Solid* in HT physics as opaque, and the ones defined as *Fluid* as transparent, associating by a transmissivity equal to 0% to the former and 100% to the latter. All these aspects will be discussed more in detail in following sections after the definition of the parameters that influence them.

Each node, HT, SPF, and RAD, considers its physical phenomenon separately and their interaction was taken into consideration through the *Multiphysics* node. In particular the sub-sub-node *Heat Transfer with Surface-to-Surface Radiation* (HTRAD), couples the conduction with the radiation phenomena thus accounting for the heat exchange due to radiation. The convective heat exchanges were instead handled by the sub-sub-node called *Non isothermal flow* (NITF), which coupled conduction and fluid dynamics.

Depending on the physics implemented in the model, COMSOL requires some parameters, resembling the physical properties of the materials inserted in the *Material* node. For the Heat transfer in Solids and Fluids the thermal conductivity, λ, the density ρ, and the heat capacity at constant pressure C_p are mandatory. For the Laminar Flow module, the dynamic viscosity, μ, must be defined, and moreover it demands that the objects inserted in the SPF were also defined as fluids in the Heat transfer in solid and Fluids physics.

The properties needed by these nodes are bulk properties, as they model physical phenomena which involve both the material surface and bulk, whereas the ones demanded by Surface-to-surface Radiation are surface properties. Being RAD a node that models phenomena involving just surfaces, the surface emissivity, ε, the transmissivity, τ, and the reflectivity ρ, are required. Once these parameters are defined, to solve the simulation is sufficient to define the model initial conditions. In fact, if no further instructions are implemented, the mesh is automatically created by COMSOL according to the physics involved in the model. In Figure 3.17 a detailed view of the model Definitions, Materials and Geometry nodes is presented.
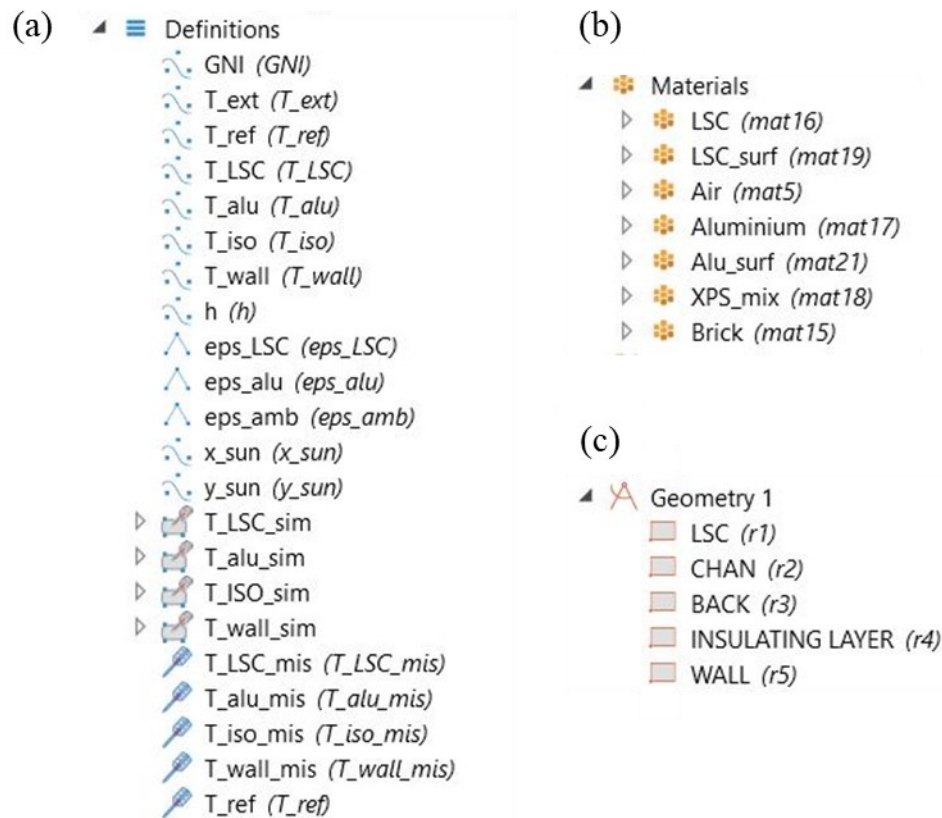
Figure 3.17 Closed Facade model (a) component, (b) materials, and (c) geometry.

In the Definition section the measured data as well as some of the material properties were collected. The GNI function was an interpolation function that represented the global normal irradiation with respect to the façade, which was measured by using a pyranometer placed next to it. The functions characterized by the label *T_* were again interpolation functions, and they corresponded to the measured temperatures, and starting from top to bottom, they referred to: the external (ambient) temperature; the temperature measured by the sensors of the Layer 1, T_ref; the temperature on the LSC internal surface, measured by the sensors of Layer 5; the temperature on the back panel (aluminum) surface, measured by the sensors of the Layer 4; the temperature within the insulating layer, measured by the sensors of Layer 3; and the temperature of the surface between the insulating material and the wall, measured by sensors of Layer 2.

The objects defined as *T_xxx_sim* or *T_xxx_mis* referred to probes used to compare the measured and simulated temperatures. The ones labeled *T_xxx_sim* were point-like probes placed in correspondence to the central probe of each Layer (see Figure 3.10), and they saved the simulated temperatures at specific points. The others were instead global probes used to import the temperature measured from the real sensors, the same temperatures were provided as input parameters for the functions named as *T_xxx*.

Figure 3.17 (c) shows the geometry implemented to model the real mockup, each layer was defined as a rectangular domain 1 m high and with a variable width. The width of each domain was ascribed according to the thickness of the real elements (see Figure 3.10). In Figure 3.17 (b) the materials attributed to each layer are listed. The labels *xxx_surf* identified boundary materials that were implemented to confer the properties *eps_LSC* and *eps_alu* demanded by RAD to the LSC and the aluminum slab. The remaining ones are instead domain materials, necessary to confer the properties required by HT and SPF. Their list is presented in Table 3.3, except for the air properties, because the COMSOL default ones were used.

Table 3.3 List of the thermal properties attributed to each layer

	LSC	Back Panel	XPS_mix	Wall
λ (W/(m·K))	0.19	237	0.037	0.24
ρ (kg/m^3)	1180	2700	1300	840
C_p (J/(kg·K))	1466	900	80	500

The properties listed in Table 3.3 were selected following the same principle of the optical ones, they were defined starting from literature values [119–124], and then modified within literature ranges. For example, the property of XPS_mix has been averaged to consider that the insulation layer is formed by a combination XPS panels and polyurethane foam, which was added to ensure the adhesion between the bricks and the XPS panel.

The function h corresponded to the convective heat transfer coefficient inserted in the HT interface to model the convective heat exchange between the ambient and the LSC external surface, and it was computed starting from the wind velocity, v_{wind}, according to [125].

$$(3.10) \quad h = 5.7 + 3.8 \cdot v_{wind}.$$

The functions labeled by *eps_* were piecewise functions implemented to model the emissivity of the materials. They referred to the LSC (*eps_LSC*), aluminum (*eps_alu*), and ambient emissivity (*eps_amb*). The first two were mandatory to simulate the mutual radiative heat exchange between these surfaces and to consider the radiative heat flux due to the solar radiation. The last one was instead inserted to give a better approximation of the cooling due to the long wave radiation exchange between the façade and the sky. In fact, the sky could be seen as a further heat sink for the building exterior surfaces, which generated a heat loss due to the emission of long wave radiation. The interaction between

the VF and the sky were simulated considering that the infrared radiation emitted by buildings could be split in two main categories: the one absorbed by the water vapor and other greenhouse gasses present in the atmosphere, and the one at which the atmosphere is almost transparent. In fact, the infrared radiation emitted in the wavelength of the so-called *atmospheric window* (8–13 μm) propagates to the outer side of the atmosphere. Normally, building simulation tools model these interactions by introducing two different temperatures, a fictitious temperature called T_{sky} and. the ambient temperature T_{amb}. The first is used to model the building-ambient heat exchange within the atmospheric window, whereas T_{amb} is used to simulate the building-atmospheric radiative heat exchange in the remaining wavelength ranges [126]. The importance for the correct estimation of building thermal performance is testified by the Albatayneh et al. work [127]. However, not being COMSOL a building simulation tool, it considers only one temperature T_{amb}, and the only way to better resemble the effects of atmospheric window on the VF was to define a modified ambient emissivity; as shown in the COMSOL example called *Radiative cooling* [128]. Table 3.4 contains the values attributed to *eps_amb* for each wavelength range.

Table 3.4 Ambient emissivity defined for the modeled wavelength ranges.

λ_{start} (μm)	λ_{end} (μm)	ε_{amb}
0	0.38	1
0.38	0.42	1
0.42	0.46	1
0.46	0.5	1
0.5	0.61	1
0.61	2.5	1
2.5	8	1
8	13	0.3
13	25	0.9

The definition of different wavelength ranges was possible thanks to the option *multiple spectral bands* in the RAD sub-node, however the definition of each wavelength range highly affects the computational resource needed for the simulation, since COMSOL had to solve a new set of radiative equations, like Equation (3.9), for each wavelength range. Given the number of wavelength ranges under consideration, the values of *eps_LSC* and *eps_alu* were attributed starting from a combination between experimental measurements

and literature evidence [129–133]; then they were slightly modified to better match the ones of the real system. Figure 3.18 displays the measured emissivity values, from 350 nm to 800 nm, for both the LSC panel and the aluminum plate. They were obtained by indirect measurements thanks to Equation (3.11):

$$(3.11) \quad \varepsilon + \tau + \rho = 1$$

where ε, is the object emissivity and absorptance, τ its transmittance, and ρ the total reflectance. For the LSC slab both the reflectance and transmittance were acquired, and since for the aluminum plate $\tau = 0$ only the specular reflectivity was measured
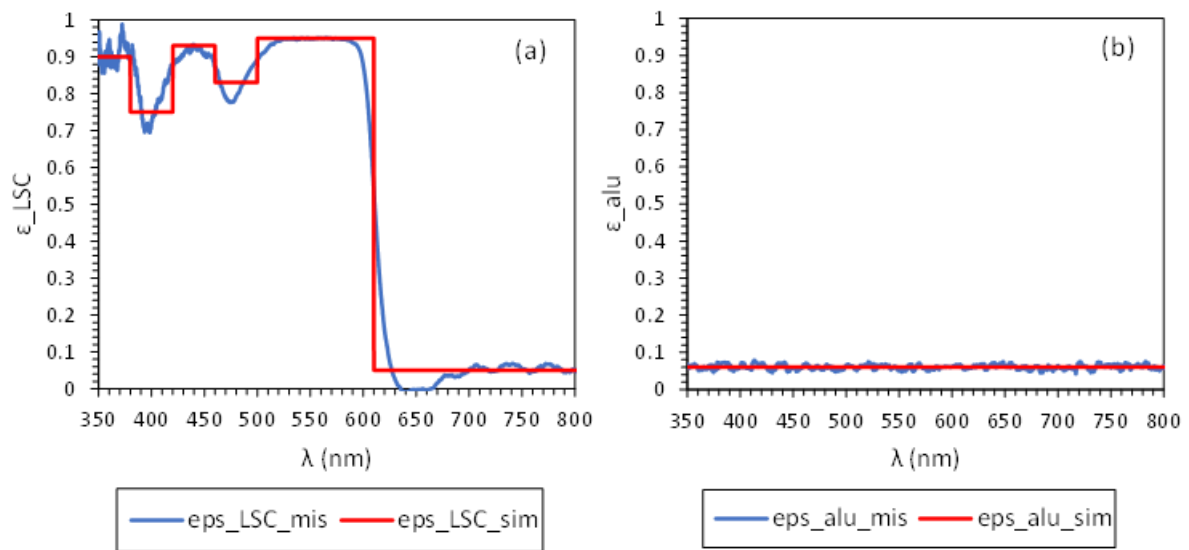

Figure 3.18 (a) LSC and (b) aluminum emissivity spectrum measured in the range 350-800 nm

In Table 3.5 and Table 3.6 the emissivity value attributed to the LSC slab, and the aluminum panel are reported.

Table 3.5 Emissivity attributed to each surface of the LSC panel.

λ_{start} (μm)	λ_{end} (μm)	ε_{LSC}
0	0.38	0.9
0.38	0.42	0.75
0.42	0.46	0.93
0.46	0.5	0.83
0.5	0.61	0.95
0.61	2.5	0.05
2.5	8	0.05
8	13	0.05
13	25	0.05

Table 3.6 Emissivity attributed to the aluminum slab surface.

λ_{start} (μm)	λ_{end} (μm)	ε_{alu}
0	0.38	0.06
0.38	0.42	0.06
0.42	0.46	0.06
0.46	0.5	0.06
0.5	0.61	0.06
0.61	2.5	0.07
2.5	8	0.05
8	13	0.01
13	25	0.01

3.3.1 Closed Façade model

This model was developed to match the closed façade configuration, for which the model components, geometry, and materials corresponded to the ones mentioned in the previous paragraph, and the experimental data were acquired in the period between 13 and 18 June 2021. Figure 3.19 shows the graphic of the COMSOL model, in which each element was separately highlighted thanks to a bluish shade. Figure 3.20, Figure 3.22, and Figure 3.23, are instead useful to understand which components were inserted in each physics, and how their model builder was structured.
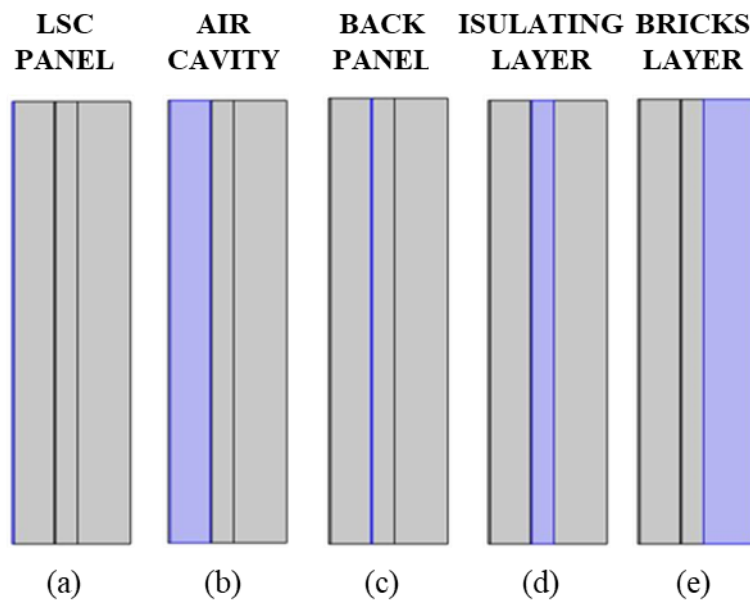

Figure 3.19 Graphic of the model geometry in which each element is separately highlighted, (a) LSC panel, (b) air channel, (c) aluminum back panel, (d), insulating layer, (e) wall.

Figure 3.20 highlights that all the domains were considered inside the HT interface, and they were divided in solid (LSC panel, aluminum plate, insulating layer, and wall), and fluid (the air inside the cavity). The nodes labeled *Initial Values_* were used to attribute the initial value to each layer, by using the temperature measured at the beginning of the data acquisition campaign. The *LSC heat flux* node was implemented to simulate the forced convective heat flux due to wind. It was imposed onto the external surface of the LSC panel, and it was modeled as:

$$(3.12) \quad q = h(T_{ext} - T)$$

where q represented the convective heat flux, T corresponded to the temperature of the LSC external surface, and T_{ext} the measured ambient temperature. The value of h was computed according to Equation (3.10).
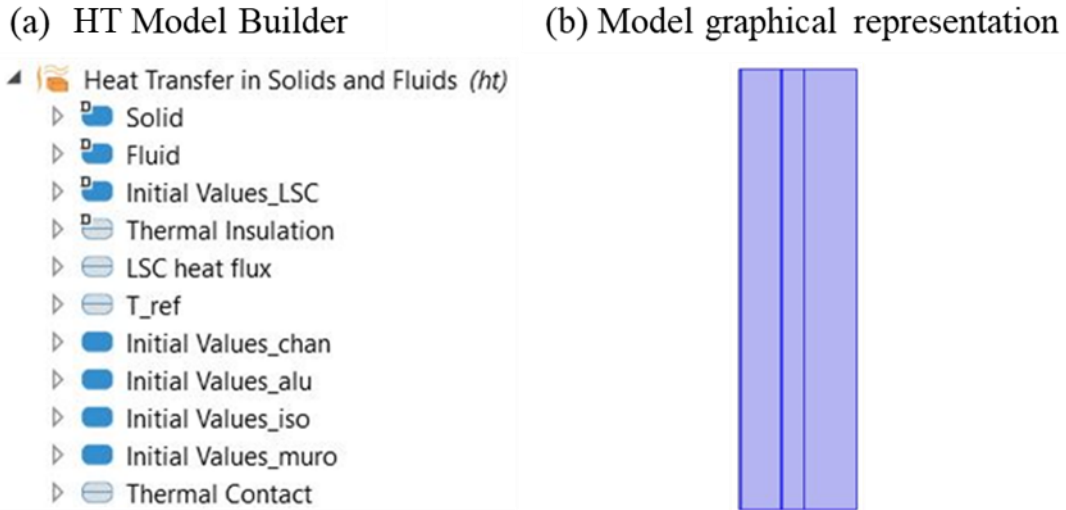

Figure 3.20 (a) Model builder list and (b) graphical representation of the component inserted in the HT node.

The sub-node T_ref was used to impose the temperature measured from the sensor of the Layer 1 onto the inner boundary of the wall as boundary condition. The Thermal Contact node was implemented to model a resistive layer between the aluminum panel and the insulating layer, which was inserted to consider the not ideal thermal coupling between the two layers. Considering the modeled materials, the operating conditions and the literature evidences [134,135], the layer equivalent thermal resistance was set equal to: $R_{eq} = 2 \ (Km^2)/W$.
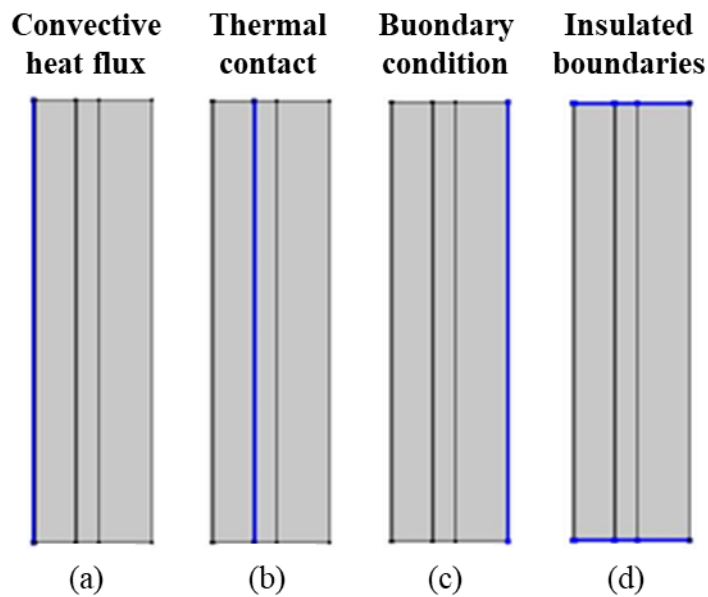

Figure 3.21 Components inserted in the HT node (a) convective heat flux, (b) thermal contact, (c) boundary condition, (d) insulated boundaries.

The wooden framework and the insulating coat were excluded from the simulations, but their presence allowed to model the remaining boundaries as thermally insulated. In Figure 3.21 the visual presentation of these functional nodes inserted in the HT physics is presented.
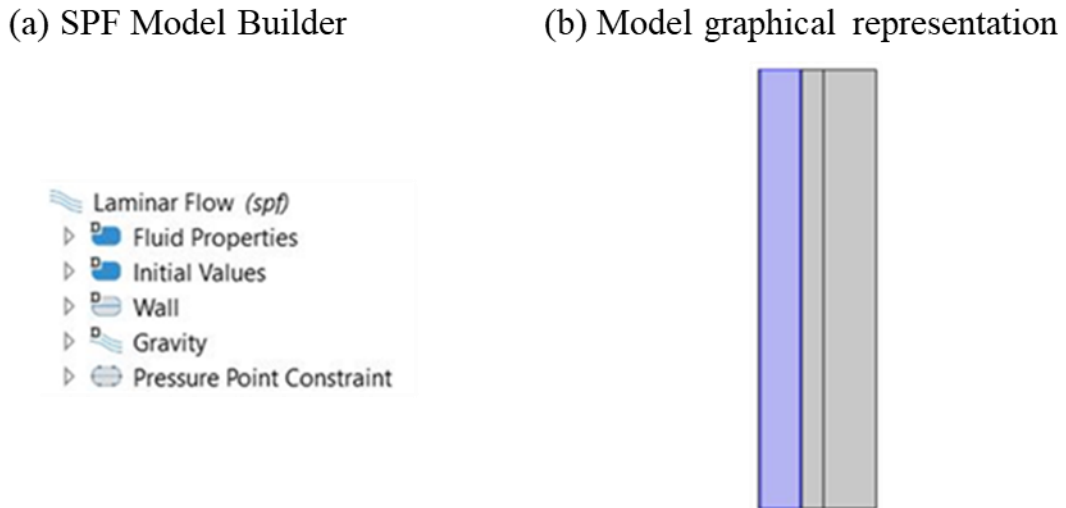
(a) SPF Model Builder   (b) Model graphical representation

≋ Laminar Flow *(spf)*
▷ ᴰ⬤ Fluid Properties
▷ ᴰ⬤ Initial Values
▷ ᴰ⬤ Wall
▷ ᴰ≋ Gravity
▷ ⬤ Pressure Point Constraint

Figure 3.22 (a) Model builder list and (b) graphical representation of the component inserted in the SPF node.

As mentioned above, Figure 3.22 shows that the only domain inserted SPF was the air cavity. The physics was introduced to consider the dependency of air density from the temperature, and the air inside the cavity was defined as a weakly compressible fluid; furthermore, the sub-node *Gravity* was inserted to simulate the effects due to the gravity acceleration. The channel boundaries were considered as walls under the *no-slip* condition, and, thanks to the homonym sub-node, a pressure point constrain was implemented with a value equal to the atmospheric pressure. This sub-node was added to define a pressure reference point inside the cavity and ensure the model convergence. The air temperature and density were computed in the HT physics, and they were provided to SPF by the NITF Multiphysics.

Figure 3.23 displays the surfaces inserted in the RAD interface, i.e., the aluminum external one and the LSC external and internal surfaces. They were modeled following the indications given by the COMSOL application *Greenhouse Effect* [136], according to which all the surfaces were defined as *diffusive surfaces*, hence they were subjected to the following equations:

$$(3.13) \quad J_i = \varepsilon_i \epsilon_b(T) FEP_i(T) + \rho_{d,i} G_i$$

74

$$(3.14) \quad \varepsilon_i + \rho_{d,i} = 1$$

$$(3.15) \quad q_{r,net,i} = \varepsilon_i(G_i - \epsilon_b(T)FEP_i(T))$$

Where, as in Equation (3.9) J_i is the surface radiosity, ε_i and $\rho_{d,i}$ the surface emissivity and diffuse reflectivity, $\epsilon_b(T)$ the blackbody radiation emission, and $q_{r,net,i}$ defines the total radiative heat flux entering the surface. G_i is the total radiation impinging on the surface and it can be better defined by Equation (3.16).

$$(3.16) \quad G_i = G_{m,i}(J_i) + F_{amb,i}\varepsilon_{amb,i}\epsilon_b(T_{amb})FEP_i(T_{amb}) + G_{ext,i}$$

where $G_{m,i}$ is the mutual radiation between different surfaces, $\varepsilon_{amb,i}$ is the ambient emissivity (see Table 3.4), and $G_{ext,i}$ is the external irradiation and corresponds to the measure GNI. $F_{amb,i}$ is the ambient view factor, which was considered equal to 1 for all the developed models. The subscript i refers to the considered wavelength range, and its presence is due to the choice of the multiple spectral bands option. The same goes for the $FEP_i(T)$ coefficient, which considers the weight of each wavelength range with respect the totality of the simulated ranges.
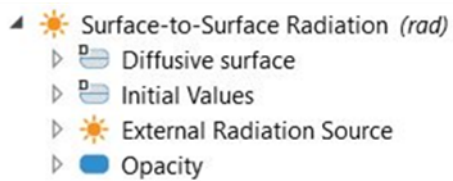
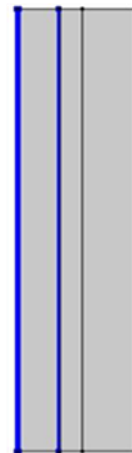(a) RAD Model Builder   (b) Model graphical representation

Figure 3.23 (a)Model builder list and (b) graphical representation of the component inserted in the RAD node

By comparing Equation (3.11) and Equation (3.14) it can be noticed that diffusive surfaces do not model surface transmittance, as by definition they are layers that absorb or reflect the impinging light. The modeling of the LSC transmittance properties was referred to the *Opacity* sub-node that allowed to define whether the domain absorbs or transmits

the impinging radiation for each wavelength range. According to Figure 3.18 (a), the LSC slab was defined opaque for the wavelengths shorter than 0.610 μm and transparent for the longer ones. The main drawback of this approximation was that this node defines the optical property of the medium by treating the transparency as a binary function. The domain became completely transparent or completely opaque collapsing the optical properties of the real LSC, which for the physical object are defined in the whole volume, on its main surface. However, as will be shown in Paragraph *3.3.3 Data comparison*, this approximation did not compromise the obtained results. Finally, the *External Radiation Source* was a sub-node defined as a point like source with an intensity equal to the GNI, positioned at an infinite distance from the simulated structure.
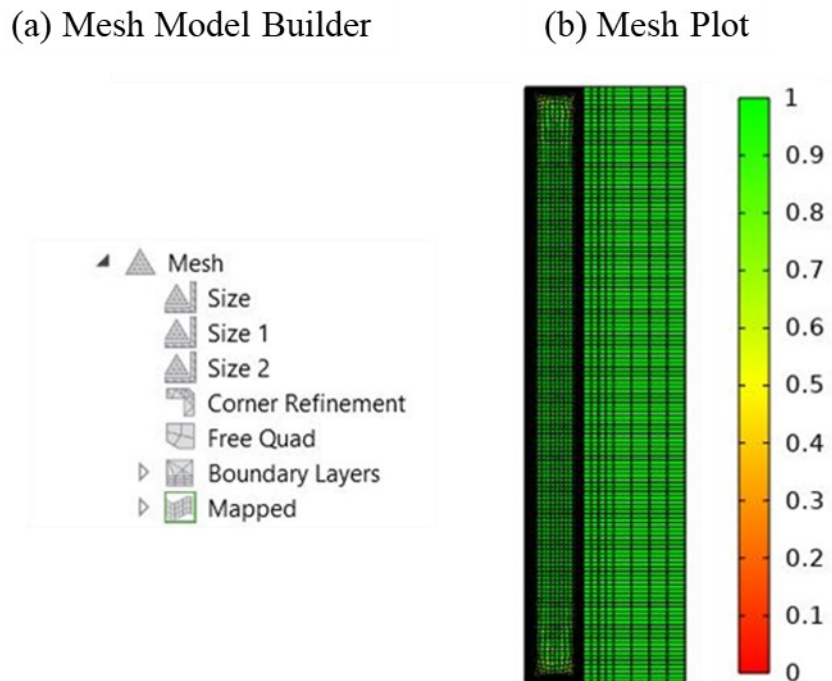

Figure 3.24 (a) Mesh model builder of the closed configuration model and (b) the relative mesh plot, reporting the skewness color map as quality parameter.

The model was meshed by combining different mash elements, as the necessity to simulate fluid dynamics phenomena required a particular mesh inside the façade channel. In particular, two bidimensional mapping structures were employed, and the channel was meshed thanks to the *Free Quad* node, whereas the remaining domains were meshed by using the *Mapped* node. The *Free Quad* node allowed to mesh the air cavity domain by creating unstructured quadrilateral elements and, considering that the air flow would have developed mainly along the system height, its elements were preferred to the triangular structure proposed by the *Free Triangular* node. Indeed, considering the symmetry of the system, the air velocity field can be considered almost monodirectional (along the height of

the cavity), thus the presence of triangular elements would have increased the simulation computational cost without improving the accuracy of the results. In this case the skewness parameter measured the distortion with respect to quadrilateral elements, where a value equal to 0 is associated to very distorted mesh elements and 1 to quadrilaterals.

The quality of the created mesh was further improved thanks to the addition of the *Corner Refinement* node and the *Boundary Layer* one. The former decreased the element size at sharp corners, whereas the latter is typically used to resolve the thin boundary layers along no-slip boundaries in fluid flow problems and was exploited to create a mesh with a denser element distribution in the direction normal to the flow. The remaining domains were meshed thanks to the *Mapped* node that created structured quadrilateral mesh elements controlled by the *Distribution* sub-node. This node allowed to define the number and size of the mesh elements along an edge, and for this specific application only the distribution along the domain width was defined. The distribution along their height was automatically handled by COMSOL thanks to the extrusion of the mesh pattern present in the air cavity. The Mesh model builder and Mesh Plot that testifies the good quality of the created mesh is reported in Figure 3.24. The *Size* node that usually defines the size of the mesh elements for all the model was overridden by the *Size 1, Size 2*, which were a domain and a boundary node, respectively. The fist defined the dimension of the mesh elements inside the façade channel, and the second along its boundary. To ensure a correct modeling of the air buoyancy phenomena the maximum dimension of these nodes was set around 0.01 m. On the remaining domains the instruction given by *Size 1* and *Size 2* were combined with the ones Distribution sub-node. The mesh independence was achieved by meshing the model with 4920 domain elements and 860 boundary ones, with an average element skewness of 0.95.

The results obtained under these hypotheses are presented in Figure 3.25
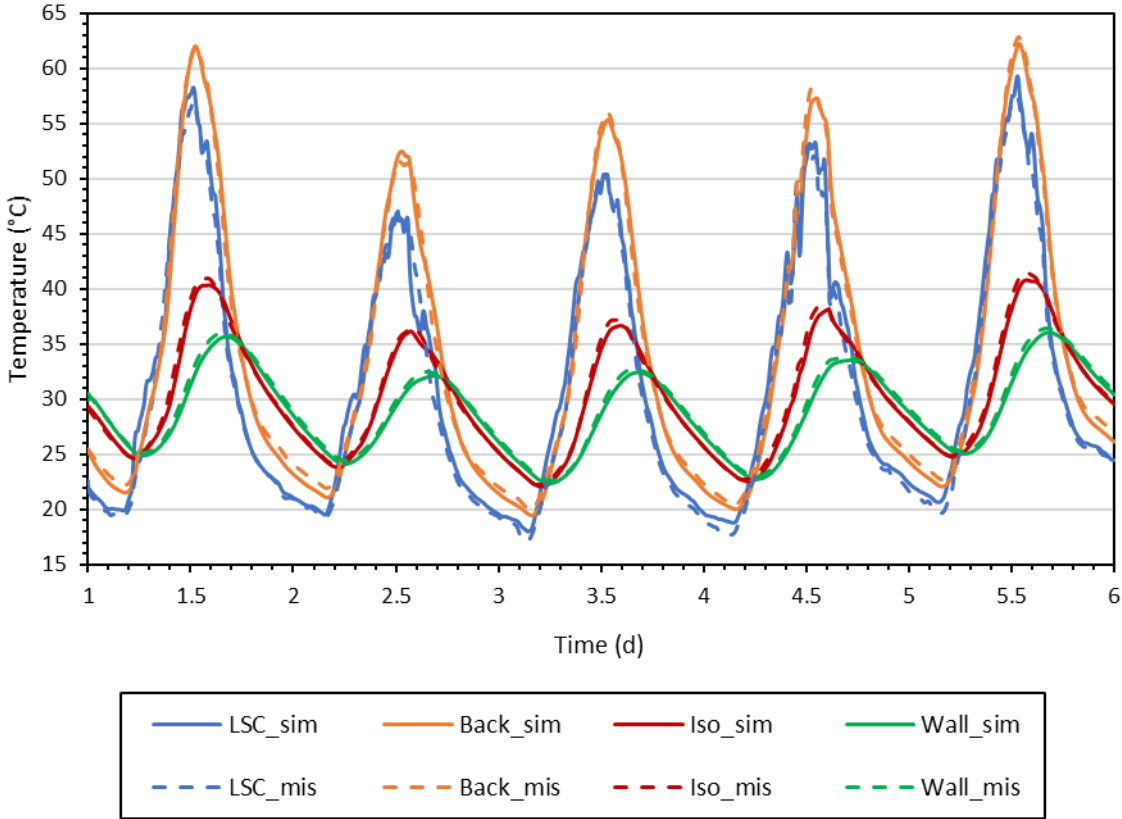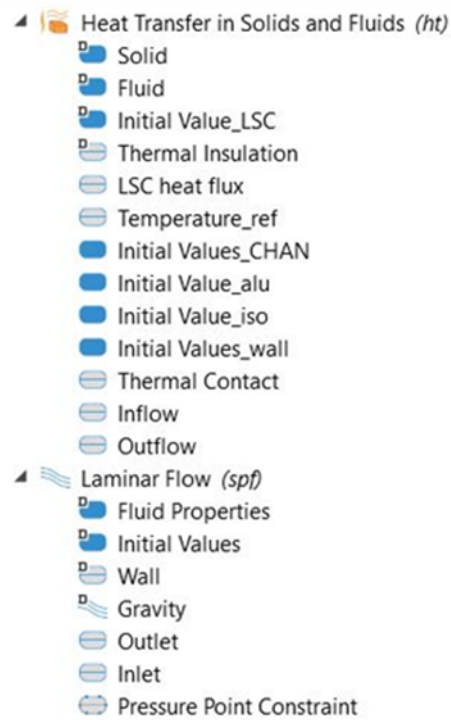

Figure 3.25 Comparison between measured (dashed lines) and simulated (continuous lines) temperature of the façade layers.

3.3.2 Open Façade model

This model was developed to resemble the configuration in which the ventilation channel was open, and the data acquisition campaign lasted from the 07th to the 15th of September 2021. Thermal and optical properties of the simulated materials were left unchanged with respect to the closed configuration model discussed in the Paragraph *3.3.1 Closed Façade model*. The only changes involved the flow condition and the implementation of two fluid domains, one on the bottom and one on the top of the channel. Their addition was discretionary, and they were modeled as rectangles having the width of the channel, and different height, namely 0.5 m for the top domain and of 0.13 m for the bottom one. The top domain was useful to better analyze the fluid flow near to the channel outlet, whereas the bottom one was added to consider the impact of the reflective floor on the air cavity. It was simulated 0.13 m high, as this height allowed to confer to its bottom reasonable boundary conditions for both HT and SPF interfaces. Considering the additional domains and the different situation, some changes in the flow conditions were mandatory. Indeed, the natural ventilated situation required the addition of two sub-nodes for both the HT and SPF interfaces. The first sub-node, termed as *Inflow* (for HT) and *Inlet* (for SPF), was implemented along the bottom boundary of the lower fluid domain, and simulated the presence of air entering the channel. The second sub-node was implemented to model the air exiting the channel, thus was placed on the top boundary of the upper fluid domain, and it was defined as *Outflow* (HT) or *Outlet* (SPF). In Figure 3.27 the added domains and the inlet and outlet sub-nodes are shown. The sub-node Inflow in the HT physics imposed the air temperature at the channel inlet, and it was forced to be two degrees higher with respect to the ambient temperature, since the air temperature measured under the channel and in the proximity of the reflecting floor was on average around that value. At the same time the same boundary was simulated as an inlet with zero pressure condition (ambient condition) in the SPF interface. The channel outlet was defined with the same boundary condition (ambient condition) for the SPF physics, and it was just defined as outflow in the HT one. As for the material properties the meshing procedure was almost identical to the one described in Paragraph *3.3.1 Closed Façade model*. The only difference was the meshing the new domains that was performed in the same manner as for the aur cavity. The mesh independence was achieved with 5276 domain elements and 1142. The Mesh Plot as well as the Mesh Model builder is presented in Figure 3.26 and the average element skewness was equal to 0.96.
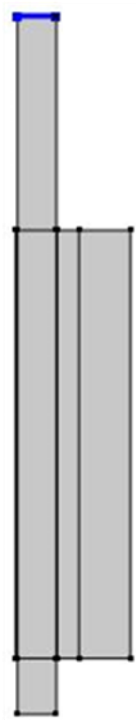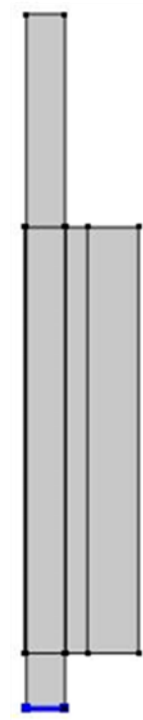
*Figure 3.26 (a) Model builder list and graphical representation of the air cavity,
(b)outflow (HT)/outlet (SPF), and (c) inflow (HT)/inlet (SPF).*
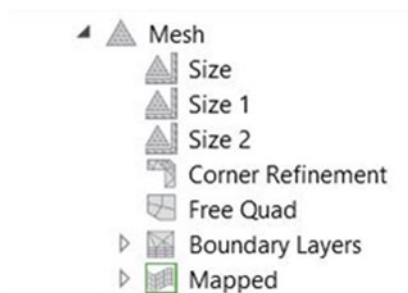
*Figure 3.27 (a) Mesh model builder of the open configuration model and (b) the relative mesh plot, reporting
the skewness color map as quality parameter.*

The comparison between the measured and simulated data is reported in Figure 3.28.

Figure 3.28 Comparison between measured (dashed lines) and simulated (continuous lines) temperature of the façade layers.

3.3.3 Data comparison

To give a quantitative examination of the simulated data, they were compared with the measured ones by using the statistical indices presented in the Wijesuriya et al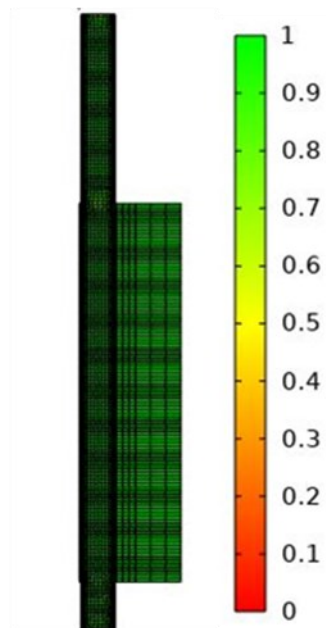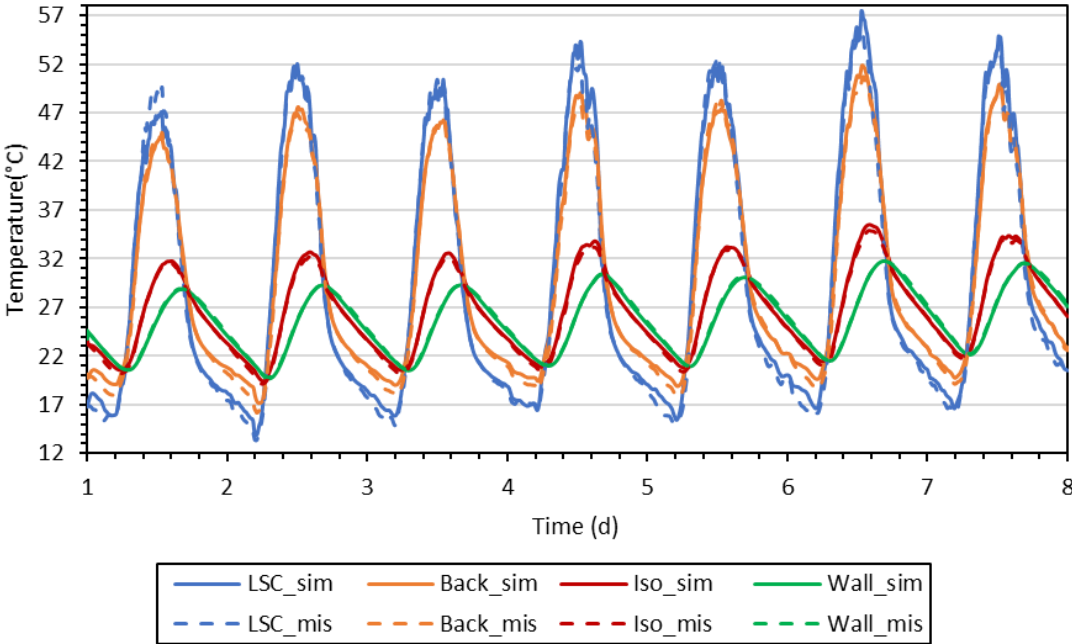 work [137]. They presented two different indices named Coefficient of Variation of the Root Mean Square Error (CVRMSE) and Normalized Mean Biased Error (NMBE). The study [137], in accordance with ASHRAE Guideline 14, considered an NMBE between ±5% and a CVRMSE between ±15% as high standard calibration criteria. These indices were defined as follow:

$$(3.17) \quad NMBE = \frac{1}{y_m}\left(\frac{\sum_{i=1}^{N}(y_i - \hat{y}_i)}{N}\right) \cdot 100$$

$$(3.18) \quad CVRMSE = \frac{1}{y_m}\sqrt{\frac{\sum_{i=1}^{N}(y_i - \hat{y}_i)^2}{N}} \cdot 100$$

where $\hat{y}_i$ were the simulated data, y_i the measured one, and y_m the mean of the measured data.

The values obtained from the comparison of the data collected for this thesis are reported in Table 3.7, according to which the models can be considered calibrated and validated.

Table 3.7 NMBE and CVRMSE of the closed and open configurations.

	Closed Façade configuration				Open Façade configuration			
	T_{LSC}	T_{Back}	T_{Iso}	T_{Wall}	T_{LSC}	T_{Back}	T_{Iso}	T_{Wall}
NMBE (<±5%)	2.3%	-0.83%	-1.2%	-1.4%	1.1%	1.1%	0.43%	-0.14%
CV(RMSE) (<±15%)	4.2%	2.1%	1.9%	1.6%	6.1%	5.4%	2.1%	0.8%

CHAPTER 4

Extension of the model

The aim of this chapter is to extend the model validated within *CHAPTER 3*, by implementing the described VF system to perform the retrofit of an existing building. The thermal performance of the developed VF was estimated by modeling the bare wall of an existing building and the same wall with the addition of the VF. The model was extended for typical days of both summer and winter, with a change in the boundary conditions according to the season. In particular, the description of the developed model and some conclusions regarding the thermal performance of the designed ventilated system are presented.

4.1 Bare wall model

The model of the existing building consisted in a three bricks wall made of Fired Clay Brick and finished with 0.02 m of plaster on both sides. The bricks and plaster thermal properties were defined according to Vijayan et al [138] and Pavlík et al work [139], respectively. Because of the extended wavelength range under consideration, the optical properties of the external plaster were acquired by combining several literature works [140,141], as for the above-mentioned materials optical properties. The system thermal properties and the values attributed to the plaster emissivity are summarized in Table 4.1 and Table 4.2.

Table 4.1 List of the thermal properties attributed to wall and plaster.

	Wall	Plaster
λ (W/(m·K))	0.7	1.61
ρ (kg/m^3)	1650	2064
C_p (J/(kg·K))	820	845

Table 4.2 Emissivity values attributed to the plaster surface and to the ambient

λ_{start} (μm)	λ_{end} (μm)	$\varepsilon_{plaster}$	ε_{amb}
0	0.8	0.05	1
0.8	2.5	0.55	1
2.5	8	0.7	1
8	13	0.7	0.3
13	25	0.7	0.9

Figure 4.1 (a) displays the section of the model builder in which the elements inserted in the HT interface and the surface added to the RAD physics are presented, whereas Figure 4.1 (b) and (c) shows the model structure. The imposed boundary conditions were the same of the model described in *CHAPTER 3* i.e., the GNI, the ambient temperature and the forced convective heat flux due to wind.

They were measured with the same data acquisition software, and the data were collected from 13 to 16 February 2021 for the winter season, and from 19 to 22 July 2021 for the summer one. The models geometry consisted of three rectangles 1 m high and with

different widths, the central one that was created to model the three bricks wall was 0.38 m thick, whereas the lateral ones that modeled the finishing plaster had a width of 0.02 m. As in the previous models the material labeled as _surf was a boundary one defining the plaster optical properties, whereas the others were domain materials, used to confer the bulk properties. Figure 4.1 (b) shows that also in this configuration all the domains were added to the HT node, and they were defined as solid materials (the Fluid sub-node is a default node of the physics that can not be eliminated, but it was empty). The *Initial values* sub-nodes were used to define the initial value of each domain, the one labeled by *Initial values ext* was attributed to the external plaster, whereas the one labeled by *Initial values int* was attributed to the remaining domains.
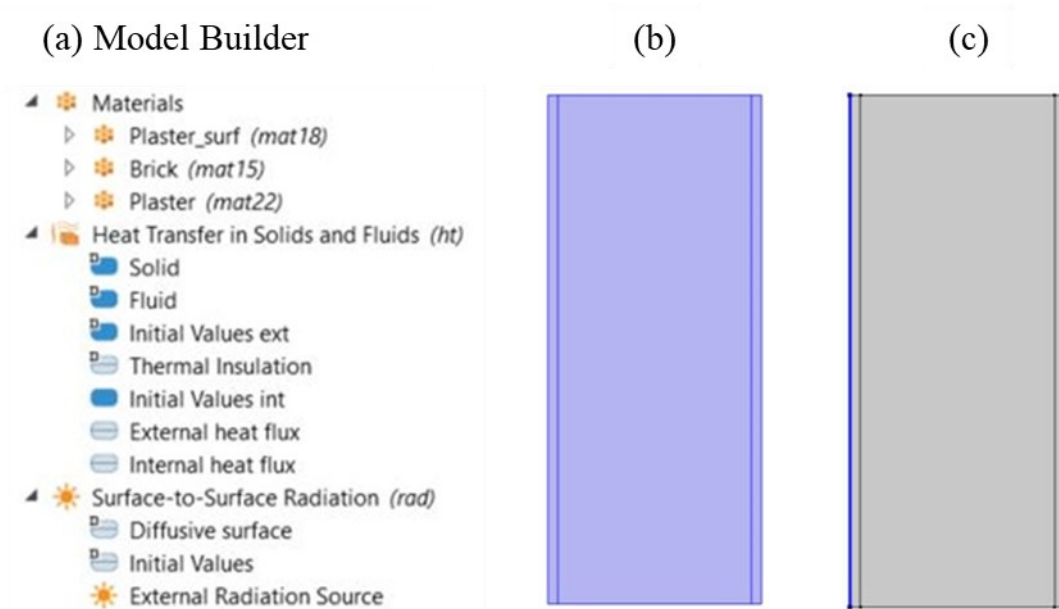

Figure 4.1 (a) Model Builder, (b) highlight of the elements inserted in the HT physics, (c)highlight of the elements inserted in the RAD interface

The initial temperature of *Initial values ext* was set equal to the external temperature measured at the beginning of the data acquisition campaign. The *Initial values int* was set equal to a characteristic temperature labeled *T_in*, which was set to 20 °C for the winter season and to 26 °C for the summer one. For this model both the internal and external temperatures were employed to define a convective heat flux that was modeled thanks to the respective node by using Equation (3.12) (see Figure 4.1 (a)). For the *External heat flux* node, the value of h was computed thanks to Equation (3.10), in which T was the temperature of the external plaster surface. For the *Internal heat flux* node, T_{ext} was instead defined as the internal temperature *T_in*, T was the temperature of the internal plaster surface, and h was set to 4 W/(m^2 K), as in the Corrao and La Placa work [30].

The *External radiation Source* was a point like source at an infinite distance from the system, with an intensity equal to the measured GNI. Since the plaster is an opaque material, the external plaster surface was the only one inserted in the RAD interface (see Figure 4.1 (c)), and it was modeled as a diffusive surface, having the emissivity values listed Table 4.2.

Due to the absence of fluids, the model was meshed using two Mapped nodes, one for the wall domain and one for the plaster ones. Also in this simulation only the distribution along the domain width were specified, as the meshing parameters along the height were handled thanks to the Size node. The Mesh Plot as well as the Mesh Model builder are presented in Figure 4.2. Thanks to the presence of only solid domains the mesh independence was achieved by meshing the model with 1400 domain elements and 212 boundary elements with an average element quality of 0.99.
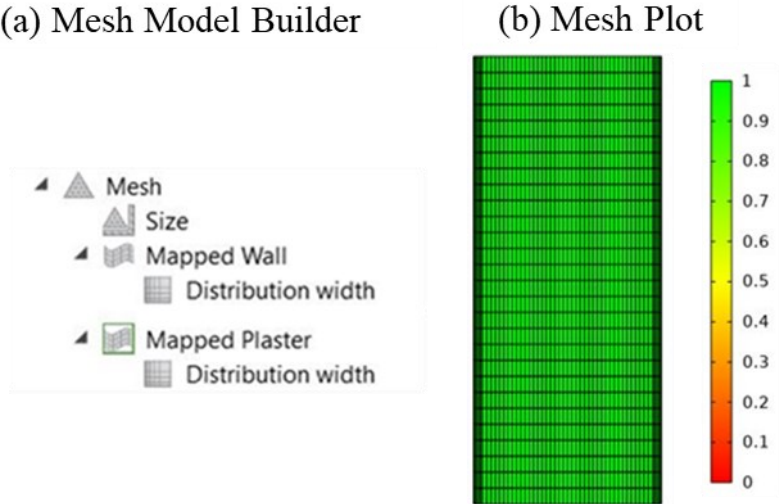

Figure 4.2 (a) Mesh model builder of the bare wall configuration and (b) the relative mesh plot, reporting the skewness color map as quality parameter.

4.2 Closed façade model

To evaluate the thermal performance of the VF a combination between the model presented in *3.3.1 Closed Façade model* and the one displayed in the previous paragraph was developed. In fact geometrical, thermal, and optical properties of the LSC panel, and of the channel domains were identical to the ones defined in the Paragraph *3.3.1 Closed Façade model*, whereas the domain called "wall" and the "internal plaster" were modeled as described in Paragraph *4.1 Bare wall model*. The novelties lied in the properties attributed to the insulating layer and in the technique used to model the aluminum panel. In order to model a more ecological retrofit of the building, the insulating layer used for the validation procedure was substituted with an insulating countertop 0.02 m thick and made of coconut fiber. Its thermal properties were taken from [124], and were defined as $\lambda = 0.043$ W/(m·K), $\rho = 100$ kg/m^3, $c_p = 1300$ J/(kg·K). The change in the modeling of the aluminum slab was instead driven by the willingness to decrease the computational cost of the simulation, in fact, since its thickness was at least one order of magnitude lower than the average size considered in the model, it could be modeled as a *Thin Layer*. Thin Layers are boundary domains for which the number of elements defined to mesh their thickness is ignored from the Mesh node and must be specified within the Material one as the thermal and optical properties. This expedient allowed to reduce the number of mesh elements created for the model, decreasing the total computational costs. This option was not applicable for the models described in *CHAPTER 3* because of the necessity to define a thermal contact node between the aluminum and the insulation layer. However, its thermal and optical properties were kept equal to ones listed in Table 3.6 and Table 3.3. In Figure 4.3 the components inserted in each physics are summarized.

The heat flux sub-nodes were defined in the same way of Paragraph *4.1 Bare wall model*, where in particular the *LSC heat flux* corresponded to the *External heat flux* sub-node. Once again, the environmental data collected in July and February were used as GNI, ambient temperature, and to calculate h. Furthermore, the SPF and RAD node, as well as the Mesh one, were structured as described in Paragraph *3.3.1 Closed Façade model*. The Mesh independence were achieved thanks to 4350 domain elements and 958 boundary elements.
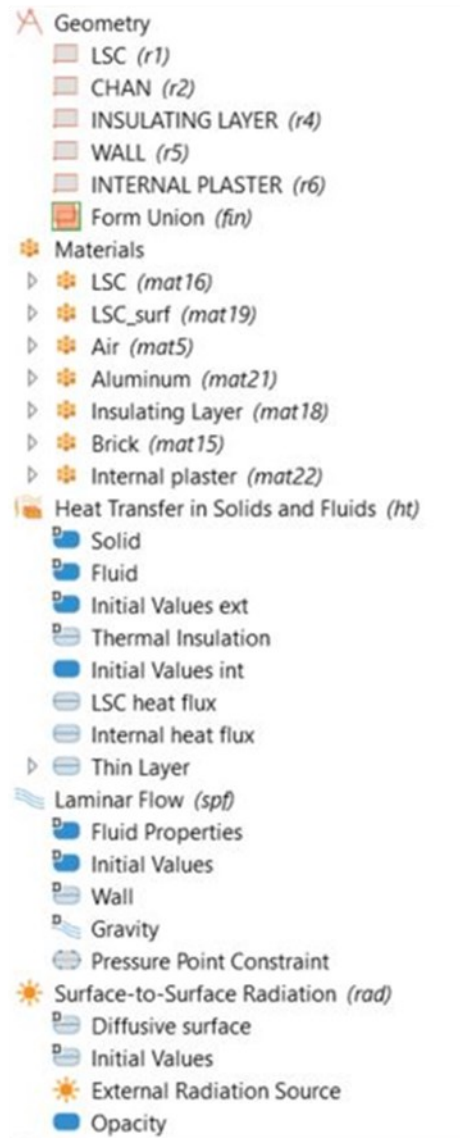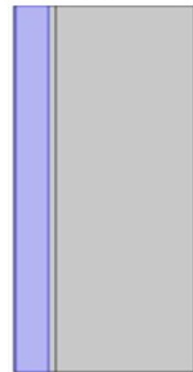
Figure 4.3 Extended closed facade model (a) Model Builder, (b) domain inserted in the HT, (c) SPF, and (d) RAD interfaces

4.3 Open façade model

The thermal performance of the open configuration was obviously investigated only for the summer season, and the model was derived from a combination between the one presented in the paragraph *3.3.2 Open Façade model* and *4.2 Closed façade model*. In fact, the model structure was the one described in the previous paragraph, but the channel with the relative additional domain was modeled as in the homonymous section of *CHAPTER 3*.
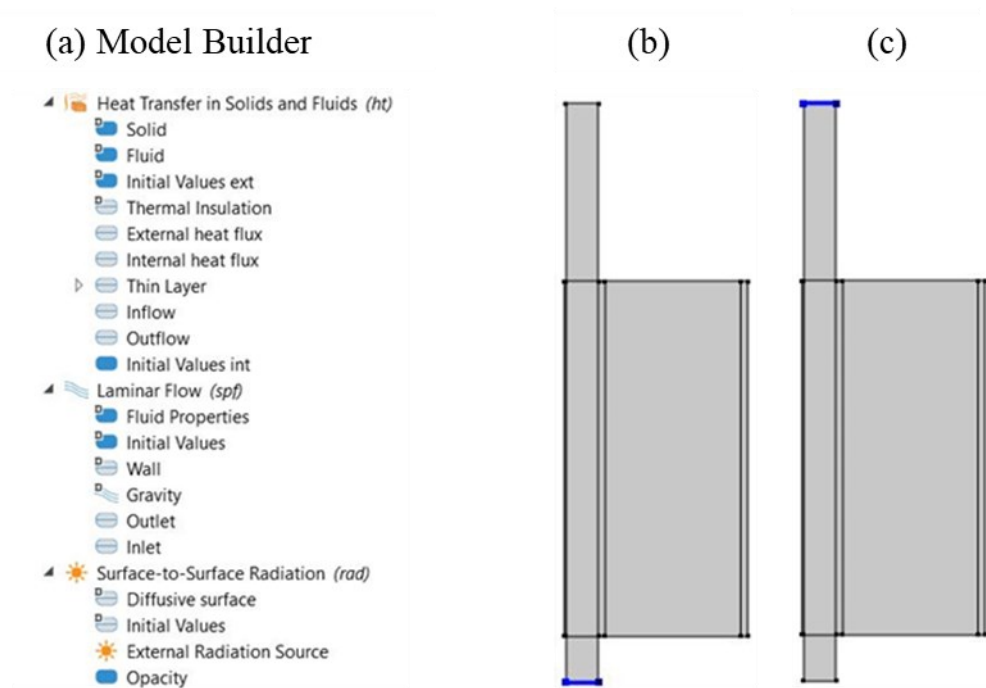

Figure 4.4 (a) Model builder list and graphical representation of the air cavity (b) inflow (HT)/inlet (SPF) and (c) outflow (HT)/outlet (SPF).

The inlet boundary condition (Figure 4.4 (b)) was kept equal to ambient condition for SPF node, whereas it was modified in the HT interface by eliminating the increase with respect to the ambient temperature. Moreover, this model allowed a performance evaluation in a mechanically ventilated configuration. This assessment was done by changing the SPF boundary condition at the channel outlet Figure 4.4 (c), in fact the ambient condition (zero-pressure condition) was substituted with a normal outflow velocity equal to 5 m/s. The outflow velocity vector was modeled with this magnitude, as it was a value that could be generated by a ventilation system directly powered from the LSC panel. The inlet and outlet nodes as well as the system model builder are shown in Figure 4.4. The procedure used to mesh the model was identical to the one described in 3.3.2 Open Façade model, and

in this case the mesh independence was achieved by meshing the model with 6435 domain elements and 1206 boundary elements and an average element quality of 0.97.

4.4 Comparison of the results

The obtained results were analyzed by comparing the normal total heat flux that crossed the boundary between the internal plaster and the wall. In Figure 4.5 are presented the result for both the winter and the summer configuration.
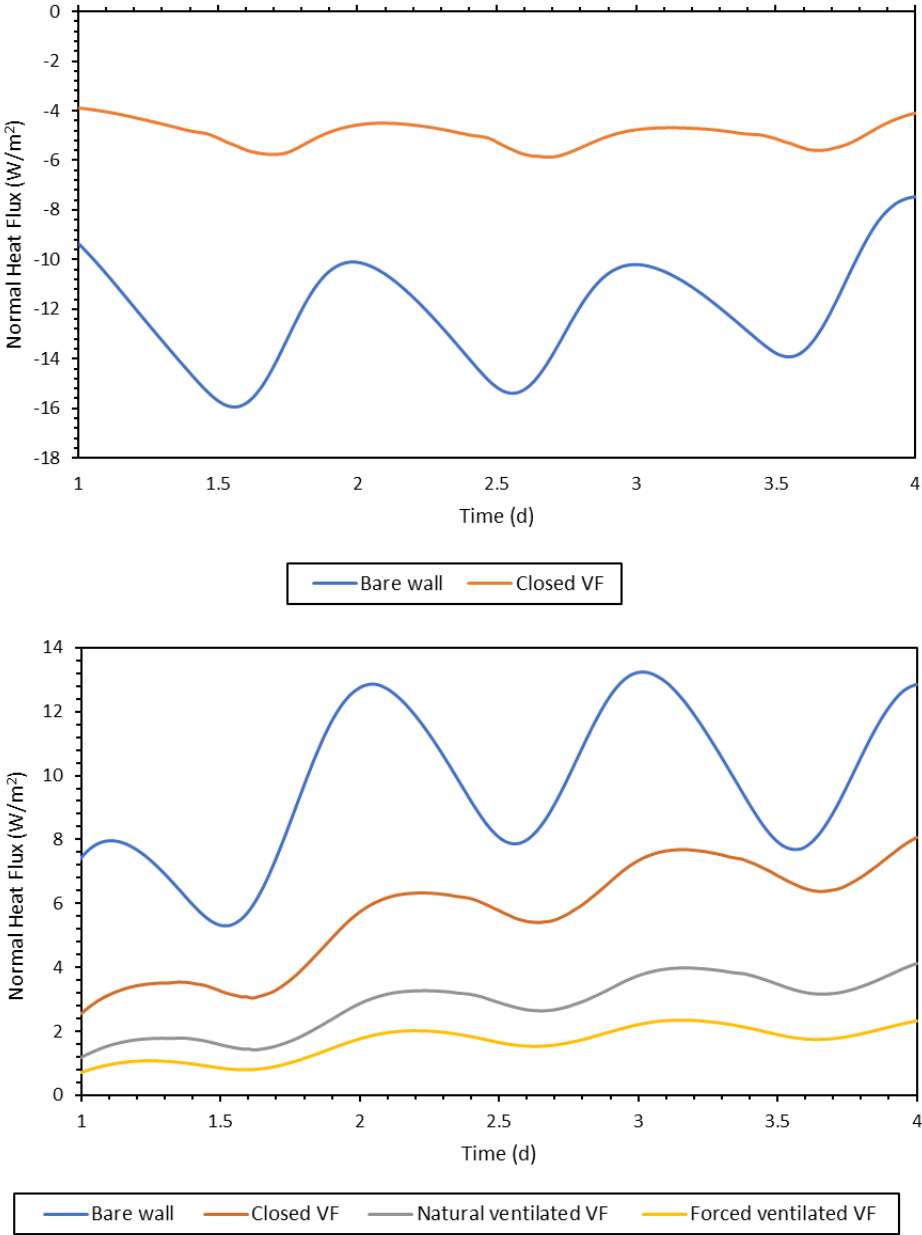

Figure 4.5 total heat flux that crossed the boundary between the wall and the internal plaster during both (a) winter season, and (b) summer one.

Where the flux was defined as positive when the heat flowed into the building, so a negative flux value means that the heat was exiting the building. Figure 4.5 shows that the implementation of the VF increased the system thermal insulation (decreased the outgoing flux) during winter, and decreased the ingoing heat flux during summer, thus reducing the building energy load associated to both heating and cooling needs. Moreover, from Figure 4.5 (b) it is evident that a mechanical ventilation during summer can be a further asset to lower the thermal load, especially if it can be powered by the LSC panel. This result is highlighted also from Figure 4.6 reporting the temperature of the whole system in °C under different cavity configurations.
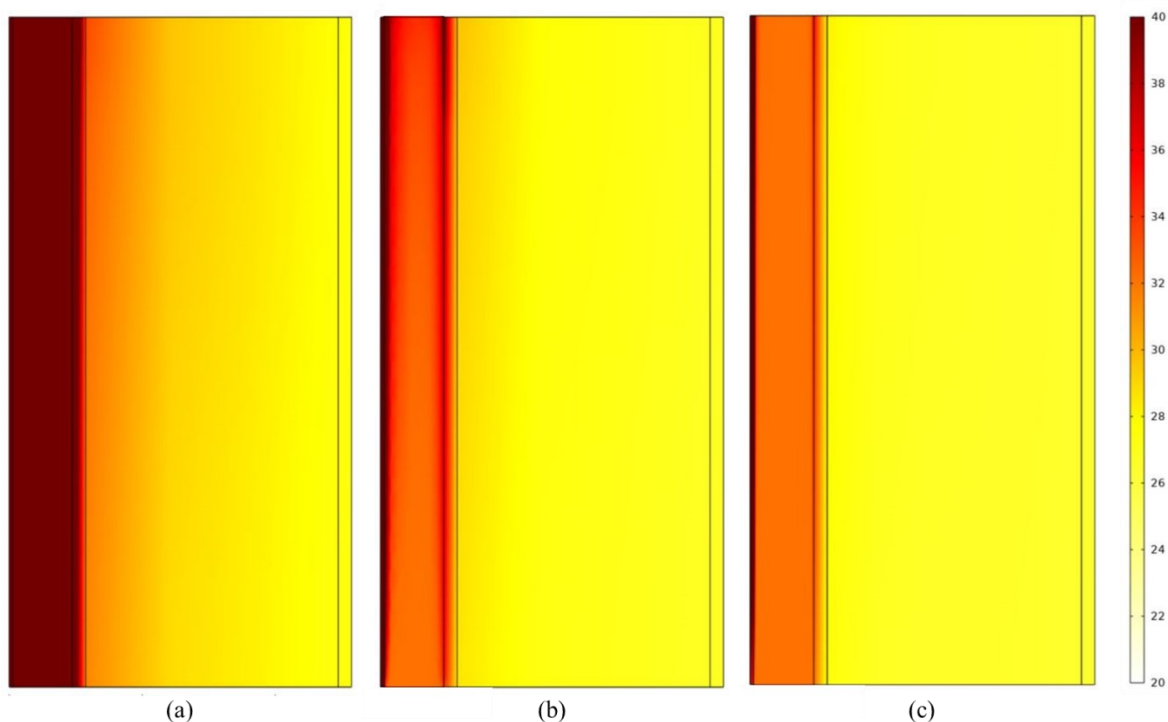
Figure 4.6 Results of the simulation concerning the (a) closed, (b) natural ventilated, and (c) mechanically ventilated façade, presenting a color map of the system temperature expressed in °C.

Finally, the thermal transmittance of the ventilated system was compared to the maximum values prescribed by the Italian directive. These values depend on the building element nature (transparent or opaque element), their installation position (vertical or horizontal), and on the geographical area. in which the building is situated. Indeed, according to the directive EN ISO 15927-6 the Italian territory could be subdivided in several zones that are discerned by a parameter called Degree Days (DD). The DD estimated the cumulative difference between a conventional ambient temperature (different for each country) and the average daily outdoor temperature, so they can be defined as:

$$(4.1) \quad DD = \sum_{d=1}^{n}(T_0 - T_e)$$

where d is a counter that identifies the considered number of days, T_e is the average daily outdoor temperature, and T_0 is the conventional ambient temperature, which for the Italian directive is equal to 20 °C. This definition is correct only if the cumulative difference is considered positive, i.e., the terms that contribute to the summation are the one for which $T_e < T_0$. In Table 4.3 the information regarding different zones is summarized.

Table 4.3 Information regarding the number of degree days in the different geographical zones

Zone	Range of DD	Start date	End date
A	0 - 600	1st Dec	15th Mar
B	601 - 900	1st Dec	31st Mar
C	901 - 1400	15th Nov	31st Mar
D	1401 - 2100	1st Nov	15th Apr
E	2101 - 3000	15th Oct	15th Apr
F	3001 - +∞	all year	

In Figure 4.7 is reported a choropleth map of Italy that associates each zone with the maximum thermal transmittance value prescribed by the national directive. This value for opaque vertical structures in Ferrara (Zone E) is 0.28 W/(m^{2}K) and for the VF system developed in this work (LSC panel, cavity, aluminum pane, and insulation layer) a mean value of 0.29 W/(m^{2}K) was estimated.

Zone A e B
λ<0.40 W/(m²K)

Zone C
λ <0.36 W/(m²K)

Zone D
λ<0.32 W/(m²K)

Zone E
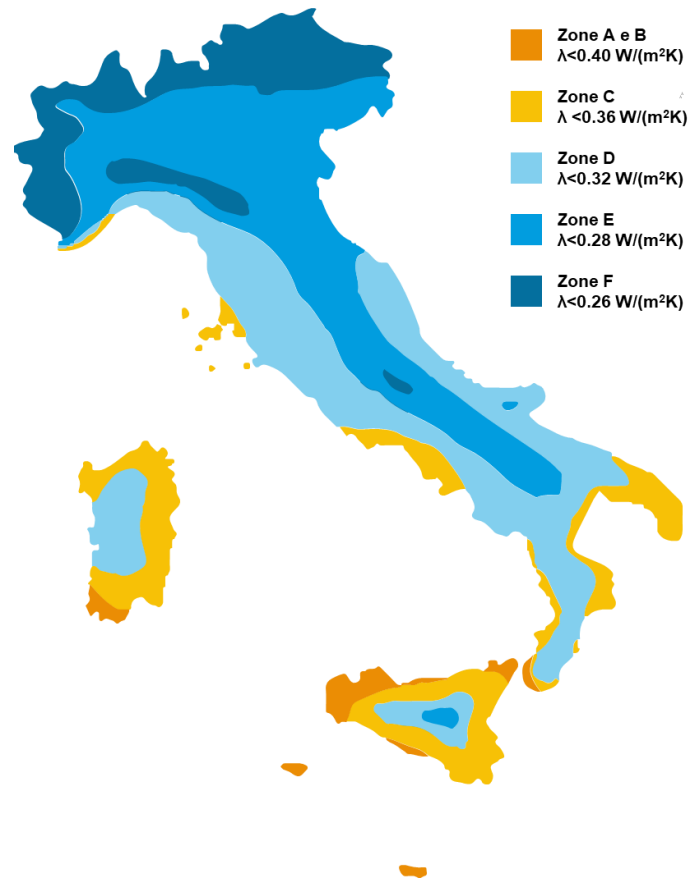λ<0.28 W/(m²K)

Zone F
λ<0.26 W/(m²K)

Figure 4.7 Choropleth map of the differ zones with the associated maximum conductance value.

Conclusions

This thesis work concerned the development of a photovoltaic ventilated façade for the control of buildings thermal budget integrating a LSC panel as external skin. The system was developed with the intention to exploit its optical properties to increase building thermal efficiency minimizing the cavity width and thus the retrofit footprint. In fact, the high transparency of the LSC ensured to increase the solar radiation reaching the internal skin, if compared with traditional solar panels. Moreover, the LSC aesthetical appearance opened the possibility to create a back panel that increased the façade aesthetic appealing optimizing the solar radiation harvesting, according to the building energy needs.

Firstly, the optical and electrical performance of large area LSC panels were investigated, as they are usually studied for small devices, which dimensions were not so suitable for BIPV application. The results highlighted that contrary to what happens for panels of small dimensions, a slab with a lower dye concentration turned to be more suitable for this type of application. In fact, organic dyes are often characterized by self-absorption phenomena that diminish when low concentration are used. Lumogen® Red 305 was chosen as luminophore as it was one of the most efficient organic dyes, and its price per kilogram ensured a competitive price to watt ratio, if compared with other semitransparent PV technologies.

Secondly, the comparison between two models created with COMSOL Multiphysics and experimental data allowed the development and of thermal simulations having a maximum NMBE and CV(RMSE) value of 1.1% and 6.1% respectively, which are values far below the threshold for which a model can be considered validated. The obtained thermal and optical properties were then implemented in new COMSOL models created to perform the retrofit of a typical building envelope in both summer and winter. The results demonstrated that a narrow VF implementing an LSC panel as external skin, and an aluminum pane as internal one, improved the building thermal load both in heating and cooling season. Moreover, if properly managed, the addition of a mechanical ventilation system to the cavity that is directly powered by the external pane was a further asset to reduce the thermal load.

Finally, the comparison between the system thermal transmittance, 0.29 W/(m^{2}K), and the maximum values prescribed by the Italian directive, 0.28 W/(m^{2}K), underlined a promising result for a "proof of concept" research work.

Considering the high transparency of LSC panels, further works will regard their coupling with passive material commonly used to increase building thermal comfort, like phase change materials or thermochromic paints, or their implementation in transparent façades in combination with adaptive shading technologies directly powered by the LSC.

Bibliography

[1]   EUR-Lex, Renewable Energy Directive 2018/2001/EU, (n.d.).

[2]   EUR-Lex, Energy Efficiency Directive 2012/27/EU, (n.d.). https://eur-
        lex.europa.eu/legal-content/EN/TXT/?uri=celex%3A32012L0027 (accessed March
        15, 2021).

[3]   G.M. Wilson, A.-J. Mowafak, W.K. Metzger, S.W. Glunz, P. Verlinden, G. Xiong,
        L.M. Mansfield, B.J. Stanbery, K. Zhu, Y. Yan, J.J. Berry, A.J. Ptak, F. Dimroth,
        B.M. Kayes, A.C. Tamboli, R. Peibst, K. Catchpole, M.O. Reese, C.S. Klinga, P.
        Denholm, M. Morjaria, M.G. Deceglie, J.M. Freeman, M.A. Mikofski, D.C. Jordan,
        G. TamizhMani, D.B. Sulas-Kern, The 2020 Photovoltaic Technologies Roadmap, J.
        Phys. D. Appl. Phys. 53 (2020).

[4]   International Energy Agency, Renewables 2020 - Solar PV, (n.d.).
        https://www.iea.org/reports/renewables-2020/solar-pv.

[5]   T. Blaschke, M. Biberacher, S. Gadocha, I. Schardinger, "Energy landscapes":
        Meeting energy demands andhuman aspirations, Biomass and Bioenergy. 55 (2013)
        3–16. https://doi.org/10.1016/j.biombioe.2012.11.022.

[6]   G.A. Barron-Gafford, R.L. Minor, N.A. Allen, A.D. Cronin, A.E. Brooks, M.A.
        Pavao-Zuckerman, The photovoltaic heat island effect: Larger solar power plants
        increase local temperatures, Sci. Rep. 6 (2016) 1–7.
        https://doi.org/10.1038/srep35070.

[7]   U.N. Environment, Towards a zero-emission, efficient, and resilient buildings and
        construction sector, 2017. www.globalabc.org.

[8]   D. D'Agostino, L. Mazzarella, What is a Nearly zero energy building? Overview,
        implementation and comparison of definitions, J. Build. Eng. 21 (2019) 200–212.
        https://doi.org/10.1016/j.jobe.2018.10.019.

[9]   EUR-Lex, Energy Performance of Buildings Directive 2018/844/EU, (n.d.).
        https://eur-lex.europa.eu/legal-
        content/EN/TXT/?uri=uriserv%3AOJ.L_.2018.156.01.0075.01.ENG (accessed
        February 13, 2021).

[10]   EUR-Lex, Guidelines accompanying Commission Delegated Regulation (EU) No 244/2012, (n.d.). https://eur-lex.europa.eu/legal-content/EN/ALL/?uri=CELEX%3A52012XC0419%2802%29.

[11]   M. Panagiotidou, R.J. Fuller, Progress in ZEBs-A review of definitions, policies and construction activity, Energy Policy. 62 (2013) 196–206. https://doi.org/10.1016/j.enpol.2013.06.099.

[12]   H. Lund, A. Marszal, P. Heiselberg, Zero energy buildings and mismatch compensation factors, Energy Build. 43 (2011) 1646–1654. https://doi.org/10.1016/j.enbuild.2011.03.006.

[13]   L. De Boeck, S. Verbeke, A. Audenaert, L. De Mesmaeker, Improving the energy performance of residential buildings: A literature review, Renew. Sustain. Energy Rev. 52 (2015) 960–975. https://doi.org/10.1016/j.rser.2015.07.037.

[14]   H.Y. Chan, S.B. Riffat, J. Zhu, Review of passive solar heating and cooling technologies, Renew. Sustain. Energy Rev. 14 (2010) 781–789. https://doi.org/10.1016/j.rser.2009.10.030.

[15]   E. Halawa, A. Ghaffarianhoseini, A. Ghaffarianhoseini, J. Trombley, N. Hassan, M. Baig, S.Y. Yusoff, M. Azzam Ismail, A review on energy conscious designs of building façades in hot and humid climates: Lessons for (and from) Kuala Lumpur and Darwin, Renew. Sustain. Energy Rev. 82 (2018) 2147–2161. https://doi.org/10.1016/j.rser.2017.08.061.

[16]   F. Pomponi, P.A.E. Piroozfar, R. Southall, P. Ashton, E.R.P. Farr, Energy performance of Double-Skin Façades in temperate climates: A systematic review and meta-analysis, Renew. Sustain. Energy Rev. 54 (2016) 1525–1536. https://doi.org/10.1016/j.rser.2015.10.075.

[17]   I. Visa, M. Comsit, A. Duta, Urban acceptance of facade integrated novel solar thermal collectors, Energy Procedia. 48 (2014) 1429–1435. https://doi.org/10.1016/j.egypro.2014.02.161.

[18]   T. Matuska, B. Sourek, Façade solar collectors, Sol. Energy. 80 (2006) 1443–1452. https://doi.org/10.1016/j.solener.2006.04.006.

[19]   M.C. Munari Probst, C. Roecker, Towards an improved architectural quality of

building integrated solar thermal systems (BIST), Sol. Energy. 81 (2007) 1104–1116. https://doi.org/10.1016/j.solener.2007.02.009.

[20] M.A. Shameri, M.A. Alghoul, K. Sopian, M.F.M. Zain, O. Elayeb, Perspectives of double skin façade systems in buildings and energy saving, Renew. Sustain. Energy Rev. 15 (2011) 1468–1475. https://doi.org/10.1016/j.rser.2010.10.016.

[21] Q. Liu, F. Cao, Y. Liu, T. Zhu, D. Liu, Design and simulation of a solar chimney PV/T power plant in Northwest China, Int. J. Photoenergy. 2018 (2018). https://doi.org/10.1155/2018/1478695.

[22] O.K. Ahmed, A.S. Hussein, New design of solar chimney (case study), Case Stud. Therm. Eng. 11 (2018) 105–112. https://doi.org/10.1016/j.csite.2017.12.008.

[23] S. Pantic, L. Candanedo, A.K. Athienitis, Modeling of energy performance of a house with three configurations of building-integrated photovoltaic/thermal systems, Energy Build. 42 (2010) 1779–1789. https://doi.org/10.1016/j.enbuild.2010.05.014.

[24] P.A. Mirzaei, J. Carmeliet, Influence of the underneath cavity on buoyant-forced cooling of the integrated photovoltaic panels in building roof: a thermography study, Prog. Photovoltaics Res. Appl. 23 (2015) 19–29.

[25] A.K. Athienitis, G. Barone, A. Buonomano, A. Palombo, Assessing active and passive effects of façade building integrated photovoltaics/thermal systems: Dynamic modelling and simulation, Appl. Energy. 209 (2018) 355–382. https://doi.org/10.1016/j.apenergy.2017.09.039.

[26] J.C. Ortiz Lizcano, Z. Haghighi, S. Wapperom, C. Infante Ferreira, O. Isabella, A. v. d. Dobbelsteen, M. Zeman, Photovoltaic chimney: Thermal modeling and concept demonstration for integration in buildings, Prog. Photovoltaics Res. Appl. 28 (2020) 465–482. https://doi.org/10.1002/pip.3194.

[27] V. Timchenko, O.A. Tkachenko, S. Giroux-Julien, C. Ménézo, Numerical and experimental investigation of natural convection in open-ended channels with application to building integrated photovoltaic (BIPV) systems, EPJ Web Conf. 92 (2015). https://doi.org/10.1051/epjconf/20159201002.

[28] C. Balocco, A simple model to study ventilated facades energy performance, Energy Build. 34 (2002) 469–475. https://doi.org/10.1016/S0378-7788(01)00130-X.

[29] M. Ibañez-Puy, M. Vidaurre-Arbizu, J.A. Sacristán-Fernández, C. Martín-Gómez, Opaque Ventilated Façades: Thermal and energy performance review, Renew. Sustain. Energy Rev. 79 (2017) 180–191. https://doi.org/10.1016/j.rser.2017.05.059.

[30] R. Corrao, E. La Placa, Plaster ventilated fa ade system for renovating modern and ancient buildings. A CFD analysis, IOP Conf. Ser. Earth Environ. Sci. 863 (2021). https://doi.org/10.1088/1755-1315/863/1/012046.

[31] Building-integrated Photovoltaics Market Size, Share & Trends Analysis Report By Technology (Crystalline Silicon, Thin Film), By Application (Roofs, Glass), By End Use (Industrial, Commercial), And Segment Forecasts, 2021 - 2028, (n.d.).

[32] H. Onbasioglu, A.N. Egrican, Experimental approach to the thermal response of passive systems, Energy Convers. Manag. 43 (2002) 2053–2065. https://doi.org/10.1016/S0196-8904(01)00138-8.

[33] S. Barbosa, K. Ip, Perspectives of double skin façades for naturally ventilated buildings: A review, Renew. Sustain. Energy Rev. 40 (2014) 1019–1029. https://doi.org/10.1016/j.rser.2014.07.192.

[34] M. Petrichenko, A. Ostrovaia, E. Statsenko, The Glass Ventilated Facades – Research of an Air Gap, Appl. Mech. Mater. 725–726 (2015) 87–92. https://doi.org/10.4028/www.scientific.net/amm.725-726.87.

[35] I. Pérez-Grande, J. Meseguer, G. Alonso, Influence of glass properties on the performance of double-glazed facades, Appl. Therm. Eng. 25 (2005) 3163–3175. https://doi.org/10.1016/j.applthermaleng.2005.04.004.

[36] A.L.S. Chan, T.T. Chow, K.F. Fong, Z. Lin, Investigation on energy performance of double skin façade in Hong Kong, Energy Build. 41 (2009) 1135–1142. https://doi.org/10.1016/j.enbuild.2009.05.012.

[37] N. Mingotti, T. Chenvidyakarn, A.W. Woods, Combined impacts of climate and wall insulation on the energy benefit of an extra layer of glazing in the facade, Energy Build. 58 (2013) 237–249. https://doi.org/10.1016/j.enbuild.2012.11.033.

[38] A. Pappas, Z. Zhai, Numerical investigation on thermal performance and correlations of double skin façade with buoyancy-driven airflow, Energy Build. 40 (2008) 466–475. https://doi.org/10.1016/j.enbuild.2007.04.002.

[39] H. Parhizkar, R.A. Khoraskani, M. Tahbaz, Double skin façade with Azolla; ventilation, Indoor Air Quality and Thermal Performance Assessment, J. Clean. Prod. 249 (2020) 119313. https://doi.org/10.1016/j.jclepro.2019.119313.

[40] H. Radhi, S. Sharples, F. Fikiry, Will multi-facade systems reduce cooling energy in fully glazed buildings? A scoping study of UAE buildings, Energy Build. 56 (2013) 179–188. https://doi.org/10.1016/j.enbuild.2012.08.030.

[41] E. Oesterle, R. Lieb, M. Lutz, W. Heusler, Double skin facades: integrated planning; building physics, construction, aerophysics, air-conditioning, economic viability, Prestel, 2001.

[42] E. Biyik, M. Araz, A. Hepbasli, M. Shahrestani, R. Yao, L. Shao, E. Essah, A.C. Oliveira, T. del Caño, E. Rico, J.L. Lechón, L. Andrade, A. Mendes, Y.B. Atlı, A key review of building integrated photovoltaic (BIPV) systems, Eng. Sci. Technol. an Int. J. 20 (2017) 833–858. https://doi.org/10.1016/j.jestch.2017.01.009.

[43] C. Gregório-Atem, C. Aparicio-Fernández, H. Coch, J.L. Vivancos, Opaque ventilated façade (OVF) thermal performance simulation for office buildings in Brazil, Sustain. 12 (2020). https://doi.org/10.3390/su12187635.

[44] J. Falk, K. Sandin, Ventilated rainscreen cladding: A study of the ventilation drying process, Build. Environ. 60 (2013) 173–184. https://doi.org/10.1016/j.buildenv.2012.11.015.

[45] J.E. Gonçalves, T. van Hooff, D. Saelens, Simulating building integrated photovoltaic facades: Comparison to experimental data and evaluation of modelling complexity, Appl. Energy. 281 (2021) 116032. https://doi.org/10.1016/j.apenergy.2020.116032.

[46] E. Gratia, A. De Herde, The most efficient position of shading devices in a double-skin facade, Energy Build. 39 (2007) 364–373. https://doi.org/10.1016/j.enbuild.2006.09.001.

[47] T.E. Jiru, Y.X. Tao, F. Haghighat, Airflow and heat transfer in sustainable building components-double-skin facades, in: 14th Int. Heat Transf. Conf. IHTC 14, 2010. https://doi.org/10.1115/IHTC14-23017.

[48] Y. Ji, M.J. Cook, V.I. Hanby, D.G. Infield, D.L. Loveday, L. Mei, CFD

MODELLING OF DOUBLE-SKIN FAÇADES WITH VENETIAN BLINDS, in: Build. Simul. 2007, 2007: pp. 1491–1498.

[49]   S.K. Chou, K.J. Chua, J.C. Ho, A study on the effects of double skin façades on the energy management in buildings, Energy Convers. Manag. 50 (2009) 2275–2281. https://doi.org/10.1016/j.enconman.2009.05.003.

[50]   M. Haase, F. Marques da Silva, A. Amato, Simulation of ventilated facades in hot and humid climates, Energy Build. 41 (2009) 361–373. https://doi.org/10.1016/j.enbuild.2008.11.008.

[51]   C.M. Lai, S. Hokoi, Solar façades: A review, Build. Environ. 91 (2015) 152–165. https://doi.org/10.1016/j.buildenv.2015.01.007.

[52]   R.H. Crawford, G.J. Treloar, R.J. Fuller, M. Bazilian, Life-cycle energy analysis of building integrated photovoltaic systems (BiPVs) with heat recovery unit, Renew. Sustain. Energy Rev. 10 (2006) 559–575. https://doi.org/10.1016/j.rser.2004.11.005.

[53]   S. Dubey, J.N. Sarvaiya, B. Seshadri, Temperature dependent photovoltaic (PV) efficiency and its effect on PV production in the world - A review, Energy Procedia. 33 (2013) 311–321. https://doi.org/10.1016/j.egypro.2013.05.072.

[54]   J. Peng, L. Lu, H. Yang, J. Han, Investigation on the annual thermal performance of a photovoltaic wall mounted on a multi-layer façade, Appl. Energy. 112 (2013) 646–656. https://doi.org/10.1016/j.apenergy.2012.12.026.

[55]   E. Gratia, A. De Herde, Natural ventilation in a double-skin facade, Energy Build. 36 (2004) 137–146. https://doi.org/10.1016/j.enbuild.2003.10.008.

[56]   S.F. Barkaszi, J.P. Dunlop, Discussion of strategies for mounting photovoltaic arrays on rooftops, Int. Sol. Energy Conf. (2001) 333–338. https://doi.org/10.1115/sed2001-142.

[57]   B.P. Jelle, C. Breivik, H. Drolsum Røkenes, Building integrated photovoltaic products: A state-of-the-art review and future research opportunities, Sol. Energy Mater. Sol. Cells. 100 (2012) 69–96. https://doi.org/10.1016/j.solmat.2011.12.016.

[58]   M.G. Debije, P.P.C. Verbunt, Thirty years of luminescent solar concentrator research: Solar energy for the built environment, Adv. Energy Mater. 2 (2012) 12–35. https://doi.org/10.1002/aenm.201100554.

[59] J. Escarre, H.Y. Li, L. Sansonnens, F. Galliano, G. Cattaneo, P. Heinstein, S. Nicolay, J. Bailat, S. Eberhard, C. Ballif, L.E. Perret-Aebi, When PV modules are becoming real building elements: White solar module, a revolution for BIPV, 2015 IEEE 42nd Photovolt. Spec. Conf. PVSC 2015. (2015) 1–2. https://doi.org/10.1109/PVSC.2015.7355630.

[60] A. Morlier, B. Lim, S. Blankemeyer, H. Schulte-huxel, R. Witteck, T. Daschinger, S. Bräunig, M. Köntges, R. Brendel, Photovoltaic Modules with the Look and Feel of a Stone Façade for Building Integration, in: 2021: pp. 1–8. https://doi.org/10.1002/solr.202100356.

[61] H. Yu, Q. Wang, C. Lu, C. Wei, The research on a new type of BIPV modules constructed by thin-film photovoltaic panel (or module)/PU/color organic-coated steel plate, 2015 IEEE 42nd Photovolt. Spec. Conf. PVSC 2015. (2015) 2724–2727. https://doi.org/10.1109/PVSC.2015.7355824.

[62] M. Pagliaro, R. Ciriminna, G. Palmisano, BIPV: Merging the photovoltaic with the construction industry, Prog. Photovoltaics Res. Appl. 18 (2010) 61–72. https://doi.org/10.1002/pip.920.

[63] N.G. Dhere, N. Shiradkar, E. Schneller, V. Gade, The reliability of bypass diodes in PV modules, Reliab. Photovolt. Cells, Modul. Components, Syst. VI. 8825 (2013) 88250I. https://doi.org/10.1117/12.2026782.

[64] G.Y. Yun, M. McEvoy, K. Steemers, Design and overall energy performance of a ventilated photovoltaic façade, Sol. Energy. 81 (2007) 383–394. https://doi.org/10.1016/j.solener.2006.06.016.

[65] K.E. Park, G.H. Kang, H.I. Kim, G.J. Yu, J.T. Kim, Analysis of thermal and electrical performance of semi-transparent photovoltaic (PV) module, Energy. 35 (2010) 2681–2687. https://doi.org/10.1016/j.energy.2009.07.019.

[66] J. Han, L. Lu, H. Yang, Numerical evaluation of the mixed convective heat transfer in a double-pane window integrated with see-through a-Si PV cells with low-e coatings, Appl. Energy. 87 (2010) 3431–3437. https://doi.org/10.1016/j.apenergy.2010.05.025.

[67] J. Kang, C. Cho, J.Y. Lee, Design of asymmetrically textured structure for efficient light trapping in building-integrated photovoltaics, Org. Electron. 26 (2015) 61–65.

https://doi.org/10.1016/j.orgel.2015.07.021.

[68]   P. Bernardoni, G. Mangherini, M. Gjestila, A. Andreoli, D. Vincenzi, Performance optimization of luminescent solar concentrators under several shading conditions, Energies. 14 (2021). https://doi.org/10.3390/en14040816.

[69]   B.C. Rowan, L.R. Wilson, B.S. Richards, Advanced material concepts for luminescent solar concentrators, IEEE J. Sel. Top. Quantum Electron. 14 (2008) 1312–1322. https://doi.org/10.1109/JSTQE.2008.920282.

[70]   C. Tablero, Quantum dot energy levels and spectrum for different geometries, J. Appl. Phys. 106 (2009). https://doi.org/10.1063/1.3243290.

[71]   T. Wang, J. Zhang, W. Ma, Y. Luo, L. Wang, Z. Hu, W. Wu, X. Wang, G. Zou, Q. Zhang, Luminescent solar concentrator employing rare earth complex with zero self-absorption loss, Sol. Energy. 85 (2011) 2571–2579. https://doi.org/10.1016/j.solener.2011.07.014.

[72]   S.M. El-Bashir, F.M. Barakat, M.S. Alsalhi, Metal-enhanced fluorescence of mixed coumarin dyes by silver and gold nanoparticles: Towards plasmonic thin-film luminescent solar concentrator, J. Lumin. 143 (2013) 43–49. https://doi.org/10.1016/j.jlumin.2013.04.029.

[73]   J.C. Goldschmidt, M. Peters, A. Bösch, H. Helmers, F. Dimroth, S.W. Glunz, G. Willeke, Increasing the efficiency of fluorescent concentrator systems, Sol. Energy Mater. Sol. Cells. 93 (2009) 176–182. https://doi.org/10.1016/j.solmat.2008.09.048.

[74]   N.D. Bronstein, Y. Yao, L. Xu, E. O'Brien, A.S. Powers, V.E. Ferry, A.P. Alivisatos, R.G. Nuzzo, Quantum Dot Luminescent Concentrator Cavity Exhibiting 30-fold Concentration, ACS Photonics. 2 (2015) 1576–1583. https://doi.org/10.1021/acsphotonics.5b00334.

[75]   M. Rafiee, S. Chandra, H. Ahmed, S.J. McCormack, An overview of various configurations of Luminescent Solar Concentrators for photovoltaic applications, Opt. Mater. (Amst). 91 (2019) 212–227. https://doi.org/10.1016/j.optmat.2019.01.007.

[76]   L. Zalewski, M. Chantant, S. Lassue, B. Duthoit, Experimental thermal study of a solar wall of composite type, Energy Build. 25 (1997) 7–18.

https://doi.org/10.1016/s0378-7788(96)00974-7.

[77] T. Pasquay, Natural ventilation in high-rise buildings with double facades, saving or waste of energy, Energy Build. 36 (2004) 381–389. https://doi.org/10.1016/j.enbuild.2004.01.018.

[78] V. Gavan, M. Woloszyn, F. Kuznik, J.J. Roux, Experimental study of a mechanically ventilated double-skin façade with venetian sun-shading device: A full-scale investigation in controlled environment, Sol. Energy. 84 (2010) 183–195. https://doi.org/10.1016/j.solener.2009.10.017.

[79] C.S. Park, G. Augenbroe, T. Messadi, M. Thitisawat, N. Sadegh, Calibration of a lumped simulation model for double-skin façade systems, Energy Build. 36 (2004) 1117–1130. https://doi.org/10.1016/j.enbuild.2004.04.003.

[80] C.S. Park, G. Augenbroe, N. Sadegh, M. Thitisawat, T. Messadi, Real-time optimization of a double-skin façade based on lumped modeling and occupant preference, Build. Environ. 39 (2004) 939–948. https://doi.org/10.1016/j.buildenv.2004.01.018.

[81] S. Rheault, E. Bilgen, Heat transfer analysis in an automated venetian blind window system, J. Sol. Energy Eng. Trans. ASME. 111 (1989) 89–95. https://doi.org/10.1115/1.3268291.

[82] C. Balocco, A non-dimensional analysis of a ventilated double façade energy performance, Energy Build. 36 (2004) 35–40. https://doi.org/10.1016/S0378-7788(03)00086-0.

[83] C. Balocco, M. Colombari, Thermal behaviour of interactive mechanically ventilated double glazed façade: Non-dimensional analysis, Energy Build. 38 (2006) 1–7. https://doi.org/10.1016/j.enbuild.2005.02.006.

[84] J.L. Hensen, Modeling and Simulation of a Double-Skin Façade System, (2002).

[85] R.M. Aynsley, A resistance approach to analysis of natural ventilation airflow networks, J. Wind Eng. Ind. Aerodyn. 67–68 (1997) 711–719. https://doi.org/10.1016/S0167-6105(97)00112-8.

[86] Z. Ioannidis, A. Buonomano, A.K. Athienitis, T. Stathopoulos, Modeling of double skin façades integrating photovoltaic panels and automated roller shades: Analysis of

the thermal and electrical performance, Energy Build. 154 (2017) 618–632. https://doi.org/10.1016/j.enbuild.2017.08.046.

[87] E. Gratia, A. De Herde, Greenhouse effect in double-skin facade, Energy Build. 39 (2007) 199–211. https://doi.org/10.1016/j.enbuild.2006.06.004.

[88] N. Hashemi, R. Fayaz, M. Sarshar, Thermal behaviour of a ventilated double skin facade in hot arid climate, Energy Build. 42 (2010) 1823–1832. https://doi.org/10.1016/j.enbuild.2010.05.019.

[89] J. Zhou, Y. Chen, A review on applying ventilated double-skin facade to buildings in hot-summer and cold-winter zone in China, Renew. Sustain. Energy Rev. 14 (2010) 1321–1328. https://doi.org/10.1016/j.rser.2009.11.017.

[90] W.J. Stec, A.H.C.V. Paassen, Symbiosis of the double skin façade with the HVAC system, Energy Build. 37 (2005) 461–469. https://doi.org/10.1016/j.enbuild.2004.08.007.

[91] D. Faggembauu, M. Costa, M. Soria, A. Oliva, Numerical analysis of the thermal behaviour of glazed ventilated facades in Mediterranean climates. Part II: Applications and analysis of results, Sol. Energy. 75 (2003) 229–239. https://doi.org/10.1016/j.solener.2003.07.014.

[92] D. Saelens, S. Roels, H. Hens, Strategies to improve the energy performance of multiple-skin facades, Build. Environ. 43 (2008) 638–650. https://doi.org/10.1016/j.buildenv.2006.06.024.

[93] D. Saelens, J. Carmeliet, H. Hens, Energy performance assessment of multiple-skin facades, HVAC R Res. 9 (2003) 167–185. https://doi.org/10.1080/10789669.2003.10391063.

[94] D. Saelens, S. Roels, H. Hens, The inlet temperature as a boundary condition for multiple-skin facade modelling, Energy Build. 36 (2004) 825–835. https://doi.org/10.1016/j.enbuild.2004.01.005.

[95] T.E. Jiru, F. Haghighat, Modeling ventilated double skin façade-A zonal approach, Energy Build. 40 (2008) 1567–1576. https://doi.org/10.1016/j.enbuild.2008.02.017.

[96] Y. Jaluria, S.N. Atluri, Computational heat transfer, Comput. Mech. 14 (1994) 385–386. https://doi.org/10.1007/BF00377593.

[97]   A. Krimotat, H. Sedarat, Structural modeling, 2014. https://doi.org/10.1201/b15616.

[98]   A.M. Afonso, M.S.N. Oliveira, P.J. Oliveira, M.A. Alves, F.T. Pinho, The Finite Volume Method in Computational Rheology, 2012. https://doi.org/10.5772/38644.

[99]   N.A. Fallah, C. Bailey, M. Cross, G.A. Taylor, Comparison of finite element and finite volume methods application in geometrically nonlinear stress analysis, Appl. Math. Model. 24 (2000) 439–455. https://doi.org/10.1016/S0307-904X(99)00047-5.

[100] B. Diskin, J.L. Thomas, Notes on accuracy of finite-volume discretization schemes on irregular grids, Appl. Numer. Math. 60 (2010) 224–226. https://doi.org/10.1016/j.apnum.2009.12.001.

[101] T.R. Borgers, H. Akbari, Free convective turbulent flow within the trombe wall channel, Sol. Energy. 33 (1984) 253–264. https://doi.org/10.1016/0038-092X(84)90156-7.

[102] R. Ben Yedder, Z.G. Du, E. Bilgen, Numerical study of laminar natural convection in composite trombe wall systems, Sol. Wind Technol. 7 (1990) 675–683. https://doi.org/10.1016/0741-983X(90)90042-Z.

[103] F. Mootz, J.J. Bezian, Numerical study of a ventilated facade panel, Sol. Energy. 57 (1996) 29–36. https://doi.org/10.1016/0038-092X(96)00042-4.

[104] L. Zalewski, S. Lassue, B. Duthoit, M. Butez, Study of solar walls - Validating a simulation model, Build. Environ. 37 (2002) 109–121. https://doi.org/10.1016/S0360-1323(00)00072-X.

[105] Z. Yilmaz, F. Çetintaş, Double skin façade's effects on heat losses of office buildings in Istanbul, Energy Build. 37 (2005) 691–697. https://doi.org/10.1016/j.enbuild.2004.07.010.

[106] L. Mei, D. Infield, U. Eicker, V. Fux, Thermal modelling of a building with an integrated ventilated PV façade, Energy Build. 35 (2003) 605–617. https://doi.org/10.1016/S0378-7788(02)00168-8.

[107] R. Charron, A.K. Athienitis, Optimization of the performance of double-façades with integrated photovoltaic panels and motorized blinds, Sol. Energy. 80 (2006) 482–491. https://doi.org/10.1016/j.solener.2005.05.004.

[108] N. Safer, M. Woloszyn, J.J. Roux, Three-dimensional simulation with a CFD tool of the airflow phenomena in single floor double-skin facade equipped with a venetian blind, Sol. Energy. 79 (2005) 193–203. https://doi.org/10.1016/j.solener.2004.09.016.

[109] G. Baldinelli, Double skin façades for warm climate regions: Analysis of a solution with an integrated movable shading system, Build. Environ. 44 (2009) 1107–1118. https://doi.org/10.1016/j.buildenv.2008.08.005.

[110] B. Corporation, Technical Data Sheet Lumogen® F Red 305, (n.d.).

[111] D.I. Adhesives, Technical Data Sheet: DELO-PHOTOBOND GB368, (2014).

[112] SunPower, Technical Data Sheet: C50 SOLAR CELL MONO CRYSTALLINE SILICON, (2010).

[113] 3M, Technical Data Sheet: DF2000MA Release B, (2015).

[114] S. Dragićević, M. Lambic, Influence of constructive and operating parameters on a modified Trombe wall efficiency, Arch. Civ. Mech. Eng. 11 (2011) 825–838. https://doi.org/10.1016/s1644-9665(12)60080-6.

[115] V. BCcomponents, NTC Thermistors, Datasheet, (n.d.).

[116] W. Pasut, M. De Carli, Evaluation of various CFD modelling strategies in predicting airflow and temperature in a naturally ventilated double skin faade, Appl. Therm. Eng. 37 (2012) 267–274. https://doi.org/10.1016/j.applthermaleng.2011.11.028.

[117] F. Schlegel, COMSOL: Using the Boussinesq Approximation for Natural Convection, (n.d.). https://www.comsol.com/blogs/using-the-boussinesq-approximation-for-natural-convection/ (accessed January 13, 2022).

[118] ScienceDirect, Grashof Number - an overview | ScienceDirect Topics, (n.d.). https://www.sciencedirect.com/topics/chemistry/grashof-number.

[119] Porotherm, Technical datasheet Porotherm BIO inc 12, (n.d.). https://www.wienerberger.it/content/dam/wienerberger/italy/marketing/documents-magazines/technical/technical-product-info-sheet/wall/Sch_tec_Pth_BIO_inc_12x50x19_BUB.pdf.

[120] M.I. of T. MIT, PMMA Properties, (n.d.).

http://www.mit.edu/~6.777/matprops/pmma.htm.

[121] Q. LI, A. ping WU, Y. jun LI, G. qing WANG, B. jin QI, D. yang YAN, L. yu XIONG, Segregation in fusion weld of 2219 aluminum alloy and its influence on mechanical properties of weld, Trans. Nonferrous Met. Soc. China (English Ed. 27 (2017) 258–271. https://doi.org/10.1016/S1003-6326(17)60030-X.

[122] R. Brandt, G. Neuer, Electrical resistivity and thermal conductivity of pure aluminum and aluminum alloys up to and above the melting temperature, Int. J. Thermophys. 28 (2007) 1429–1446. https://doi.org/10.1007/s10765-006-0144-0.

[123] C. Borgohain, K. Acharyya, S. Sarma, K.K. Senapati, K.C. Sarma, P. Phukan, A new aluminum-based metal matrix composite reinforced with cobalt ferrite magnetic nanoparticle, J. Mater. Sci. 48 (2013) 162–171. https://doi.org/10.1007/s10853-012-6724-4.

[124] IUAV, Materiali isolanti, Architecture. (2017) 50–51.

[125] K.S. Ong, A mathematical model of a solar chimney, Renew. Energy. 28 (2003) 1047–1060. https://doi.org/10.1016/S0960-1481(02)00057-5.

[126] L. Evangelisti, C. Guattari, F. Asdrubali, On the sky temperature models and their influence on buildings energy performance: A critical review, Energy Build. 183 (2019) 607–625. https://doi.org/10.1016/j.enbuild.2018.11.037.

[127] A. Albatayneh, D. Alterman, A. Page, B. Moghtaderi, The significance of sky temperature in the assessment of the thermal performance of buildings, Appl. Sci. 10 (2020) 1–16. https://doi.org/10.3390/app10228057.

[128] COMSOL, Radiative cooling, (n.d.). https://www.comsol.it/model/radiative-cooling-75021.

[129] M. Rashidian, D. Dorranian, Low-intensity UV effects on optical constants of PMMA film, J. Theor. Appl. Phys. 8 (2014) 0–7. https://doi.org/10.1007/s40094-014-0121-0.

[130] C.O. Ayieko, R.J. Musembi, A.A. Ogacho, B.O. Aduda, B.M. Muthoka, P.K. Jain, Controlled Texturing of Aluminum Sheet for Solar Energy Applications, Adv. Mater. Phys. Chem. 05 (2015) 458–466. https://doi.org/10.4236/ampc.2015.511046.

[131] R.M. Ahmed, Optical study on poly(methyl methacrylate)/poly(vinyl acetate) blends, Int. J. Photoenergy. 2009 (2009). https://doi.org/10.1155/2009/150389.

[132] C. Da Wen, I. Mudawar, Emissivity characteristics of polished aluminum alloy surfaces and assessment of multispectral radiation thermometry (MRT) emissivity models, Int. J. Heat Mass Transf. 48 (2005) 1316–1329. https://doi.org/10.1016/j.ijheatmasstransfer.2004.10.003.

[133] E.A. Estalote, K.G. Ramanathan, Low-temperature emissivities of copper and aluminum, J. Opt. Soc. Am. 67 (1977) 39. https://doi.org/10.1364/josa.67.000039.

[134] T. Fiedler, N. White, M. Dahari, K. Hooman, On the electrical and thermal contact resistance of metal foam, Int. J. Heat Mass Transf. 72 (2014) 565–571. https://doi.org/10.1016/j.ijheatmasstransfer.2014.01.045.

[135] V. Casalegno, P. Vavassori, M. Valle, M. Ferraris, M. Salvo, G. Pintsuk, Measurement of thermal properties of a ceramic/metal joint by laser flash method, J. Nucl. Mater. 407 (2010) 83–87. https://doi.org/10.1016/j.jnucmat.2010.09.032.

[136] COMSOL, Greenhouse Effect, (n.d.). https://www.comsol.it/model/greenhouse-effect-98061.

[137] S. Wijesuriya, P.C. Tabares-Velasco, K. Biswas, D. Heim, Empirical validation and comparison of PCM modeling algorithms commonly used in building energy and hygrothermal software, Build. Environ. 173 (2020) 106750. https://doi.org/10.1016/j.buildenv.2020.106750.

[138] D.S. Vijayan, A. Mohan, J. Revathy, D. Parthiban, R. Varatharajan, Evaluation of the impact of thermal performance on various building bricks and blocks : A review, Environ. Technol. Innov. 23 (2021) 101577. https://doi.org/10.1016/j.eti.2021.101577.

[139] Z. Pavlík, M. Záleská, M. Pavlíková, R. Černý, The thermal and mechanical performance of cement-based composites with enhanced thermal insulation properties, WIT Trans. Eng. Sci. 83 (2014) 251–260. https://doi.org/10.2495/HT140231.

[140] K.W. Borth, R. Ferreira, D. Galante, F.J. Anaissi, M.G.P. Valenga, Structural and morphological behaviour and study of the colorimetric and reflective properties of

commercial inorganic pigments, South African J. Chem. 72 (2019) 215–221. https://doi.org/10.17159/0379-4350/2019/V72A28.

[141] N.P. Avdelidis, A. Moropoulou, Emissivity considerations in building thermography, Energy Build. 35 (2003) 663–667. https://doi.org/10.1016/S0378-7788(02)00210-4.